January 2013

Effect of Localized Corrosion of Steel on Chloride-Induced Concrete Cover Cracking in Reinforced Concrete Structures

Ezeddin Rafaa Busba
University of South Florida, ezeddin@hotmail.com

Effect of Localized Corrosion of Steel on Chloride-Induced Concrete Cover Cracking in Reinforced Concrete Structures

by

Ezeddin Busba

A dissertation submitted in partial fulfillment
of the requirements for the degree of
Doctor of Philosophy
Department of Civil and Environmental Engineering
College of Engineering
University of South Florida

Major Professor: Alberto Sagüés, Ph.D.
Rajan Sen, Ph.D.
Gray Mullins, Ph.D.
Richard Gilbert, Ph.D.
Matthias Batzill, Ph.D.

Date of Approval:
November 22, 2013

Keywords: Corrosion Propagation, Spalling, Durability, Modeling, Corrosion Rate

DEDICATION

To my parents and all my family, whom I ask Allah to shower with mercy and blessing and to count this work as part of their good deeds

ACKNOWLEDGMENTS

Above all, I deeply express my countless thanks and gratitude to Allah for granting me the ability to proceed successfully.

First and foremost, I sincerely thank my advisor, Dr. Alberto Sagüés for his valuable guidance, continual support and words of encouragement. I would also like to thank my committee chairperson and members for their patience and helpful comments. Sincere thanks and gratitude go to Dr. K. Esaklul, Dr. M. Nachabe and Dr. A. Zayed for their kind assistance. The assistance of the FDOT State Materials Office is thankfully acknowledged. I should also express my sincere thanks to Amideast for sponsoring me under the Fulbright foreign student program and also to the Libyan MOE for the partial scholarship. The efforts made by K. Nawaa, A. Ibrahim, R. Barasi, R. El Rbaa and H. Sgoutri in attempting to secure funds are highly appreciated. I am also grateful to all the undergraduate students of USF whose help contributed a great deal to making this work a success. Many thanks go to my co-workers in the corrosion laboratory, A. Sanchez, K. Lau, M. Dugarte, A. Accardi, M. Walsh, S. Hoffman, M. Hutchison, J. Fernandez, E. Paz, S. Alshehri, M. Akhoondan, J. Cardenas and K. Williams for the friendly atmosphere. Last but not least, I would like to thank the Libyan and Muslim community in Tampa for providing a home-like environment.

TABLE OF CONTENTS

LIST OF TABLES

LIST OF FIGURES

ABSTRACT

Concrete cover cracking due to reinforcement corrosion is widely accepted as a limit-state indicator in defining the end of functional service life for existing reinforced concrete (RC) structures undergoing corrosion. Many of the currently available durability prediction models are incapable of providing realistic estimates of remaining service lives of RC structures beyond the corrosion initiation point. Therefore, the need to incorporate the length of the corrosion propagation stage in a comprehensive durability prediction approach has recently received much research attention. Previous research focus however was mostly limited to the case of uniformly corroding reinforcement with only few studies addressing the commonly encountered case of localized rebar corrosion. It was empirically shown in a previous study that localized corrosion can have a mitigating effect on time to concrete cover cracking due to the larger required depth of rebar corrosion penetration (Critical penetration or X_{crit}). The present research was focused on developing a model for predicting X_{crit} for various degrees of corrosion localization including new cases of highly localized corrosion. Accelerated corrosion testing of controlled anodic regions along axial rebars in sound concrete cylinders suggested that localized corrosion can increase X_{crit} by up to about a factor of 10. The effect of corrosion localization on the orientation of corrosion-induced surface cracks was also addressed. Testing

of freely corroding pre-cracked RC pipe specimens in a chloride-containing environment indicated that steel corrosion can be localized at intersection regions with the pre-existing cracks and uniformly distributed around the reinforcing steel perimeter. Numerical modeling was undertaken to substantiate the experimentally observed trends on a theoretical basis for various degrees of corrosion localization. A mechanical model was developed to improve understanding of the underlying mechanism responsible for corrosion-induced stresses. A thick-walled multiple-cylinder approach was employed to simulate crack initiation and propagation to account for the residual strength property of concrete after cracking by applying the principles of applied elasticity. For a given concrete cover depth, the amount of X_{crit} was shown by modeling to be largely determined by the length of corroding region and the capacity of the induced cracks to accommodate produced rusts. The properties of both concrete-rebar interface and corrosion products were also found to have a significant impact on X_{crit}. Based on the model and experimental trends and comparisons with literature data, an improved relationship for the estimation of X_{crit} was proposed. An electrochemical model was also formulated to address the possible role of corrosion aggravation due to macrocell coupling in counteracting the mitigating effect of increased X_{crit} on time to concrete cover cracking. Findings confirmed that corrosion localization can reasonably be considered a mitigating factor for extending the corrosion propagation stage, and provided more precise quantification to that effect.

1. INTRODUCTION

1.1 Background

The total direct cost of corrosion estimated in 2002 by the Federal Highway Administration (FHWA) was $ 276 billion per year which makes 3.1% of the national gross domestic product (GDP) in the United States. The direct cost of corrosion in the highway bridges only was estimated by $8.3 billion per year with possible indirect costs of 10 times greater. The national bridge inventory (NBI) data base released by FHWA in 2010 indicated that the entire bridge population is 604,485 of which 69,223 (11.5%) are classified as structurally deficient with a mean age of ~62 years. Both conventional and pre-stressed concrete bridges represented ~ 68% of the total population of bridges [Lee 2012- parts 1 and 2]. Reliable and timely maintenance programs are therefore necessary to prevent catastrophic failures and minimize deterioration of bridges. In an effort to highlight the issue of deteriorating infrastructure in the U.S., LePatner has recently launched an interactive Google map featuring nearly 8000 bridges nationwide labeled by the FHWA as “structurally deficient” and “fracture critical”. The total cost of repair and rehabilitation of those bridges was estimated to be up to about $60 billion [LePatner 2012].

Corrosion-induced concrete cover cracking is considered an important performance limit state marking the end of functional service life of a reinforced

concrete (RC) structure. Estimating the remaining service life of corrosion-affected RC structures is required by asset owners and practicing engineers for repair and maintenance planning.

1.2 Problem Statement and Research Significance

Reinforcing steel is initially protected by a passive layer of iron oxides / hydroxides in alkaline, uncontaminated concrete. Unfortunately, the protective layer can be destroyed due to chloride contamination when the chloride concentration at the steel surface reaches a critical amount. Corrosion durability of RC structures exposed to chloride-containing environments is measured by the length of durations of both corrosion initiation and propagation phases [Tuutti 1982]. The corrosion initiation phase is defined as the length of time needed for chloride ions to diffuse from the external surface of concrete to reach the imbedded steel and exceed the critical chloride concentration. On the other hand, the corrosion propagation phase is defined as the length of time from the onset of corrosion to the onset of corrosion-induced cover cracking [Val et al. 2009].

Various service life predictive models were developed to forecast the initiation stage. Chloride ion transport is typically assumed to be controlled by a diffusion process driven by chloride concentration gradient. The apparent diffusion coefficient of chloride through concrete and the chloride concentration at the external concrete surface are generally assumed to be constant with time [Sagüés et al. 2006]. Various commercially available models (e.g. Life 365®, Stadium®, etc.) are customarily developed based on the corrosion initiation stage with a pre-set fixed value for the corrosion propagation period [Williamson 2007].

However, once corrosion has initiated or where pre-existing narrow cracks are present in a reinforced concrete member, the corrosion propagation period becomes predominant. Therefore, a reliable prediction accounting for the variability of the corrosion propagation period is required to realistically estimate the remaining service life of a corroding RC structure.

Active corrosion of embedded steel produces expansive corrosion products with specific volumes several times greater than that of the original steel. Those corrosion products result in pressure on surrounding concrete associated with radial and hoop stresses with a tensile component. Given the low tensile strength of concrete, the generated stresses can ultimately lead to cracking and spalling of the cover concrete. Knowledge of the critical amount of rebar radius loss needed for cracking, (also known as critical penetration, X_{crit}), along with a reliable estimate of the projected corrosion rate is important for the overall service life prediction of a corroding RC structure. Most of the previous research work was focused on developing models for determining X_{crit} assuming an approximately uniform distribution of corrosion along the length of rebar [Jamali et al. 2013]. However, localized corrosion is commonly encountered in practice, especially in high quality concrete structures. Localized corrosion can occur due to the presence of preexisting narrow cracks in cover concrete, concrete cold joints and similar concrete deficiencies [Lau 2010b] or coating defects in epoxy-coated steel. The application of X_{crit} models intended for uniformly distributed corrosion can unnecessarily lead to significant underestimation of remaining service lives for RC members suffering localized corrosion.

Very limited research work has previously been undertaken to examine the positive effect of corrosion localization on tolerance of more rebar radius loss, X_{crit}, required for concrete cover cracking. Torres-Acosta and Sagüés [Torres-Acosta et al. 2004] suggested a user-friendly empirical relationship showing that the amount of critical penetration, X_{crit}, increases as corrosion becomes more localized along embedded reinforcing bar. However, that experimental investigation did not include cases of sufficiently localized corrosion representative of conditions typically encountered at the bottom of narrow preexisting cracks intersecting rebars. Therefore extrapolation of the proposed relationship to cases of small corroding lengths may be associated with significant uncertainty. Further, the empirical nature of the proposed model highlights the need for its verification/validation using a reliable theoretical approach to model the responsible underlying phenomena. A more recent study by Darwin and O'Reilly [Darwin et al. 2011] suggested an alternative more sophisticated model based, in part, on testing epoxy-coated rebars with controlled areas of coating damage. One major drawback related to that study is that the values of X_{crit} were solely determined based on Faradaic calculation of corrosion damage. The latter can be different from actual values unless confirmed by gravimetric evaluation. In addition, coated rebars are associated with uncertainty in the amount of corrosion damage due to possible wide variation in the extent of coating distress [Sagüés et al. 2006]. The uncertainty associated with the Darwin's model predictions does not justify the model

complexity which provides no significant advantage in its application over its empirical predecessor, as will be shown in the next chapter [Busba et al. 2013a].

Further, localized corrosion may result in the formation of a corrosion macrocell due to electrochemical coupling between the small corroding spot and the larger surrounding passive steel region. The macrocell coupling is likely to aggravate the corrosion current leading to a faster rate of radius loss compared to the case of uniform corrosion otherwise exposed to the same conditions. As a result, the positive mitigating effect of localized corrosion on the amount of X_{crit} needed for cracking may be counteracted by the higher corrosion rate expected at a small corroding spot. Those possible competing effects on the duration of propagation stage were not addressed in the literature in detail. The effects of both X_{crit} and corrosion rate on the duration of propagation stage were examined here as the degree of corrosion localization increased. Those competing effects were examined to highlight the possible extent to which corrosion localization can be considered a mitigating factor for cover cracking.

The above discussion underscores the need for developing a reliable model for determining the amount of critical penetration, $X_{crit,}$ for the case of localized corrosion. The model can serve as a useful tool that can be incorporated along with existing reliable corrosion rate projection models in a comprehensive service life forecasting model for RC structures. The effect of concrete parameters variability on the amount of X_{crit} can be accounted for by using a probabilistic approach [Lau et al. 2010a].

The overall service life predictive models should be capable of providing a reliable estimate of time to cover cracking. As a result, they can assist in defining a timely and cost-effective intervention point for repair of the corrosion-affected existing RC structures to maintain their serviceability.

1.3 Research Objectives

(a) Determine experimentally the effect of highly localized corrosion of steel reinforcement on the critical penetration (X_{crit}) needed for concrete cover cracking. Testing should extend to sufficiently localized corrosion conditions representative of those typically encountered at the intersection of rebars with preexisting narrow cracks or similar concrete deficiencies. Based on the observed experimental trends, a functional relationship should be derived for the critical penetration (X_{crit}) in terms of the degree of corrosion localization and system geometrical configurations.

(b) Improve the prediction of critical penetration (X_{crit}) based on understanding the underlying mechanism and controlling factors. This was achieved by developing a theoretical mechanical model using the principles of applied elasticity to simulate the stresses induced by corrosion products (rust). The modeling was used to examine cases having similar geometric configurations to those tested experimentally. The model should take into account the residual strength of concrete cover after cracking. It should also examine the effect of properties and amounts of rust accommodated in the rebar-concrete interface and within the induced cracks for cases of uniform and localized corrosion. The present and previous experimental findings of critical

penetration, X_{crit}, should be used to validate and calibrate the theoretical model, as appropriate.

(c) Examine the role of possible corrosion rate aggravation due to localized corrosion in counteracting the mitigating effect of increased X_{crit} on time to concrete cover cracking. An electrochemical model is to be developed to simulate corrosion macrocell coupling between a small corrosion region and a large passive region for various corroding to passive surface area ratios similar to those tested experimentally but under natural exposure conditions. The extent to which local corrosion rate can be aggravated due to localization is then to be determined. The model should provide an answer to the question as to whether such a possibly higher corrosion rate can counteract the positive effect of the increased X_{crit} on extending the propagation period and hence the service life.

2. LITERATURE REVIEW

2.1 Concrete Composition and its Chemistry

Concrete is a widely used construction material due to its versatility and relatively low cost. Concrete is a composite material composed of cement paste as a binder with a low cost filler of coarse (stone) and fine (sand) aggregates making about 60-75% of the mix total volume. The main chemical constituents of cement are tricalcium silicate (C_3S), dicalcium silicate (C_2S), tricalcium aluminate (C_3A), tetracalcium alumioferite (C_4AF) and calcium sulfate (Gypsum). Water is added to the concrete mix with appropriate amounts to cause the cement to hydrate and form hydration products (cement paste). The latter is typically made up of about 75% calcium silicate hydrate gel (C-S-H) (by volume of hardened cement), 20% solid crystalline calcium hydroxide and low amount of calcium aluminate compounds. The hydration reaction is exothermic in nature and result in the hardening of concrete as it progresses. The hydrated cement exhibits capillary porosity with the pores partially filled with a saturated solution of calcium hydroxide. The pore solution also contains high concentrations of sodium and potassium ions which make the solution highly alkaline (pH =12.5 to 13.6). The most commonly reported mechanical property of concrete is its 28-day compressive strength with typical values around e.g. 35 Mpa in highway construction applications. Concrete is however brittle with its tensile strength

being an order of magnitude less than its compressive strength. Embedded steel reinforcement is therefore used in reinforced concrete structures to handle tensile stresses. Fortunately, steel in alkaline, uncontaminated concrete environment is found to be protected (passivity) from corrosion damage. In addition, the thermal compatibility of steel and concrete (thermal expansion coefficients 11.8×10^{-6} and 12×10^{-6} /^{o}C, respectively) enables the use of steel-reinforced concrete as a construction material. [Mindess et al. 2003, Materials Property Data]

2.2 Passivation

The alkaline concrete environment results in the formation of a very thin (e.g. a few nm) and dense protective layer of iron oxide / hydroxide on the embedded steel surface due to corrosion of the steel itself. Figure 2.1 shows the region (shaded area) at which the passive layer is thermodynamically stable (insoluble) for steel in aqueous solution after Pourbaix. The passive protective layer is adherent to the surface and believed to be mainly composed of gamma ferric oxide (γ-Fe_2O_3). The oxide layer develops as the cement hydration progresses. Due to the amorphous structure of the passive layer, the diffusion of iron ions (F^{2+}) from the steel substrate to the passive layer-concrete interface is made difficult [Pruckner 2001].

2.3 Corrosion of Steel in Concrete

2.3.1 General

Corrosion of steel reinforcement is a destructive process affecting the serviceability of reinforced concrete structures and can in extreme cases lead to

unexpected structural failure. The two main mechanisms responsible for the damage induced by steel reinforcement corrosion are concrete carbonation and chloride ingress. Concrete carbonation caused by the ingress of carbon dioxide from the surrounding atmosphere can result in the loss of alkaline conditions needed for steel passivity. The drop of pH to below about 9 can cause the steel to actively corrode [Sagüés et al. 1997].

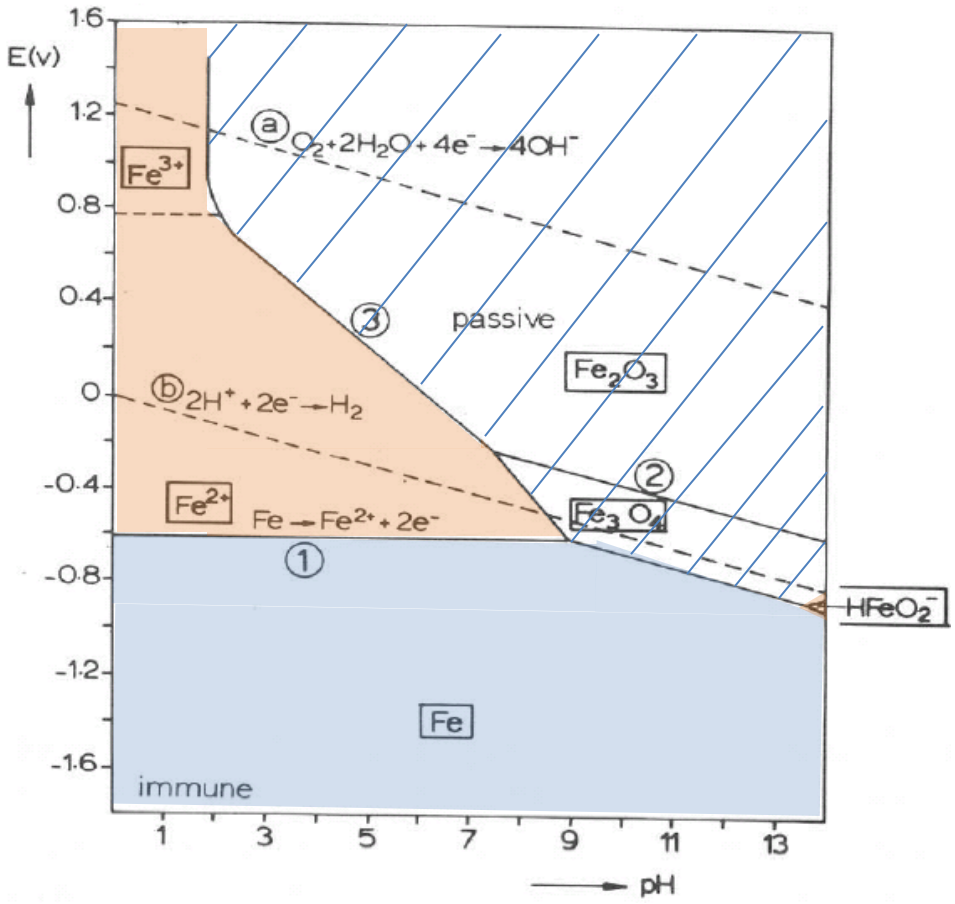

Figure 2.1 Simplified potential-pH equilibrium diagram for iron-H_2O system at a temperature of 25^o C [Gellings 2005].

Literature search has shown that chloride-induced corrosion can have an extensively damaging effect on reinforced concrete structures compared to that

of carbonation-induced corrosion [Val et al. 2009]. In chloride-containing environments, the ingress of chloride through concrete cover can destroy the protective passive layer and cause corrosion of the underlying steel to initiate. The protective layer can be disrupted when the chloride concentration at the steel / concrete interface reaches a critical amount known as the chloride corrosion threshold [Raupach1996]. Pruckner described the mechanism of passivity breakdown by three steps; adsorption of chloride ions on the surface of passive layer, penetration and formation of complexes [Pruckner 2001].

The functional service life of an RC structure affected by chloride-induced corrosion is divided into corrosion initiation and propagation periods [Tuutti 1982]. Figure 2.2 shows a simplified service life model based on the model first proposed by Tuutti.

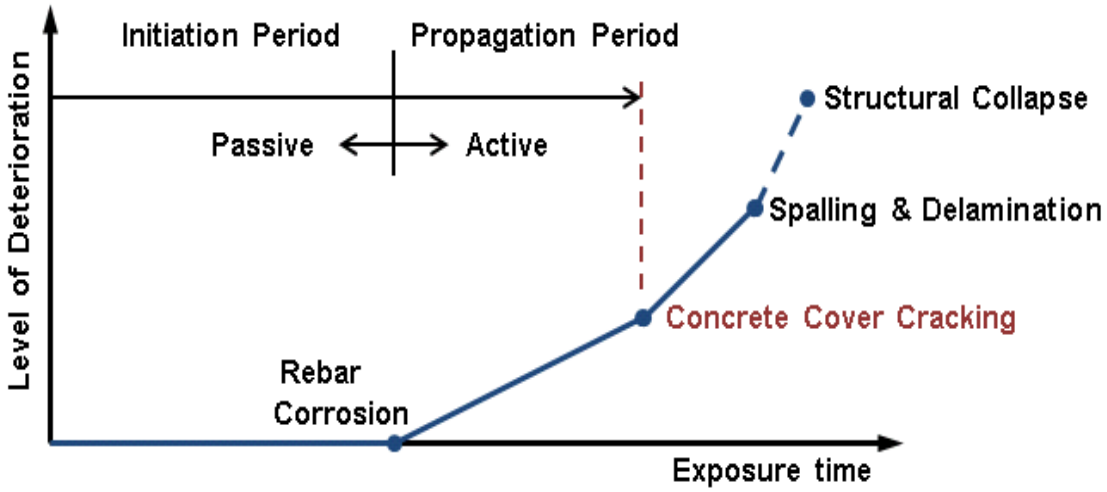

Figure 2.2 A simplified service life model based on Tuutti's model

2.3.2 Mechanism of Steel Reinforcement Corrosion

The corrosion process involves two coupled electrochemical reactions taking place on steel – concrete interface at separate sites. In order for the reactions to proceed there has to be an exchange of charge between the two sites. The electrochemical reaction that involves loss of electrons is known as anodic reaction whereas the one that involves gain of electrons is known as cathodic reaction [Gellings 2005]. Figure 2.3 shows a schematic diagram illustrating the corrosion process of a steel reinforcement in concrete. The common anodic and cathodic reactions of steel in concrete are iron dissolution (equation 2.1) and oxygen reduction (equation 2.2) reactions.

$$Fe \longrightarrow Fe^{2+} + 2e \qquad (2.1)$$

$$2H_2O + O_2 + 4e \longrightarrow 4OH^- \qquad (2.2)$$

The exchange of electrons results in electronic current flow along the rebar itself between the anodic and cathodic sites. At equilibrium, the anodic and cathodic reactions should proceed at the same rate which represents the corrosion rate of steel. To maintain the continuity of current there should be a flow of ionic current in the concrete (electrolyte) between the anodic and cathodic sites. It follows that concrete resistivity can become a rate-controlling factor for

both reactions. The resistivity depends on concrete permeability, the degree of concrete saturation and chloride content in pore water. If the current flow is limited by the resistance between the anode and cathode, the reaction rate is said to be under resistance control. Otherwise, the reaction rate will be proceeding under activation control as long as there is sufficient supply of reactants for each reaction. Once the reaction rate becomes controlled by the speed with which the reactants (ions) arrive at the reaction front, the reaction rate is then said to be under concentration control or diffusion control. The reaction rate can be governed by one or more of those three controlling mechanisms [Jones 1996].

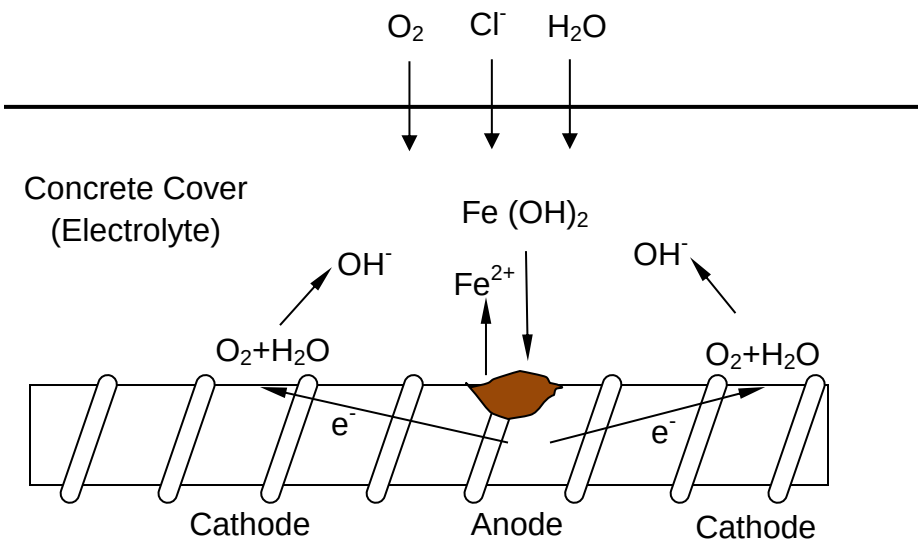

Figure 2.3 Corrosion of steel reinforcement in concrete

2.4 Chloride-induced Corrosion Initiation Stage

The initiation period is represented by the time needed for the chloride ions to transport from the external environment through the concrete cover and reach the rebar with sufficient amount to trigger corrosion. Figure 2.4 shows the modified Pourbaix diagram applicable for iron-H_2O system in the presence of chloride. The transport of chloride ions through concrete pore system proceeds mainly by diffusion driven by concentration gradient as well as by capillary action (convection) [Val et al. 2009]. For RC structures having thick concrete cover, the chloride transport is considered simply controlled by a time-dependent diffusion process which may be expressed in terms of Fick's second law as follows: [Bohni 2005]

$$\frac{\partial C}{\partial \mathrm{t}} = \mathrm{D}\nabla^2 C \tag{2.3}$$

where *C* is chloride ion concentration, t is time and D is chloride diffusion coefficient of concrete and customarily assumed to be spatially and time-independent. The relationship in (2.3) is usually treated as a one-dimensional case as shown in equation (2.4) and utilized for modeling time to corrosion initiation. In the case of constant diffusivity and surface chloride content, the error function solution is available (equation 2.5) [Crank 1975].

$$\frac{\partial C}{\partial \mathrm{t}} = \mathrm{D}\frac{\partial^2 C}{\partial \mathrm{X}^2} \qquad (2.4)$$

$$\frac{C_{X,t} - C_i}{C_S - C_i} = 1 - \mathrm{erf}\left(\frac{\mathrm{X}}{\sqrt{4\mathrm{Dt}}}\right) \qquad (2.5)$$

where X is the distance from external concrete surface inside concrete cover, (erf) is the error function, C_i is the initial chloride concentration in concrete, $C_{X,t}$ is the chloride concentration at a given depth from surface into concrete cover at time t and C_s is the external surface chloride concentration. Replacing the parameters X and $C_{X,t}$ in equation (2.5) with the values of concrete cover depth (C) and the chloride corrosion threshold (C_{th}) respectively allows the determination of time to corrosion initiation (ti).

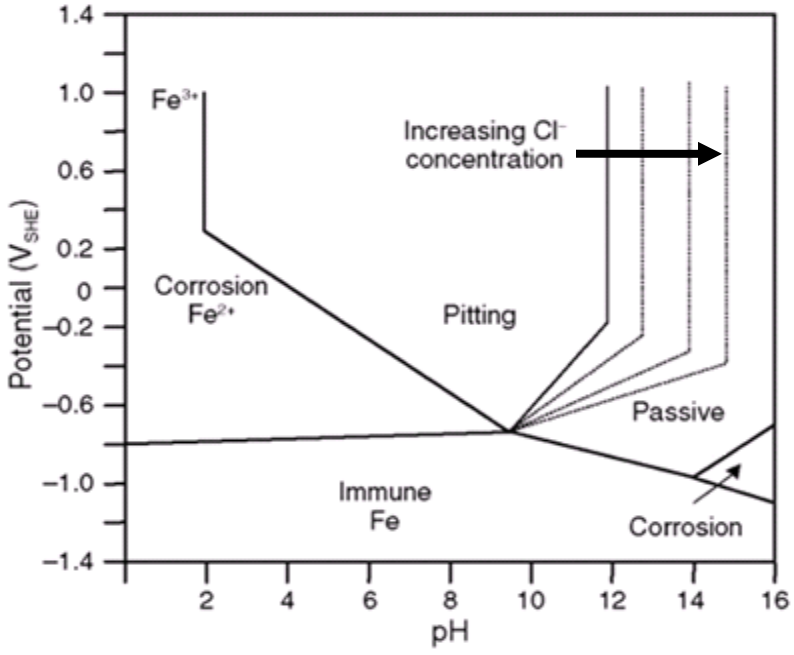

Figure 2.4 The potential-pH equilibrium diagram for iron-H_2O system in the presence of chloride ions

2.5 Chloride-induced Corrosion Propagation Stage

Once corrosion has initiated, its propagation is controlled primarily by the supply of oxygen, moisture content and resistivity of concrete [Tuutti 1982]. The length of the corrosion propagation stage is the time from corrosion initiation to a well-defined limit state. There are various damage indicators associated with different limit states such as; loss of rebar cross-sectional area, loss of bond strength between steel and concrete and corrosion-induced concrete cover cracking [Otieno et al. 2011]. Corrosion causes an initial increase in rebar to concrete bond strength due to the increased rebar surface roughness but further corrosion results in loss in bond strength. That loss is explained by deterioration of rebar ribs and the lubricating effect of the flaky thick layer of rust. The consequent corrosion-induced cracking tends to reduce the confining capacity of surrounding concrete [Sulaimani et al. 1990]. Many researchers have considered the appearance of corrosion-induced surface cracks as a performance limit state as it is relatively easy to determine in a corroding RC structure [Liu et al. 1998, Torres-Acosta et al. 2004]. Concrete cover cracking is caused by the accumulation of expansive corrosion products at the steel-concrete interface. Generally corrosion products can have a volume up to six times greater than that of the original steel [Marcotte 2001]. However, Hansson et al. found that the volume of corrosion products observed in concrete is between 2.2 and 3.3 times greater than that of steel from which they formed [Hansson et al. 2007]. As corrosion progresses, the corrosion products continue to accumulate and once it fills up the concrete pores, radial and hoop stresses start to develop. Cover

cracking begins when the stress state satisfies a certain cracking failure criterion. Figure 2.5 shows a schematic indicating the amount of rebar radius loss needed for cracking, X_{crit}, (also known as critical penetration).

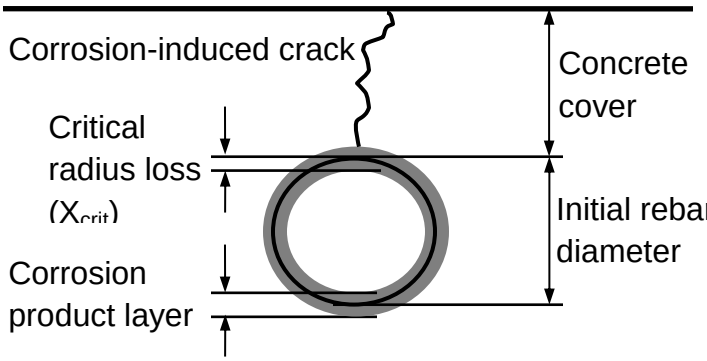

Figure 2.5 A conceptual diagram for corrosion-induced cracking

Generally, the corrosion initiation duration is several times longer (e.g. ~ 30 to 80 years) than that of the propagation stage (e.g. 5 years). In those cases, it is the accuracy of predicting the initiation period that determines the accuracy of predicting the overall service life [Mullard et al. 2011]. However, some RC structures exhibit corrosion early in service with longer corrosion propagation stage which highlights the need for accurate prediction of the variability in the corrosion propagation. The latter is also true in the case of new structures where, preexisting narrow cracking has caused corrosion to initiate relatively early.

The corrosion propagation period, in terms of time to cover cracking (T_{cr}), can be determined if the projected average corrosion rate (CR) and the critical rebar radius loss, X_{crit} are known as approximated by equation (2.6) [Sagüés et al. 2006]. The effect of rebar surface curvature can be reasonably neglected since the amounts of X_{crit} are usually very small (<<1 μm) in comparison. On first

approximation, equation (2.6) may be used for the prediction of the remaining service lives of corroding RC structures utilizing a probabilistic approach to account for the variability of the controlling parameters [Lau et al. 2010a].

$$T_{cr}\ (y) = X_{crit}\ (mm) / CR\ (mm/y) \qquad (2.6)$$

Various attempts were made to directly model the time to corrosion-induced cracking assuming time-invariant corrosion rates [El Maaddawy et al. 2007]. Corrosion rate is however expected to vary with time. Further, there are no reliable models currently available for the prediction of corrosion rate versus time [Otieno et al. 2011, Val et al. 2009]. It appears that the variability in corrosion rate can make it difficult to abstract the individual effects of X_{crit} and corrosion rate on time to cracking. Further, studying the direct effects of parameters such as concrete tensile strength, Poisson's ratio and rust properties on time to cracking has led to widely varying or even contradictory conclusions [Jamali et al. 2013]. That significant uncertainty may be attributed to the expected wide variation in corrosion rate from the moment of corrosion initiating up to the development of externally visible cracking. That uncertainty can be further complicated by the test acceleration necessitated during laboratory tests. Therefore developing separate models for predicting Xcrit and corrosion rate may be more reliable for determining their individual contributions to the cracking process. The corrosion rate and X_{crit} models can therefore be integrated into a comprehensive durability prediction approach to reasonably estimate time to cracking. The present

research work is only focused on studying the critical rebar radius loss (X_{crit}) induced by localized corrosion.

2.6 Factors Affecting the Critical Penetration

2.6.1 Geometrical Parameters and Concrete Properties

Alonso et al. investigated with accelerated laboratory test the key parameters controlling the corrosion penetration required for cover cracking under uniform corrosion conditions [Alonso et al.1998]. The study determined that X_{crit} is related to the ratio of concrete cover to rebar diameter (C/Ø) and proposed the following simple empirical relationship:

$$X_{crit}/\mu m = a + b\,\frac{C}{\emptyset} \tag{2.7}$$

where a and b are constants (7.53 and 9.32 μm, respectively). That study concluded that for C/Ø ≥ 2, the amount of X_{crit} needed to create a 0.05 mm wide surface crack is ~ 50 μm whereas for C/Ø ≤ 2, the amount of X_{crit} needed is between 15 – 30 μm. It was also determined that experiments with excessively accelerated corrosion rates required higher amounts of X_{crit} than those with slow corrosion rates and otherwise comparable conditions. The effect of applied corrosion current density in accelerated experiments is discussed in more detail in the following section. Alonso et al. also suggested that concrete with higher water to cement ratios require greater values of X_{crit}. Although not quantified,

such an effect was explained by the higher permeability associated with higher water to cement ratios which in turn allows corrosion products to diffuse away from the steel-concrete interface. It was also determined that greater amounts of corrosion attack penetration are needed to create wider surface cracks following a linear behavior between both variables [Alonso et al. 1998]. The latter finding may explain the discrepancy in the values of X_{crit} obtained by different researchers. Crack width limit states defined by other researchers include ~ 0.1 mm [Torres-Acosta et al. 2004], 0.05 mm [Darwin et al. 2011] and 0.3, 0.5 and 1 mm [Vu et al. 2005].

Liu and Weyers employed the concept of a thick-walled cylinder to analytically derive a relationship (2.8) for determining the critical mass of corrosion products required for concrete cover cracking in the case of uniform corrosion [Liu et al. 1998]. A critical mass was defined as the sum of corrosion product mass needed to fill up the interconnected pores at the steel-concrete transition zone and that required to generate expansive radial and hoop stresses up to cracking. The corrosion product was assumed to be composed of a mix of ferrous and ferric hydroxides, $Fe(OH)_2$ and $Fe(OH)_3$, with a relative mass ratio of steel to corrosion product being 0.622 and 0.523, respectively. Concrete was assumed to crack when the hoop stress reaches the tensile strength of concrete as the corrosion products continue to build up. The critical mass of corrosion product per unit length of rebar, W_{crit}, (equation 2.8) was found to be mainly influenced by the type of corrosion product, concrete cover, rebar diameter, properties of concrete and steel-concrete interface. The critical amount of steel

corroded per unit length of rebar (Δm) may be found by multiplying W_{crit} by the corrosion product to steel mass ration. Given the density of steel, the consumed steel volume per unit length of rebar may be determined and therefore the value of X_{crit} can be calculated (see equation 3.5).

$$W_{Crit} = \rho_{rust}\left(\pi\emptyset\left[\frac{Cf_t'}{E_{ef}}\left(\frac{a^2+b^2}{b^2-a^2}+\nu\right)+d_o\right]+\frac{\Delta m}{\rho}\right) \qquad (2.8)$$

where $a = (\emptyset+2d_o)/2$, $b = C + [(\emptyset+2d_o)/2]$ and $\Delta m = \gamma W_{crit.}$ The parameters Ø, C, d_o, ν, ρ and ρ_{rust} represent rebar diameter, concrete cover, thickness of porous interfacial zone (ITZ), concrete Poisson's ratio, density of iron and density of rust. The parameter E_{ef} represents the effective modulus of elasticity for concrete and expressed by $E_{ef} = [E_c / (1+\varphi_{cr})]$, where E_c is the concrete modulus of elasticity and φ_{cr} is the concrete creep coefficient. The parameter γ is a constant related to the rust molecular mass and obtained by dividing the molecular mass of iron by the molecular mass of rust.

The derived model (2.8) however may not be practical as it requires input information hard to obtain for determining the critical mass of corrosion product. More importantly, as with the other model introduced in this section, the model is only intended for uniformly corroding rebars and therefore not capable of providing information on critical penetration (X_{crit}) in the case of localized corrosion.

2.6.2 Effect of Corrosion Products

The degree of damage in concrete induced by corroding steel is dependent upon the type of corrosion product and its distribution within the concrete cover. All types of iron corrosion products have greater relative volumes than steel as shown in figure 2.6 [Marcotte 2001]. The corrosion products formed in atmospherically-exposed concrete were analyzed and found to be Fe_3O_4, α-Fe_2O_3, γ-Fe_2O_3, α-FeOOH and γ-FeOOH with specific volumes ranging from 2.2 to 3.3 compared to steel [Hansson et al. 2007]. The latter range is less than the corresponding value of red-brown rust, $Fe_2O_3.3H_2O$ which is customarily believed to be the main corrosion product with a specific volume of 6. Lazari et al. also performed an X-ray Diffraction (XRD) analysis of corrosion products in concrete exposed to atmosphere and reported corrosion product specific volumes ranging between 2 to 3.5. The main corrosion products found were Fe_3O_4, β-FeOOH and α-FeOOH [Lazari et al. 2000]. The type of corrosion product formed is generally dependent on exposure environmental conditions such as relative humidity and supply of oxygen [Jaffer et al. 2009]. Submerged corroding structures, for instance, are expected to form hydrated corrosion products that are possible to transport away from the steel-concrete interface. Therefore, the latter case may require more corrosion penetration for concrete cracking to occur (if any) [Sagüés et al. 2006 and Lazari et al. 2000].

Wong et al. investigated the penetration of corrosion products into concrete by image analysis [Wong et al. 2010]. It was found that corrosion products penetrated into the porous aggregate-paste interface and through the pores of

cement paste hydration products. Once the capillary pores and air voids are filled, the corrosion products were found to be forced to accumulate at the steel-concrete porous interfacial zone. It was also reported that a fraction of corrosion products preferentially accumulate at large cracks rather than at small pore spaces once corrosion cracking has initiated at the steel-concrete interface [Wong et al. 2010].

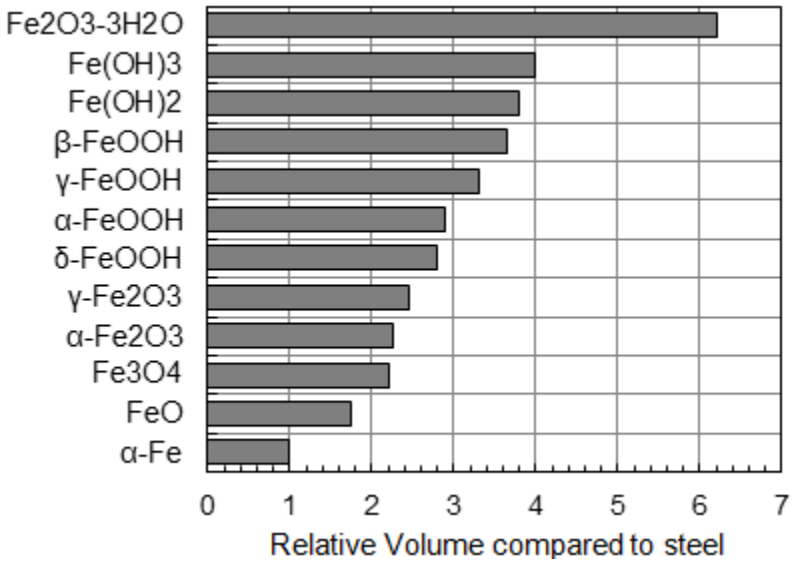

Figure 2.6 Corrosion products of iron [Marcotte 2001]

Lack of knowledge of corrosion product compositions is thought to be a source of discrepancy between theoretical model calculations and experimental data of X_{crit} [Lu et al. 2011].

2.6.3 Effect of Induced Corrosion Rate in Accelerated Testing

Corrosion acceleration is a common approach that has long been used to study the corrosion-induced damage in concrete structures to obtain results in

short durations. It was previously reported that results obtained from accelerated corrosion experiments are reasonably comparable to those from natural corrosion experiments [Torres-Acosta et al. 2010]. However, it has been argued that the widely-used direct linear extrapolation of results obtained from accelerated testing to behavior in real structures may be misleading [Vu et al. 2005 and Mullard et al. 2011]. Those investigators explained that corrosion-induced concrete cracking can be affected by the induced corrosion rate in one of two ways. Firstly, the value of X_{crit} increases as the corrosion rate increases up to a threshold value of about 150 to 200 μA/cm^2. This phenomenon was also observed by Alonso et al. [Alonso et al. 1998]. Secondly, the value of X_{crit} decreases as the impressed current density increases above a 200 μA/cm^2 threshold value. This behavior seems to be explained by an observation previously reported in the literature which attributed the effect to insufficient time for corrosion products to diffuse away from the steel/concrete interface [El Maaddawy et al. 2003]. Therefore, Vu et al proposed a correction factor for the accelerated anodic current density to account for those effects [Vu et al. 2005].

2.6.4 Effect of Corrosion Localization

The formation of non-corrosion related transverse cracks intersecting embedded reinforcement is expected to occur early in service in structures having large concrete covers [ACI 224-01]. The presence of such cracks can locally enhance chloride ingress leading to localized corrosion. It was shown that corrosion at crack-steel intersections can be highly localized at the intersection region and uniformly distributed around the perimeter [Busba et al. 2013b]. It was

previously suggested that the value of X_{crit} increases as corrosion becomes more localized along rebar length [Torres-Acosta et al. 2004]. However, the underlying mechanism responsible for that increase in X_{crit} was not explained. That phenomenon may in part be attributed to the availability of more space sidewise along the rebar for corrosion products to diffuse away. Jang et al. conducted a qualitative FEM modeling of non-uniformly distributed corrosion around the rebar perimeter but extending along the entire rebar length [Jang et al. 2010]. Such a corrosion distribution pattern may be expected in un-cracked concrete due to corrosion initiating on the face of the rebar closest to the concrete cover [Zhao et al. 2011]. The study by Jang et al., contrary to other findings, suggested that much smaller pressure is needed to induce cover cracking compared to evenly distributed corrosion around rebar perimeter. That finding was attributed to pressure concentration due to the uneven distribution of corrosion products around rebar perimeter [Jang et al. 2010]. Nevertheless, there was no experimental evidence provided by that study or found in the literature to validate that FEM-based finding.

2.7 Existing Models for Cover Cracking Induced by Localized Corrosion

2.7.1 Torres-Acosta and Sagüés' Model (2004)

Torres-Acosta's work was the first to experimentally investigate the effect of localized rebar corrosion on the amount of steel corrosion penetration needed for cover cracking [Torres-Acosta et al. 2004]. It was found that when corrosion is localized to a short segment along a reinforcing bar, the amount of corrosion needed for cover cracking (X_{crit}) would be greater than otherwise. Concrete

cylindrical and prismatic specimens with a concrete cover (C) and reinforced with single rebars of diameter (Ø) were tested at a controlled relative humidity environment of ~ 85%. Controlled anodic zones along rebars were represented by central carbon steel segments of various lengths (L). The anodic regions were bounded by either stainless steel or non metallic rebar segments. The anodic zones were forced to corrode in an accelerated fashion by applying anodic current density of ~ 100 μA/cm^2. It was reported that the amount of steel loss needed for cracking was between 30 to ~270 μm for localized corrosion compared to 3 to 74 μm reported previously for uniform corrosion. From the experimental data, an empirical model was proposed for calculating X_{crit} as a function of C/Ø and C/L ratios as follows:

$$X_{crit}/mm \approx 0.011 \left(\frac{C}{Ø}\right) \left(\frac{C}{L} + 1\right)^2 \quad (2.9)$$

The relationship was derived for a range of C/L ratios of 0 to ~ 2. Nevertheless, it did not extend to small enough corroding lengths to approach the narrow corroding spots expected at the bottom of preexisting cracks (i.e. C/L >2). In addition, the previously published data used in that study to supplement the investigation findings for the case of uniform corrosion were based on different experimental anodic current densities, some up to 3000 μA/cm^2. The acceleration by increasing anodic current density can have an effect on the

amount of X_{crit} as explained earlier. The study by Torres-Acosta showed that the amount of rebar radius loss needed for cracking in the case of prismatic specimens is greater than that for cylindrical specimens. This effect may be attributed to the larger effective concrete cover associated with prismatic configuration. The investigator, however, made no distinction between the two kinds of specimens in deriving the relationship. Previously published data compiled by Torres-Acosta were also based on initial surface crack width of ~ 0.05 mm whereas the limit state crack width in Torres investigation was defined as ~ 0.1 mm. The latter requires greater values of X_{crit} to create wider surface cracks and therefore may lead to inaccurate comparisons between findings of different investigations [Alonso et al. 1998]. Further, the reported observation by Torres-Acosta of a scattered pitting along the stainless steel segments used may have influenced the values of X_{crit}. The predictions by Torres-Acosta's empirical model tended to yield overestimated amounts of X_{crit} compared to the reported experimental observations. Further, the empirical nature of the model requires theoretical verification based on modeling the underlying phenomena.

2.7.2 Darwin and O'Reilly's Model (2011)

A recent laboratory work focused on studying the amount of X_{crit} for epoxy-coated rebars (ECR) exposed to corrosion at deliberate coating defects. The coating damage patterns used to simulate generic coating defects were in the form of two holes drilled through the coating, each having a diameter of 3 mm or two defects, each having the shape of a coating damage peeled off half of the rebar perimeter to form half a ring having a band width of 3 mm. The holes or half

rings were spaced 102 mm apart on a 15 mm-diameter epoxy-coated rebar embedded in concrete with one inch cover. The corrosion of steel at the coating defects was accelerated by applying anodic current using a 30 V between the rebar and an auxiliary electrode. There was no information reported however, on the applied corrosion current density. The cover concrete was ponded with de-ionized water throughout the test. The total accumulated mass loss was reported to have been calculated using Faraday's law when a surface crack of 0.05 mm was observed. The specimens were kept under testing even after cracking to allow for monitoring of crack growth. Therefore, autopsy at the end of testing showed significant coating blistering and consequently increased exposed coating areas of holes and half rings by factors of 10 and 2, respectively. The experimental results showed that the rebars with two holes generally need about twice the amount of X_{crit} needed for the rebars with two half rings almost regardless of the exposed steel surface area. The major drawback of this investigation is that there was no gravimetric measurement conducted to confirm the Faradaic-based values of mass loss. It is widely known that the actual mass loss can be significantly different from the mass loss calculated based on the applied anodic current [Alonso et al. 1998 and Torres-Acosta 2010]. Further, the assumption of corrosion loss in the two defects along a corroding rebar to be identical may lead to errors especially in the presence of coating blistering. Coated rebars are associated with uncertainty in the amount of corrosion damage due to wide variation in the extent of coating distress [Sagüés et al. 2006]. Ponding the rebars in water may lead to the formation of soluble corrosion

products as exhibited by rust staining observed on the concrete surrounding the rebar. The soluble corrosion products can diffuse away from the steel-concrete interface and slow down the pressure build-up needed for cracking. Application of models based on those results for atmospherically-exposed RC structures may lead to overestimation of X_{crit}. Further, the addition of air-entraining agents to the concrete mix may provide an additional space in terms of air voids for corrosion products to fill before stresses begin to develop. The latter can lead to increased corrosion tolerance (X_{crit}), compared to concrete mixes without air-entraining agents added.

Darwin et al. conducted a three-dimensional FEM analysis in which a series of non-linear springs were used to provide a horizontal restraint along the plane of crack. The corrosion-induced cover cracking was assumed to initiate alongside the length of rebar. The properties of springs used in the analysis were based on concrete fracture energy, 61 N/m and provided an elastic modulus of 27.6 GPa and an ultimate tensile strength of 2.76 MPa. The concrete behavior away from the crack plane was assumed to be linear and elastic with an elastic modulus of 27.6 Gpa and a 0.2 Poisson's ratio. The relative volume of corrosion product was assumed to be 3 compared to steel. The stresses exerted by expansive corrosion products on surrounding concrete were represented by uniform deflection normal to the rebar surface. A visible crack of 0.05 mm was represented by a horizontal deflection of a point above the rebar at the concrete cover surface by 0.025 mm.

A model for X_{crit} was suggested as a function of concrete cover (C), bar diameter (Ø), fractional corroding length (L_f) and fractional corroding area (A_f) of the total rebar length and area, respectively, as follows:

$$X_{crit}/\mu m = 45\left(\frac{(C/25.4)^{2-A_f}}{Ø^{0.38}L_f^{0.1}A_f^{0.6}} + 0.2\right).\ 3^{A_f-1} \qquad (2.10)$$

where C and Ø are in mm. The model is based on a proposed equation suggested to fit the results from the FEM analysis and experimental data of their own and from literature. The FEM analysis simulated coating damage patterns exposing steel areas of full-ring, half-ring and quarter-ring shapes with localized corroding lengths ranging from 3.2 to 203 mm. The cases tested included concrete covers of 2 and 3 inch and rebar diameters of 0.5, 0.75 and 1 inch. The results of the FEM analysis showed that corrosion loss needed for cover cracking increases as exposed area decreases regardless of the damage pattern which is not in agreement with the reported experimental findings.

In addition to the drawbacks indicated earlier, the equation seems to be extracted from the best fit of experimental data obtained from cases of uniform and localized corrosion ignoring the effect of localization. The literature data used for comparison were corresponding to different limit crack widths such as ~ 0.1mm [Torres-Acosta 2004]. No tolerance seems to have been assumed for the corrosion product to fill the porous transition zone at the steel-concrete interface

before stresses begin to build up. It is also not clear how the fractional values of corroding rebar length (L_f) and area (A_f) can be calculated for real life structures with infinite amounts of entire rebar lengths and areas. The latter brings the applicability of equation (2.10) into question. Further, the FEM model also underestimated the X_{crit} values compared to those obtained experimentally based on Faradaic evaluation of mass loss. For instance, the model yielded a critical penetration value of 200 µm versus experimental values ranging from 350 to 900 µm. Therefore, more research is needed to derive a more practical and reliable relationship for X_{crit}. The rough approximate nature of the Darwin's model predictions does not seem to reflect its level of sophistication which provides no significant advantage in its application over its empirical predecessor [Busba et al. 2013a].

3. EXPERIMENTAL METHODOLOGY[1]

3.1 Introduction

The experimental program was designed to include testing of commercially available reinforced concrete (RC) pipe sections, with mechanically-induced cracks. The test was intended to provide insight on the extent of corrosion localization likely to be encountered in service during exposure to chloride-containing environment. The corrosion testing of the pre-cracked pipe sections was also needed to verify whether corrosion would be uniformly distributed around the perimeter of reinforcing steel at the corrosion influence zone. The exposure conditions were attempted to simulate the most severe conditions that RC storm drainage pipes are expected to encounter in service. Electrochemical impedance spectroscopy (EIS) was used to estimate the instantaneous corrosion currents at various instances throughout the test. Subsequent destructive examination permitted the gravimetric approximation of total mass loss and the calculation of the corresponding average corrosion rate based on the observed influence zone. The short-term corrosion rates, although severely aggravated by accelerated cyclic exposure, were only intended for comparison with the modeled corrosion rate values in chapter 5. The RC pipe experiment was terminated before any corrosion-induced damage was observed due to the long-term nature

[1] Contents include previously published materials in [Busba et al. 2013a and b]. Permissions are provided in appendix C.

of the corrosion process under natural conditions. The major part of the experimental program was focused on testing sound (un-cracked) reinforced concrete cylinders with controlled localized corrosion regions. Various degrees of corrosion localization were tested to determine the individual influence of corrosion localization on critical penetration needed for cover cracking. Therefore, the concrete cover thickness, rebar diameter, concrete quality and exposure environmental conditions were held constant. The controlled anodic regions were forced to corrode in an accelerated fashion using an impressed current system. The presence of localized corrosion along embedded steel in un-cracked concrete represents cases such as at intersections with very narrow preexisting cracks. Localized corrosion conditions may also result from coating holidays in an epoxy coated rebar or from a concrete joint [Lau 2010b, Darwin et al. 2011, Tang et al. 2012 and Mohammed et al. 2003]. It may also be representative of a case where entrapped objects in concrete during construction result in local loss in the alkalinity required for steel passivity [Sagüés et al. 2013].

3.2 Testing of Pre-cracked Reinforced Concrete Pipe Sections

3.2.1 Materials and Specimens

Two RC pipes from a commercially available source were evaluated. Each pipe was 2.4 m long and 45 cm in diameter (ID). The pipes were manufactured in accordance with ASTM C76 [ASTM C76-2011]. The pipe type was class III B-wall having a wall thickness of 63.5 mm. The nominal interior concrete cover (C) and diameter of reinforcing steel wire (Ø) were ~ 25 mm and ~ 4.75mm,

respectively. Table 3.1 lists the RC pipe product materials. The pipe concrete mixture contains about 20% cement replacement of fly ash. This type of RC pipe is intended for highway storm drainage culvert applications requiring service for several decades with minimal interruption for repair and maintenance.

Table 3.1 Concrete mixture proportions of RC pipes as reported by manufacturer

Mix Design Designation # 4000 PSI	
Material Type	Quantity
Cement (kg/m^3)	232
Fly Ash (kg/m^3)	61
Sand (kg/m^3)	1001
Stone (kg/m^3)	1051
Water to Cementitious ratio	0.37

Figure 3.1 illustrates the sectioning procedure of an RC pipe into two pipe rings that were in turn cut into test quadrants. The cutting process was performed using a wet concrete saw. Exposed steel wires at cut edges permitted the determination of the interior concrete cover thickness by direct measurement on the four edges of each quadrant using a ruler. The average value from the four edges for each quadrant specimen was plotted on figure 3.2 to construct a normal distribution of the interior concrete cover thickness for the two pipes under testing. The concrete cover thickness ranged from ~ 9 to 28 mm with an average and standard deviation of ~ 18 mm and 4.5 mm, respectively. Table 3.2 lists the concrete cover thickness values for the individual test specimens as an

average of the measurements from the four edges for each specimen. The sectioned quadrants were subjected to pre-cracking under 3-point bending to create single longitudinal cracks extending along the entire specimen length. The 0.45m-long cracks were oriented along the center of a quadrant in a direction parallel to that from the bell end to the spigot end of a pipe.

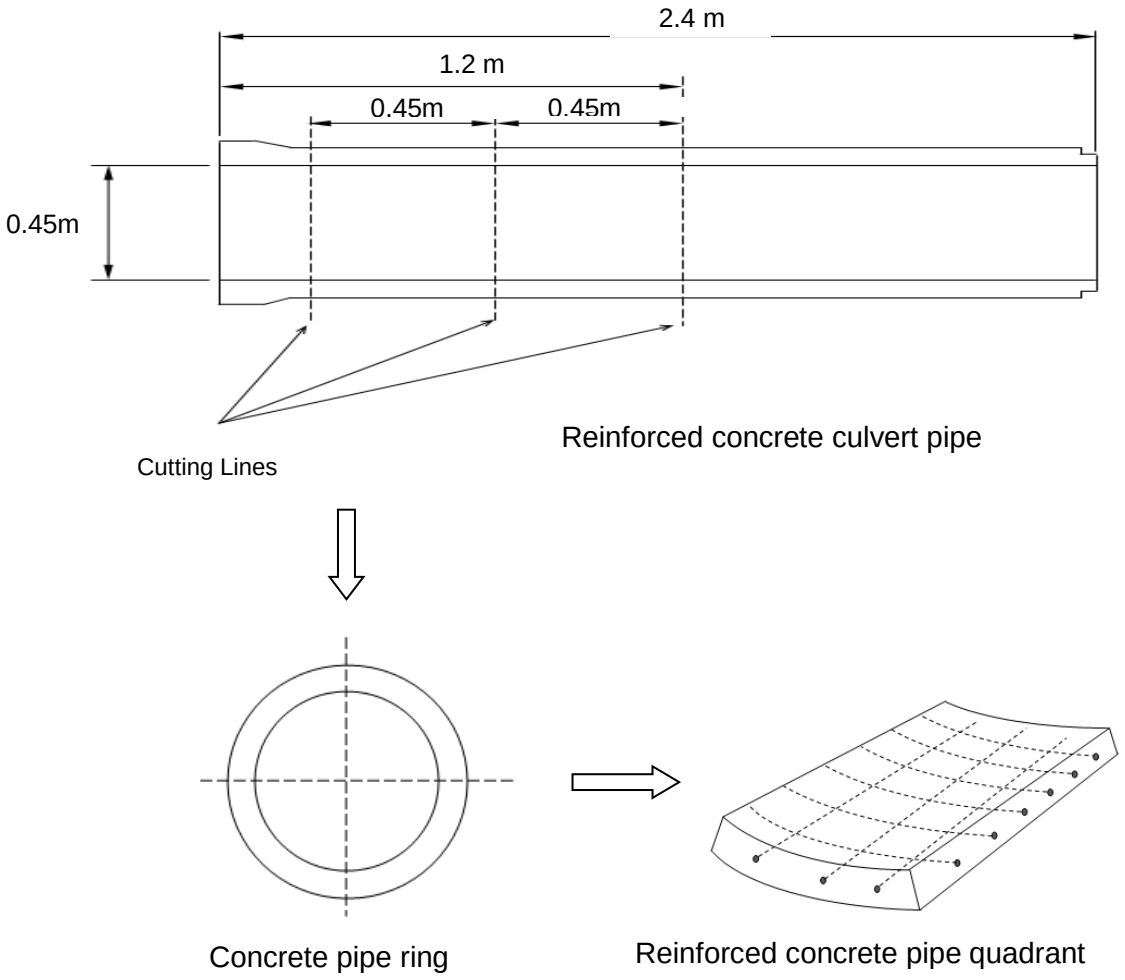

Figure 3.1 Sectioning of RC pipes to produce quadrants

The induced cracks were intended to have controlled average crack widths of 0.5 and 2.5 mm. Those target crack widths were selected to represent typical

crack width values commonly encountered in the RC pipes during construction or early in service for reasons not related to corrosion. Un-cracked specimens were tested in parallel as a control.

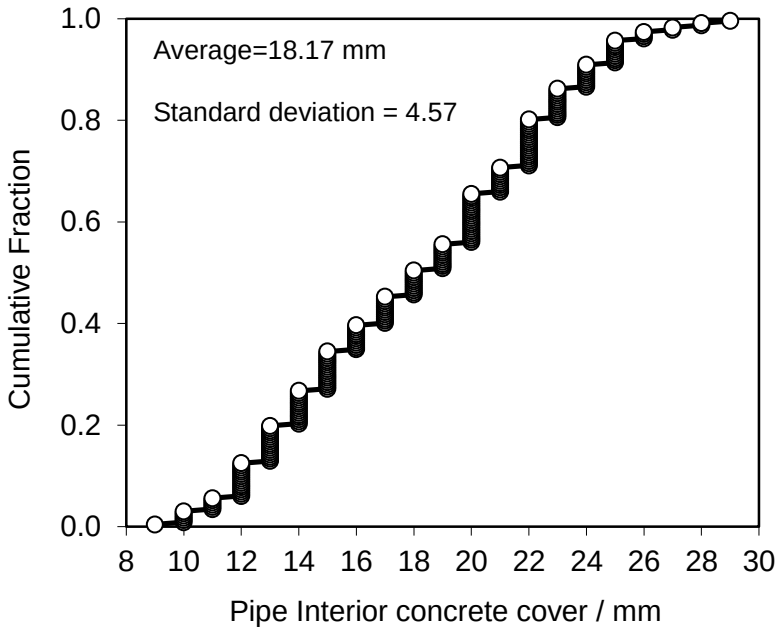

Figure 3.2 RC pipe interior concrete cover thickness measured on edges of specimens

Figure 3.3 shows the mechanical cracking rig employed to create cracks using three-point bending. The cracking rig was operated using an MTS 810 machine (model no. 204.91). Figure 3.4 illustrates the orientation of generated cracks and the intersection of crack with the reinforcing steel. Monitoring of the obtained crack widths was performed during loading using a crack gauge composed of two metallic nuts glued around the specimen centerline (figure 3.6). Upon completion of the cracking process, confirmatory detailed measurements of crack width and depth were undertaken by means of a crack comparator and a

proprietary insertion gauges, respectively. The insertion gauge for estimating crack depth was a 0.3 mm-diameter wire.

Figure 3.3 Three-point bending process used to generate cracks on the interior surface of the pipe quadrant specimens

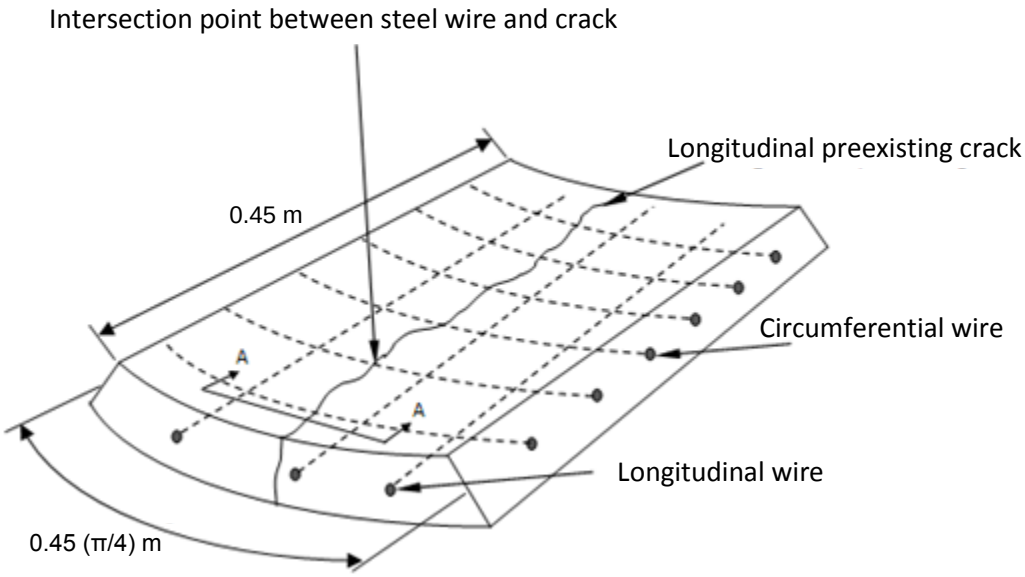

Figure 3.4 A schematic diagram for the mechanically-generated crack on a pipe specimen and the resulting crack-wire intersections

The induced cracks were found to have intersected and reached the depth of the embedded steel. The measurements were performed at 12 mm intervals

along the crack. Table 3.2 lists the average values of those crack width and depth measurements. The individual crack width measurements for each cracked specimen are shown in figure 3.5.

Figure 3.6 exemplifies the exposure ponds of Plexiglas that were attached to both cracked specimens and control specimens. The ponding footprint area to be exposed to the test medium was 23 cm x 35.5 cm. In order to prevent leaking, the sides of each pond were sealed with silicone sealant. Likewise, the crack ends outside the footprint area and the back side of specimens were also sealed with epoxy. The minimum level of test solution within the footprint zone was about 25 mm.

Table 3.2 Characteristics of generated cracks in the RC pipe specimens

Specimen #	Target crack width	Average concrete cover	Achieved crack Width		Average achieved crack depth
			Average	Standard deviation	
R7	0	21.5	-	-	-
R10		17.1	-	-	-
R3	0.5	18.6	0.71	0.15	8.4
R6		20.2	0.45	0.07	6.4
R12	2.5	18.8	2.7	1.24	32.7
R4		23.8	1.7	0.38	28.5

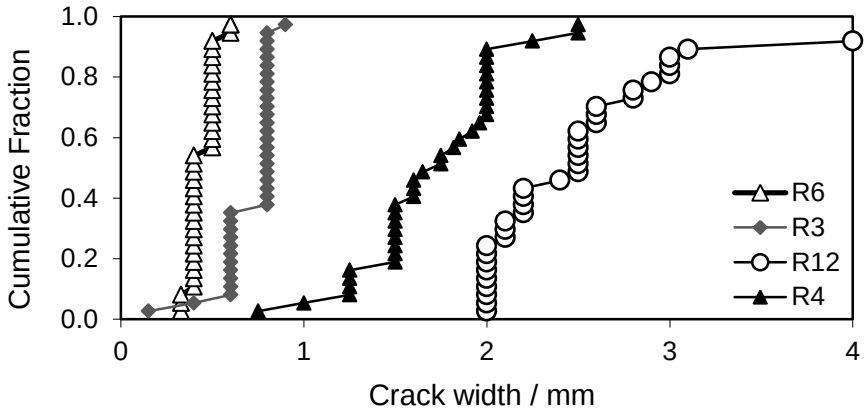

Figure 3.5 Crack width measurements for each individual cracked specimen

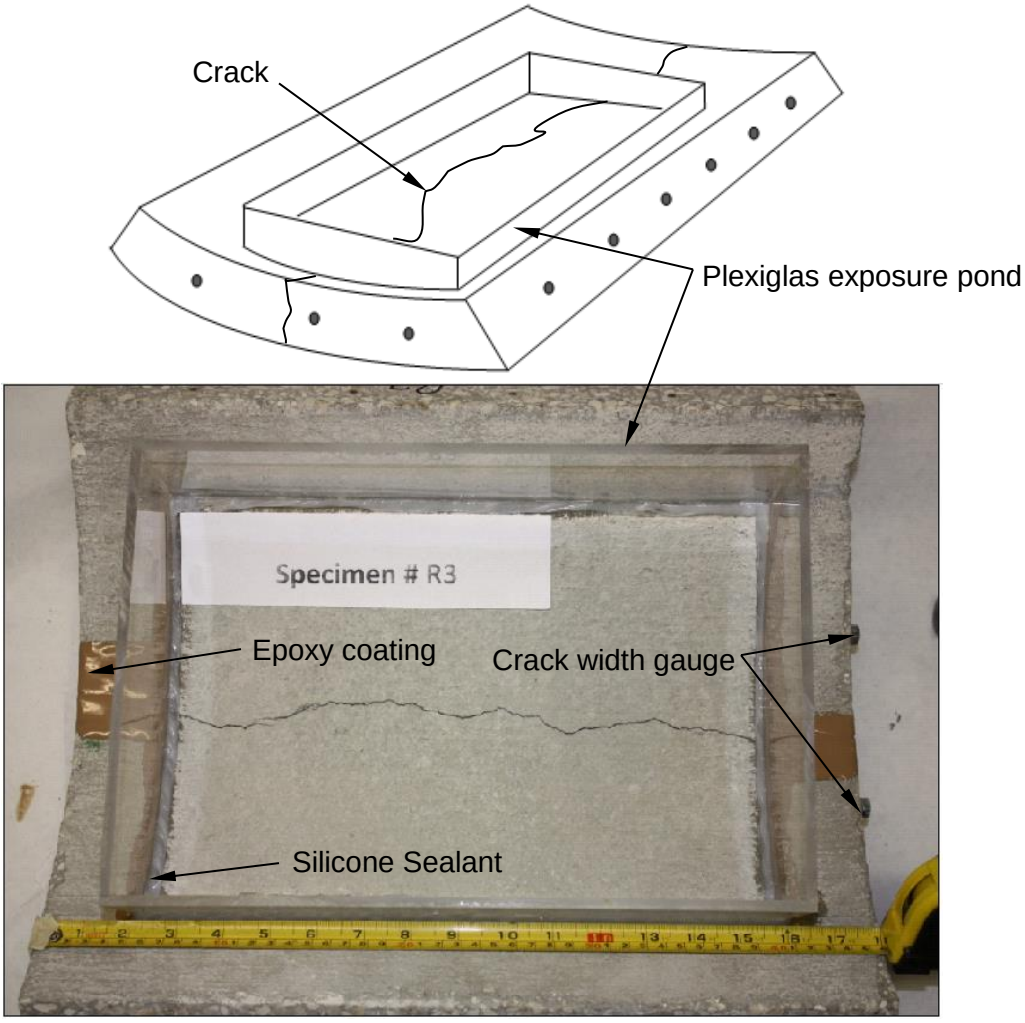

Figure 3.6 Ponding footprint exposed to test solution for the cracked and control specimens

3.2.2 Environmental Exposure

The duplicate control and cracked specimens shown in table 3.2 were tested to evaluate possible levels of corrosion. The specimens were initially exposed to continuous ponding to de-ionized (DI) water for a period of 33 days. This initial exposure was intended to allow the potential of reinforcing steel to reach a steady state in a slightly corrosive environment before the long-term exposure to a chloride-containing environment. The initial ponding was intended to obtain an insight on the corrosive effect to be expected upon exposure to more corrosive conditions in the main testing scheme. The entire experiment was conducted at lab temperature of ~ 25^{o}C. At the end of the initial exposure period, the DI water was replaced with a sodium chloride solution having a chloride ion concentration of 500 ppm. The specimens were subjected to continuous ponding of that chloride solution for 115 days. The chloride solution was nearly neutral initially and stabilized to a pH of about 8.7 after one month of exposure. The period of continuous ponding to chloride solution was followed by intermittent ponding to the same solution. The intermittent exposure period extended for seven cycles on a one week dry / one week wet basis. A new chloride solution was used for each wet cycle throughout the entire cyclic exposure regime so as to avoid changes to the solution due to evaporation or contaminants released from concrete. The intermittent exposure regime was adopted to address the possible increased corrosivity of chloride-containing aqueous media due to evaporative chloride concentration [Sagüés et al. 2001 and Glass et al. 1997]. Storm drainage culvert RC pipes may not normally be expected to encounter

such an excessive wet / dry cycling in service. However, the accelerated cycling was required to evaluate the possible level of corrosion damage severity and its morphology when corrosion becomes localized at crack-steel intersections under natural exposure conditions.

3.2.3 Electrochemical Corrosion Assessment

Steel open circuit potential (OCP) was measured at all exposure regiems using a saturated calomel reference electrode (SCE). The reference was placed at the center of the ponding footprint with the tip of the reference immersed in test solution and touching the concrete surface. Steel potential mapping was conducted over the exposed footprint area on a grid having 25 mm x 25 mm intervals. Due to its limitation as a corrosion characterization method, performance of OCP measurements were intended for initial corrosion evaluation of the embedded steel without information provided on corrosion rate [ASTM C876-2009, Gonzales et al. 2005, and Song et al. 2007]. Electrochemical Impedance Spectroscopy (EIS) is a technique used to measure the corrosion current of steel reinforcement and was applied here for measurements at all exposure environments [Mansfeld 1988 and Sagüés 1993]. The EIS test was performed by means of the Solartron® impedance equipment (Potentiostat and Analyzer SI 1287 & SI 1260). The impedance measurement was mainly run over a frequency spectrum ranging from 1000 Hz to 1 mHz. The low frequency end of the spectrum was selected to enable detailed sampling of information at that end which is typically of importance for determining corrosion rates. Due to the time-consuming nature associated with conducting EIS extending to very low

frequencies, initial EIS test sessions were conducted over narrower frequency ranges for quicker measurements. The initial quick EIS frequency ranges had an upper end of 1000 Hz and lower ends of 10 mHz (during exposure to DI water) and 3 mHz (during exposure to chloride solution).

The amplitude of EIS excitation signal was 10 mV with data sampling frequency being either 4 or 5 points/decade. An SCE reference electrode (RE) was immersed in test solution in a position same as that used for potential measurements. An activated titanium [Castro et al. 1996] mesh as a counter electrode (CE) was immersed in the test medium and was resting over the entire test footprint. The embedded reinforcing steel served as the working electrode (WE). Figure 3.7 shows a schematic illustration of the EIS test setup. The OCP and EIS testing were conducted on a daily and a weekly basis, respectively. For cyclic exposure however, testing was conducted only during wet exposure periods.

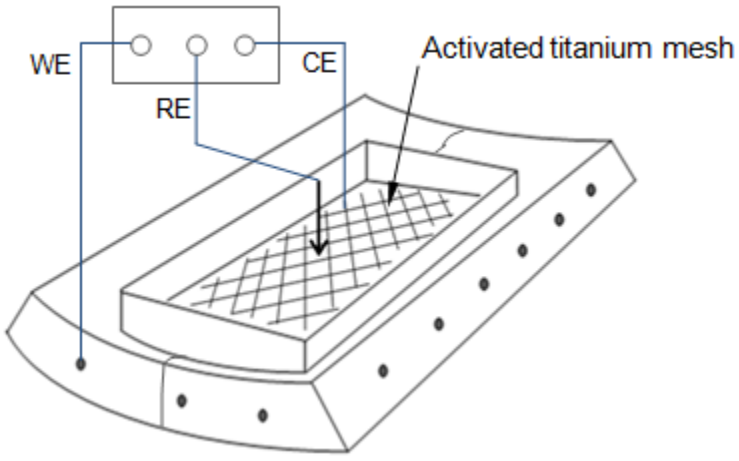

Figure 3.7 Electrochemical impedance spectroscopy (EIS) test setup

The simplified electrochemical equivalent circuit shown in figure 3.8 was applied for interpreting the EIS data. The equivalent circuit is represented by a solution resistance (Rs) in series with two parallel components of a polarization resistance (Rp) and a constant phase element (CPE). The Rp component is related to the corrosion process whereas the CPE component represents a non-ideal interfacial capacitance [Sagüés 1993].

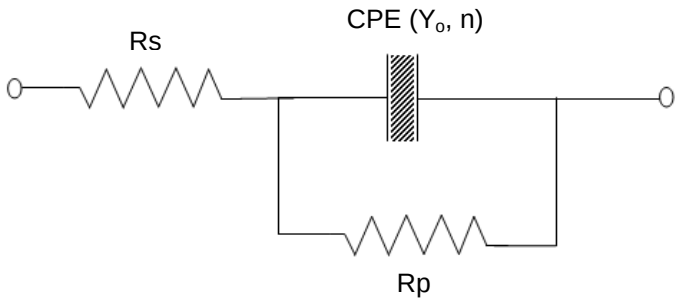

Figure 3.8 Simplified equivalent circuit applied for fitting and interpreting EIS data

The total impedance (Z_T) of the equivalent circuit is calculated by:

$$Z_T = R_S + \frac{1}{Y_o(j\omega)^n + \frac{1}{R_P}} \quad (3.1)$$

where Rs is solution resistance, Rp is polarization resistance, $j = (-1)^{0.5}$ and $\omega = 2 \pi f$, (f being frequency). Y_o and n are CPE component parameters. The parameter (Y_o) is a constant depending on the interfacial properties and has the unit of (Sec^n / Ohm). The parameter (n) is a real number with a value ranging from 0 to 1. The EIS parameters Rs, Rp, Y_o and n were calculated by fitting the

experimentally measured values of total impedance Z_T over a selected range of frequencies to the values of total impedance obtained from the equivalent circuit over the same frequency range. In general, the frequency range evaluated was selected to incorporate the impedance data measured over a frequency range of 10 mHz and below. The EIS data, however that were measured over a range having a lowest frequency end of 10 mHz, an approximation procedure was developed to calculate the respective polarization resistance values associated with those cases (appendix A.1). Further description of that approximation procedure may be found in a report previously published by the author [Busba et al. 2011]. The data fitting was performed using the commercially available EIS data analysis software, Zview®, V3.2 C. The average corrosion current (I_{corr}) was calculated using Stern-Geary equation given by [ASTM G 102 – 89]:

$$\mathrm{I_{corr}} = \frac{\mathrm{B}}{\mathrm{R_P}} \tag{3.2}$$

where, B is Stern-Geary coefficient which is estimated by a value of 0.26 V for active corrosion of steel in concrete [Andrade et al. 1989]. The average corrosion rates over the entire test duration were estimated later upon subsequent destructive examination using the actual surface area affected by corrosion as described next.

3.2.4 Direct Corrosion Assessment

Regular monitoring of cracked specimens was performed to check for visible evidence of corrosion. At the end of testing, the cracked specimens were

subjected to destructive examination by demolishing the concrete and extracting the embedded steel to confirm and quantify any corrosion damage. The extent of corrosion localization and distribution around the embedded steel in the corrosion influence zone was examined. The reduction in steel reinforcement diameter was estimated by means of a digital caliper and confirmed by the analysis of detailed magnified images of the affected region. For each specimen, the total observed amount of actual mass loss was calculated and compared with the nominal total mass loss estimated based on Faraday's law using the integrated I_{corr} data for the same specimen. Calibration factors (Fc) were then derived for each nominal crack width, accordingly. A generic calibration factor (Fc) was obtained by averaging as a universal value for the calibration of the EIS-estimated corrosion current for each individual cracked specimen. In order to obtain information on corrosion rate evolution with time, the instantaneous corrosion currents estimated by equation (3.2) were calibrated. The calibration was performed for the average current over the period of each exposure environment using Fc obtained based on the actual amounts of corrosion observed.

Similar sets of cracked and control RC pipe specimens from a different manufacturer were evaluated in parallel with the specimens reported here. However, the results of those were not considered here due to the presence of issues introduced by consolidation voids around steel causing corrosion to be mainly uniform along embedded steel. The findings of those cases were published by the author elsewhere [Busba et al. 2013b].

3.3 Corrosion-induced Cracking of Sound Reinforced Concrete Cylinders

3.3.1 Materials and Specimens

Reinforced concrete cylinders were selected for testing due to their widely accepted configuration in previous investigations dealing with the corrosion-induced cracking phenomenon [Chernin et al. 2011, Pantazopoulou et al. 2001, Munoz et al. 2007, Balafas et al. 2011, Bhargava et al 2006 and Lu et al. 2011]. Figure 3.9 illustrates a test specimen with a single central reinforcing smooth round bar with a controlled uniform concrete cover thickness surrounding the reinforcement. The presence of a single rebar would enable fundamental understanding of the individual effect of localized corrosion of a rebar on cover cracking without the complicating factors of parallel rebars or stirrups being present. The uniform concrete cover thickness represents the minimum concrete cover thickness in a reinforced concrete member. Experimental testing of reinforced concrete members with more sophisticated reinforcement configurations were not considered at this stage due to lack of basic knowledge in literature on cover cracking resulting from localized corrosion.

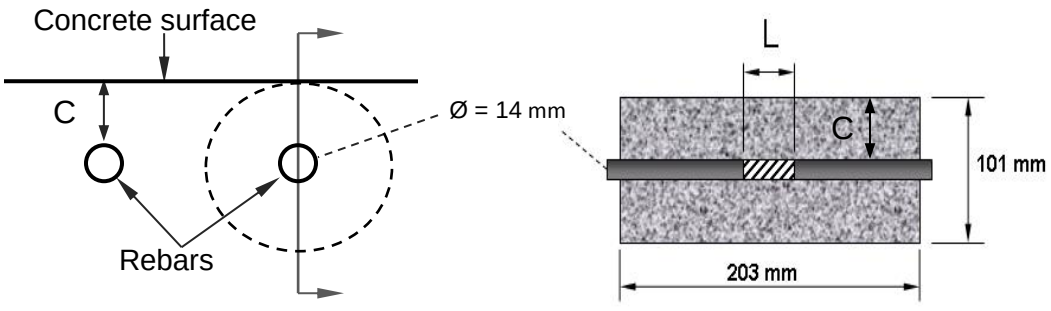

Figure 3.9 Test specimen configurations

The dimensions of test specimens were 101 mm in diameter and 203 mm in height with a concrete cover (C) of about 43 mm. The axial composite smooth metallic bar had a diameter (Ø) of about 14 mm. The reinforcing bar is composed of a central carbon steel segment having a length L representative of the localized anodic region. In order to control the degree of corrosion localization, the carbon steel segment was axially bounded by two segments of highly corrosion resistant nickel-based alloy (Hastelloy ® Alloy C22, UNS 06022) [Badwe et al. 2006]. The C22 alloy segments represented the adjacent passive (non-corroding) regions along the rest of the embedded rebar. The highly corrosion-resistant C22 alloy was selected to avoid the pitting issues associated with the relatively less corrosion-resistant stainless steel previously used in similar investigations [Torres-Acosta et al.1999 and 2004].The carbon steel segments were machined from a regular deformed rebar (figure 3.10 a) manufactured according to ASTM-A615M-03A with a size designation no. 7 (Customarily known as rebar no. 7) [ASTM A615-2003]. The chemical compositions of the carbon steel rebar and C22 alloy are listed in table 3.3 according to the mill certificates provided by respective manufacturers. Part of the reason why the carbon steel segments were prepared from a commercial product of steel rebar was obviously to obtain an electrochemical behavior representative to that expected in practice. Further, carbon steel extracted from non-rebar steel sources may include some elements uncommonly present in rebar steel. There is evidence in the literature that the presence of such uncommon elements may result in significant variation in estimating the actual

mass of lost steel. That variation is attributed to over-cleaning issues during the subsequent removal of corrosion product with the Clarke's solution of ASTM- G1 at the end of testing [ASTM G1-2003 and Singh et al. 2003]. The relatively high amounts of mass losses reported in previous similar investigations, that involved the use of anodic steel segments fabricated from steel pipes, may in part be attributed to that issue [Torres-Acosta 1999]. More details on that phenomenon will follow in the chapter of results and discussion.

Table 3.3 Chemical compositions of composite rebar materials

Carbon steel rebar*

Specification ASTM-A615M-03A												
C	Mn	P	S	V	Si	Cr	Cu	Ni	Sn	Al	Mo	Fe
0.41	0.85	0.017	0.054	0.02	0.18	0.14	0.4	0.09	0.013	0.045	0.017	Bal.

* (Grade 420 Mpa with carbon equivalent CE=0.58)

C22 Alloy (Hastelloy)

Specification UNS N06022											
C	Co	Cr	Fe	Mn	Mo	Ni	P	S	Si	V	W
0.002	0.54	21.5	3.6	0.25	13.1	Bal.	< 0.01	0.004	0.02	< 0.01	2.8

The carbon steel segments were mechanically attached to the two outer C22 segments as illustrated in figure 3.10 b. The mechanical connection was made by means of an 8 mm - 18 thread type 316 stainless steel rod passing through a concentric borehole in the carbon steel segment. The threaded rod was tightened into threaded holes within the adjacent ends of the outer segments of C22 alloy. Pitting of stainless steel connection rod was not an issue here since

that rod did not have any contact with the concrete medium. The three segments of each composite rebar were sufficiently tightened together with a torque wrench to avoid any possible crevice formation at the two intermediate joints.

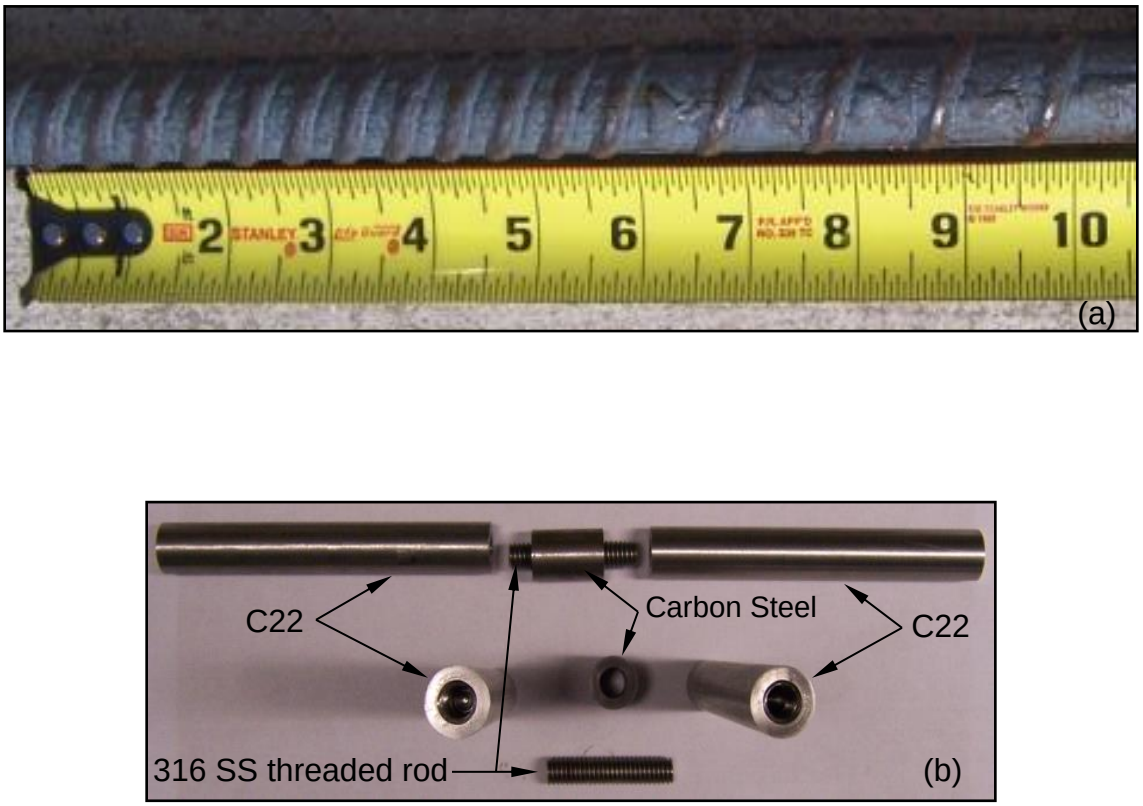

Figure 3.10 Components of composite bar. (a) deformed rebar machined to make the carbon steel segments and (b) exploded view

The length of anode segment (L) was designed to represent the case of uniform corrosion and various cases of localized corrosion such as those likely to be encountered at intersections of steel with preexisting narrow cracks [Busba et al. 2013b]. The lengths (L) of anodic regions were selected so that the ratios of concrete cover to length of anodic zone (C/L) become equal to about 0.2, 1, 2, 3,

4 and 5. Those ratios represent cases of various degrees of corrosion localization ranging from uniform (0.2) to highly localized (5). The test specimens intended to simulate uniform corrosion were made up of single bars of carbon steel along the entire embedded length. The range of C/L ratios considered included previously tested cases of localized corrosion (C/L=1 to ~ 3) in order to calibrate the existing empirical relationship and adjust it to apply for the broader range [Torres-Acosta et al.2004]. The machined carbon steel segments were surface finished with 800-grit sand paper and cleaned with acetone before concrete casting according to the procedure of ASTM G01-03 [ASTM G01-2003]. In order to examine the possible influence of the deformed configuration of regular rebars, a parallel set of specimens were subjected to uniform corrosion along the entire length of deformed rebars. The tested deformed rebars had a designation size no. 5 for closest nominal diameter (~ 15 mm) approaching that of the smooth bar test specimens. The test rebars had the same specification as that of the rebar (no. 7) used for preparing the smooth carbon steel segments. However, the test rebars were used in the as-received surface condition for concrete casting. The bar ends sticking out of concrete in all cases of uniformly corroding specimens were coated with epoxy. The reason for not using deformed rebar carbon steel segments for all test specimens instead of the smooth round bars will be discussed in section 3.3.2.5 and in chapter 4. In preparation for subsequent cable connection during testing, a stainless steel bolt (M 3.5 – 0.06) was mechanically attached to one of the outer rebar ends to ensure a good electrical contact. All specimens were tested in triplicate for reproducibility

purposes. Table 3.4 shows the matrix of test specimens, dimensions and the initial carbon steel weights needed for subsequent mass loss calculations.

In order to enable comparisons of the present findings with literature, the concrete compositions as well as curing and testing procedures were attempted to mimic the test conditions of a similar previous work [Torres-Acosta et al. 2004]. The concrete casting of test specimens was performed using cylindrical plastic molds with the composite rebar held at the centerline of the cylinder. The cylindrical molds were kept in a vertical position during concrete casting to minimize bubble formation and bleeding at the rebar / concrete interface. An additional group of non-reinforced concrete specimens were prepared to allow for subsequent destructive testing for compressive and splitting tensile strengths as well as exact determination of actual admixed chloride levels. All specimens were placed on a vibrating table for 45 seconds after casting to release any trapped air bubbles. Table 3.5 lists the concrete mixture compositions and proportions as well as the compressive and splitting tensile strengths measured after 28 days [ASTM C39-2003 and ASTM C496-2011]. A chloride contamination level was introduced by admixing sodium chloride with the concrete mixture to assist in activating corrosion of anodic zones during anodic polarization. The chloride ion concentration was intended to exceed the typical literature-reported value of 0.4 % by weight of cement for corrosion chloride threshold of rebar steel in concrete [Glass et al. 1997]. The actual levels of chloride ion concentrations determined by chloride analysis in accordance with a standard test procedure are listed in

table 3.5 [FM5-516-2009]. All the test specimens were cured by keeping them in a moist chamber for 4 weeks after removing them from their plastic molds.

Table 3.4 Test specimens and initial weights of anodic segments

Type of Corrosion	Specimen #	Ø/ mm	Nominal L /mm	Nominal C/L	C/Ø	Initial weight of steel / g
Localized Smooth bar	101	14.27	43.73	1.00	3.06	37.215
	102	14.28	43.7	1.00	3.06	36.840
	103	14.3	43.6	1.00	3.05	36.840
	201	14.23	21.62	2.02	3.07	18.197
	202	14.23	21.61	2.02	3.07	18.327
	203	14.27	21.7	2.01	3.06	18.378
	301	14.31	14.77	2.95	3.05	12.517
	302	14.32	14.55	3.00	3.05	12.402
	303	14.32	14.75	2.96	3.05	12.535
	401	14.29	10.65	4.10	3.05	9.017
	402	14.3	10.6	4.12	3.05	8.965
	403	14.3	10.5	4.16	3.05	8.845
	501	14.22	8.57	5.10	3.07	7.124
	502	14.22	8.58	5.09	3.07	7.189
	503	14.25	8.61	5.07	3.06	7.224
Uniform Smooth bar (1st set)	U1	14.12	203.2	0.215	3.09	280^{+}
	U2	14.05	203.2	0.215	3.1	277.6^{+}
	U3	14.05	203.2	0.215	3.1	277.8^{+}
Uniform Smooth bar (2nd set)	U4	14.13	203.2	0.215	3.09	277.3^{+}
	U5	14.32	203.2	0.215	3.05	284.9^{+}
	U7	14.03	203.2	0.215	3.11	279.7^{+}
Uniform (Deformed rebar)	R1	15.88*	203.2	0.21	2.7	348.2^{+}
	R2	15.88*	203.2	0.21	2.7	347.2^{+}
	R3	15.88*	203.2	0.21	2.7	338.1^{+}

* Nominal diameters, + Initial weight of entire bar including the ends of bar sticking out of concrete cylinder without the epoxy coating (~12.5 mm on each side).

Table 3.5 Concrete mixture compositions and mechanical properties

Material	I	II
Cement, kg/m^3 (Type I)	426	426
Water, kg/m^3	201	200.5
Water to cement ratio (W/C)	0.47	0.47
Coarse Aggregate, kg/m^3 (Lime stone # 89) [ASTM C33]	949	949
Fine Aggregate, kg/m^3 (Silica sand)	676	676
Total chloride ion content, % by weight of cement (As part of sodium chloride) [FM5-516-2009]	1.1	2.43
Entrained air content %	5.7	4.3
28-day Compressive Strength, MPa [ASTM C-39]	38.93	45.9
28-day Tensile splitting strength, MPa [ASTM C496]	-	4.438

N.B. (I): batch used for the cases of localized corrosion and the first set of uniformly corroded smooth bars. (II): batch used for the uniform corrosion of deformed rebars and the second set of uniformly corroded smooth bars.

3.3.2 Experimental Procedure

3.3.2.1 Acceleration of Corrosion and Exposure Conditions

In order to force the carbon steel to corrode in an accelerated fashion, the embedded bars were polarized by applying constant anodic current. The anodic current density was designed to achieve a target value of 100 μA/cm^2 [Alonso et al. 1998 and El Maaddawy et al 2007]. That corrosion current density was thought to cause sufficient acceleration but without introducing exotic electrochemical phenomena irrelevant to the natural process of steel corrosion in concrete [Lazari et al. 2000].

The current to be applied was considered to be only possible to flow through the carbon steel-concrete interface in terms of corrosion current with negligible amount passing through the C22 alloy-concrete interface. The total current to be applied was therefore calculated to achieve the target current density, for each specimen, based only on the surface area of the carbon steel. An impressed current system was designed with multiple channels to provide the required current for each case under galvanostatic control. Figure 3.11 shows the configuration of the counter electrode (CE) used as a means of passing current through concrete. The counter electrode composed of two 50 mm-wide conductive rubber bands held firmly in place by aluminum collars [Bains et al. 1989]. The rubber bands were spaced apart around the middle of a specimen by a distance of 25 mm to allow for regular monitoring of surface cracking over the center of the anodic spot.

A FE analysis was performed to ensure that the selected CE geometry provides a uniform current distribution for the various lengths of carbon steel segments. For numerical simulation purposes, a concrete resistivity typical of the material used was assumed to be in the order of 100 ohm-m and the C22 segments assumed to demand no current (surface-isolated). The numerical results for the actual CE geometry were compared with those for a case where the counter electrode was covering the entire concrete surface. The comparison suggested that the selected geometry of CE is capable of providing nearly uniform current distribution. The FE results are shown in appendix A.2.

The values of experimental applied currents shown in table 4.2 were found to be fairly constant within ± 1% of the target values. The applied voltage between the embedded bar and the counter electrode was initially found to be about 1.5 to 2 Volts. The amount of admixed chloride ions indicated earlier was required to be greater than the 0.4 % by weight of cement based on the literature-reported value for rebar steel in concrete [Glass et al. 1997]. The chloride ion addition would assist in lowering the pitting potential and breaking the passive layer under the applied constant current [Jones 1996]. Therefore most of the applied current can be consumed in turning steel into rust and thereby increase current efficiency [Nossoni et al. 2012]. Due to the nature of smooth surface finish and the effect of small size of the carbon steel segments, a higher value of chloride corrosion threshold may be needed to trigger corrosion [Li et al. 2001 and Angst et al. 2011a]. The chloride concentration however is expected to increase further at the bar – concrete interface as chloride ions transport towards the embedded bar by migration under the applied electric field. At the end of testing, two concrete samples were extracted from two locations along the radial direction at the center of a selected specimen after autopsy. The concrete powder samples were subjected to chloride analysis to confirm the expected increase in chloride ion concentration towards the inner regions close to the rebar.

The concrete specimens were placed in a test chamber (figure 3.12) controlled at a relative humidity of 85 ± 5% for a period of ~ 6 months (1 month for the deformed rebar and for the 2nd set of uniform specimens). The specimens

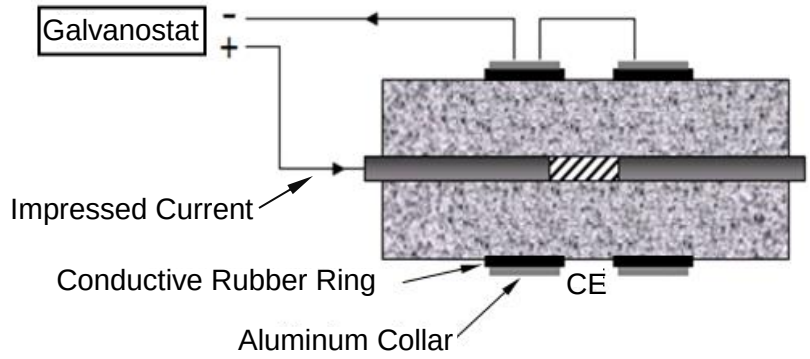

Figure 3.11 A schematic illustration of impressed current circuitry. The shaded central area along the rebar represents the localized anodic region

Figure 3.12 Test specimens under impressed current in a controlled RH chamber

were intended to stabilize before energization of current. The value of 85% RH was chosen in part because it is reported in the literature to be the point of highest corrosion risk [CEB 1985]. The required RH was achieved by blowing air on a beaker of saturated solution of potassium chloride (KCl) placed in an air-tight chamber [Young 1967]. Regular monitoring of RH was made using a Psychrometer device [ASTM E 337-1984]. The specimens were tested at an average lab temperature of ~ 22^{O}C.

3.3.2.2 Detection of the Onset of Corrosion-induced Cracking

Once the specimens have been subjected to anodic polarization, the applied current and voltage were monitored on a daily basis until corrosion-induced cracking appeared on concrete surface. Daily visual monitoring for appearance of surface cracking was performed. Specimens were disconnected and extracted for detailed microscopic examination utilizing a graduated optical microscope with 100X-magnification on a biweekly basis. The microscopic examination was required to check for invisible cracks and to accurately measure crack width.

Cracking was found to be associated with gradual increase in applied voltage immediately before it appeared on the concrete surface which in turn provided an early evidence of cracking. That increase may be attributed to an increase in concrete resistance when cracks begin to emerge at the rebar – concrete interface [Torres-Acosta 2010]. Once the crack width at the surface of a specimen has reached a value of ~ 0.1 mm, the specimen was permanently disconnected for detailed examination. The surface crack was traced on a transparent paper for later comparison of its orientation with the steel corrosion morphology.

3.3.2.3 Corrosion Evaluation and Estimation of Critical Penetration (X_{crit})

The cracked specimens were demolished to retrieve the carbon steel segments for inspection of corrosion morphology and for gravimetric evaluation of mass loss. The extent to which the steel corrosion product has radially

transported into surrounding concrete was visually examined. The surface area of corroded carbon steel regions was estimated by the area covered by the steel corrosion product which was confirmed after rust removal and adjusted if required. Further, the extent of steel corrosion product transporting sidewise on each side of the carbon steel segment along the adjacent C22 alloy segments was inspected and measured.

Subsequently, the steel corrosion product was removed off the surface of carbon steel segments in accordance with the procedure of ASTM G1-03 [ASTM G01-2003]. The measured amount of lost steel mass in grams, Δm_G, was estimated by subtracting the final weight measured after cleaning from the initial weight in table 3.4. The theoretical mass loss of steel, Δm_F, resulting from the applied current was calculated based on Faraday's first law of electrolysis (equation 3.3). The corrosion current efficiency was evaluated according to equation 3.4.

$$\Delta\, m_F = \frac{M}{n.F}\, I.t \qquad (3.3)$$

where the term (M/nF) is referred to as the electrochemical equivalence of the iron substance (assuming the steel is pure iron), (M) being the molar mass of iron (M=55.847 g/mol), (n) is the effective valence of the iron ions dissolving (n=2) and (F) is Faraday's constant which is made up of the product of the electron charge by the Avogadro's number (F=96485 C/equivalent). The term (I.t) represents the electric charge, where (I) is the applied anodic current in amperes

and (t) is the time in seconds during which the current has been passed through the circuit.

$$\text{Current Efficiency} = \frac{\Delta m_G}{\Delta m_F} \quad (3.4)$$

The distribution of corrosion along and around the perimeter of carbon steel segments was examined and detailed images taken. When the entire surface of carbon steel segment was affected by corrosion (figure 3.13a), the average value of X_{crit} was simply estimated by:

$$X_{crit} / \mu m = \frac{\Delta m_G . 10^4}{\rho \pi \emptyset L} \quad (3.5)$$

where ρ is the density of iron (ρ =7.858 g/cm^3) and Ø & L are the diameter and length in cm of the carbon steel segment, respectively. Since the value of X_{crit} is typically in the order of µm and much smaller than Ø, the effect of bar surface curvature on volume – depth relationship was ignored. On the other hand, when the carbon steel segment exhibited only partially corroded surface area (figure 3.13b), (i.e. corrosion not covering the entire perimeter), two approximate approaches were used to estimate the value of X_{crit} [Busba et al. 2013a]. The actual surface areas (Ac) of partially corroded steel segments were measured using the image analysis computer software – Image J ®.

For the instances of partially corroded surface area A_C (less than πØL), the two proposed approaches were applied. The approaches presented two alternative cases equivalent to the case of partially corroded surface but with the surface area of the carbon steel segment entirely corroding around its perimeter.

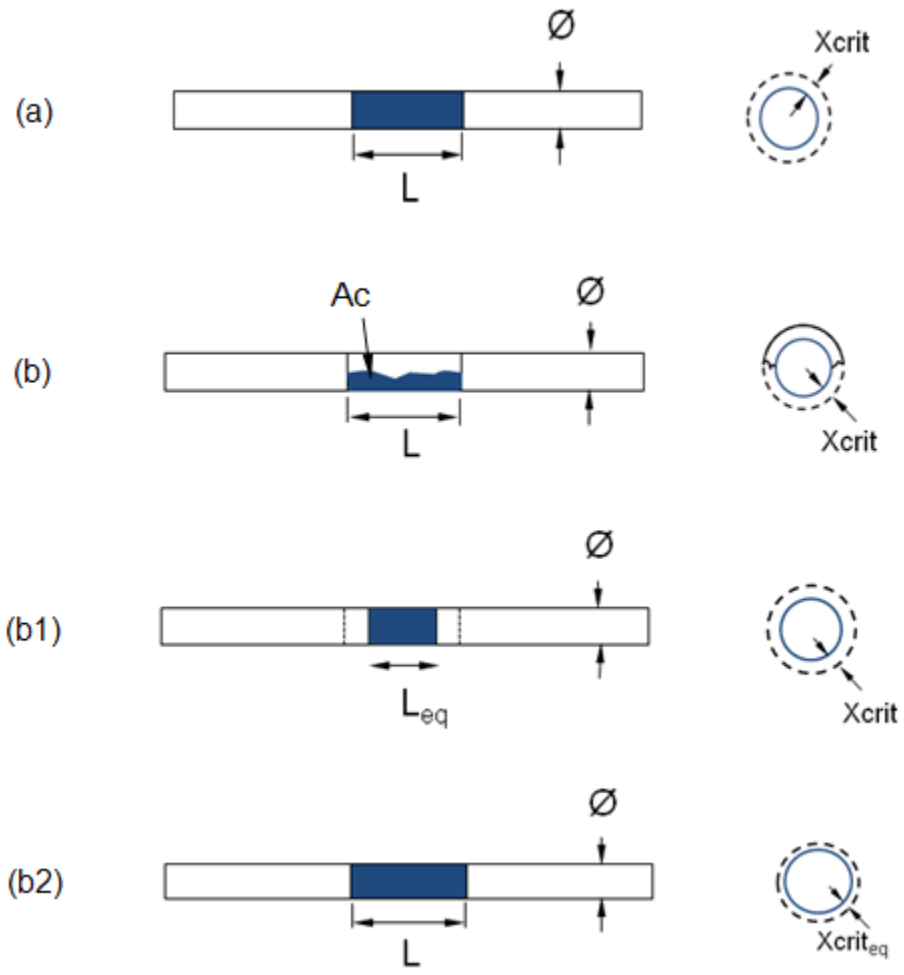

Figure 3.13 Illustration of corrosion distribution around rebar perimeter showing (a) entirely and (b) partially corroded surface area of steel bar segment. Approximate approaches (b1) and (b2) used as equivalent cases to case (b).

In approach 1, the actual corroded region (Ac) in figure 3.13 (b) is assumed to be equivalent to a case where corrosion affects a shorter segment (L_{eq}) but covering the entire perimeter. The depth of average penetration (X_{crit}) remains

unchanged to keep the consumed steel volume same as the estimated amount. According to approach 1 in figure 3.13 (b1), the average X_{crit} and the equivalent length of segment experiencing entirely corroded surface are given by equations 3.6 and 3.7, respectively.

$$X_{crit} / \mu m = \frac{\Delta m_G . 10^4}{\rho . A_C} \quad (3.6)$$

$$L_{eq} = Ac/(\pi \emptyset) \quad (3.7)$$

In approach 2, the effect of partially corroded surface area in figure 3.13 (b) is assumed to be equivalent to a case in which corrosion entirely covers a segment having the same diameter Ø and the same length L. The surface however experiences a smaller depth of penetration (X_{crit} eq) to maintain a constant volume of lost steel as that estimated experimentally. According to approach 2 in figure 3.13 (b2), the equivalent average value of critical penetration (X_{crit} eq) is given by:

$$X_{crit}\ eq / \mu m = \frac{\Delta m_G . 10^4}{\rho . \pi . \emptyset . L} \quad (3.8)$$

The results obtained from applying the above two approaches were compared later with literature data obtained from cases where the localized anode segments experienced corrosion nearly on their entire surfaces. In the following chapter, the generic term X_{crit} will be used to represent both X_{crit} and X_{crit} eq. Similarly, the generic term L will be used to represent L and Leq. The ratio of concrete cover to the actual corroded length will be referred to as C/L. Nevertheless, the specimen group names will frequently be referred to in terms of the ratio of concrete cover to the nominal length of carbon steel segment. In the latter, the ratio would be referred to as the nominal C/L.

3.3.2.4 Characterization of Corrosion Products on Carbon Steel and C22 Alloy

The chemical composition of steel corrosion product deposited on carbon steel and covering the ends of adjacent C22 Alloy segments was determined. Chemical analysis was performed by Energy Dispersive Spectroscopy (EDS) analysis. The procedure involved the collection of two corrosion product samples by scraping the scale on the carbon steel and by collecting a powder from the opposite interface concrete. A third sample was obtained from a tarnish-like scale observed mid-way along the C22 Alloy segment of some specimens. The chemical analysis results of the tarnish observed on C22 Alloy were compared against the results of the steel corrosion product samples taken from the surface of carbon steel. That comparison was intended to determine whether the tarnish scale was resulting from the C22 Alloy or a deposit of steel corrosion product transported sidewise along rebar. The C22 Alloy segments affected by slight tarnishing were examined using optical microscope for evidence of pitting before

and after chemical removal of tarnish scale according to ASTM G1-03 [ASTM G01-2003]. The affected C22 Alloy segments were subjected to gravimetric evaluation of mass loss based on the recorded initial weight. The determination of that undesirable mass loss is required to explore likely implications on applied current efficiency. More importantly, that evaluation is needed to examine possible influence of C22 Alloy slight corrosion on the degree of localization parameter being tested on estimating X_{crit}.

Secondary additional testing of possible oxygen evolution on the C22 Alloy was performed to confirm whether it is a factor to be considered in calculating the applied current efficiency. Duplicate cylindrical concrete specimens having ~ 51 mm diameter by ~101 mm height were used. The specimens were axially reinforced with ~ 14 mm diameter single bar of C22 Alloy and subjected to about 100 μA/cm^2 anodic current density. The material of the embedded bar was totally C22-Alloy and using the same concrete material as that in table 3.5 (batch I).

3.3.2.5 Reliability of Procedure for Gravimetric Determination of Mass Loss

Quantification of corrosion by the application of Faraday's law for the conversion of applied current to mass loss is associated with uncertainties. Low current efficiencies are usually related to issues such as consuming part of the applied current in oxygen evolution reaction [Nossoni et al. 2012]. Therefore, gravimetric evaluation of mass loss per ASTM G1-03 was employed in the present work for more reliable estimation of X_{crit}. The ASTM-recommended chemical removal of rust involves the use of a solution containing 1000 mL concentrated hydrochloric acid (HCl), 20 g antimony trioxide (Sb_2O_3) and 50 g

stannous chloride ($SnCl_2$). The cleaning solution (widely known as Clarke's solution) is used for rust removal in a cyclic fashion for a total cleaning time of 25-30 minutes at lab temperature. That procedure may be described as hydrochloric acid pickling process with acid inhibitors added to minimize acid attack to base metal while allowing removal of rust and mill scale [Fox et al. 1993]. Incorrect application of the ASTM procedure may result in over or under cleaning. Sources of error may arise from storage and excessive reuse of the Clarke's solution, insufficient mixing, extended cleaning durations or heating while cleaning. Nevertheless, compliance with the ASTM procedure when testing corrosion performance of deformed rebars with mill scale may not guarantee reliable quantification of mass loss. The mill scale is a layer of iron oxides formed during rebar hot rolling. The thickness of mill scale reported in literature found to be ranging from 2 – 70 µm [Ghods et al. 2011, Jaffer et al. 2009]. The mill scale on deformed rebars may possibly be removed when chemically cleaned in the as-received condition even without exposure to corrosion. That issue can lead to incorrect estimation of X_{crit}.

Based on the above discussion, an experimental investigation was performed to test the effect of the ASTM cleaning procedure on corrosion testing of deformed rebars. The test involved chemical cleaning of deformed rebars covered with mill scale (R4 and R5) in their as-received condition as well as smooth carbon steel bars (U8 and U9) according to the ASTM procedure. The deformed rebars and smooth bars had the same materials, dimensions, surface conditions as those for the specimens listed in table 3.4. The mass loss was

determined gravimetrically and the corrosion penetration calculated. The purpose was to examine the possible influence of the presence of mill scale on the values of X_{crit} evaluated by testing deformed rebars. Electrochemical impedance spectroscopy (EIS) was employed to estimate the rate of metal / rust removal during the process of chemical cleaning.

4. RESULTS AND DISCUSSION[2]

4.1 Pre-cracked Reinforced Concrete Pipe Specimens

4.1.1 Direct Observation and Qualitative Electrochemical Testing

Visual and open circuit potential (OCP) testing suggested that the specimens having nominal crack widths of 2.5 mm are more prone to corrosion damage than those having nominal crack widths of 0.5 mm. The case of relatively wide cracks is likely to be associated with neutralized solution within cracks due to efficient water mixing with bulk water. That neutralization can result in sufficiently low electrolyte pH for steel passivity breakdown leading to increased susceptibility to corrosion attack even at low chloride concentrations. One of the specimens having 2.5 mm nominal crack width (R12) exhibited a visible sign of rust within the crack after only two weeks of continuous chloride ponding. The other duplicate specimen of 2.5 mm nominal crack width (R4) showed a small rust spot at one steel-crack intersection after 52 days. Figure 4.1 shows the rust spot observed at one crack – steel intersection within the 2.5 mm wide crack of specimen R12. On the other hand, the cases of 0.5 mm nominal crack widths did not show any external sign of corrosion damage. The out-migrating corrosion product through pre-existing cracks seems to relieve build-up of stresses that would otherwise develop at steel-concrete interface. Therefore, durability prediction for cases of preexisting wide cracks may best be evaluated

[2] Contents include previously published materials in [Busba et al. 2013a and b]. Permissions are provided in appendix C.

based on time to critical loss in steel cross-section. Conversely, accumulation of rust and corresponding pressure build-up at steel – concrete interface in the case of narrow cracks is expected to result in further cover cracking. Corrosion-induced further cracking of concrete cover having a narrow crack would be even more pronounced when the cracks become self-healed [Neville 2002]. Self-healing of about 0.5 mm wide cracks was previously reported to be capable of partially recovering mechanical and electrochemical properties [Ramm et al. 1998]. The current study is only focused on the corrosion-induced cracking damage mode applicable to uncracked concrete or to concrete containing narrow preexisting cracks.

Figure 4.1 Rust observed at an intersection of steel with 2.5 mm-wide crack after continuously ponding in chloride for two weeks in specimen R12. (Indicated by arrow)

Open circuit potentials (OCP) provided a supplemental qualitative indication of corrosion level. Locations of most negative potentials of steel in reinforced concrete under atmospheric exposure conditions are indicative of active corrosion. Conversely, least negative potentials are indicative of either passive or

low corrosion activity. General guidelines on potential ranges for evaluating risk of corrosion are detailed in ASTM C-876 [ASTM C876-2009]. Figure 4.2 shows the OCP values for the pre-cracked and control duplicate RC pipe specimens averaged over each exposure environment. The specimens having 2.5 mm wide cracks exhibited the most negative potential over the three test conditions. Those highly negative potentials indicate high risk of corrosion activity in the case of wide cracks even in the absence of chloride during exposure to DI water. In contrast, the control specimens exhibited much less negative potentials comparable to values expected for passive steel in concrete.

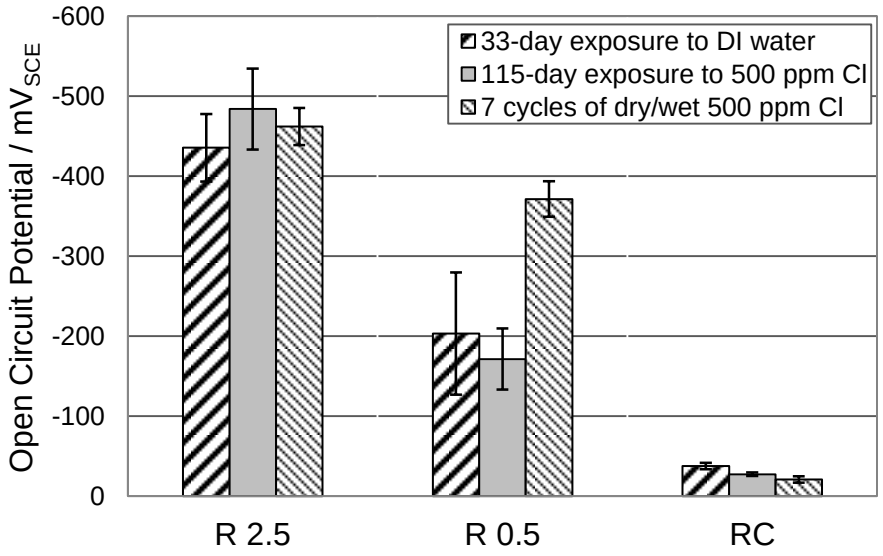

Figure 4.2 Open circuit potentials for duplicate specimens averaged over each exposure environment for the pre-cracked and control specimens.

On the other hand, the OCP values for the specimens having 0.5 mm wide cracks were distinctly at intermediate levels between those for the 2.5 mm-wide crack and control specimens. Those levels of OCP indicate some extent of

corrosion activity with their slightly mitigated values possibly signifying smaller corrosion-affected zones.

Potential mapping provided evidence that corrosion is localized at preexisting crack – steel intersections as manifested by the most negative potentials observed at those intersections. Figure 4.3 shows the potential maps recorded during the dry period of the fifth dry / wet exposure cycle for specimens having 2.5 mm (R12) and 0.5 mm (R3) wide cracks. All potentials in the footprint area of specimen R12 were more negative than -300 mV_{SCE} at cyclic exposure to chloride indicating large areas affected by corrosion (figure 4.3 a). In specimen R3, only potentials at some crack-wire intersections were more negative than -300 mV_{SCE} at cyclic exposure indicating highly localized corrosion (figure 4.3 b).

4.1.2 Destructive Examination

Detailed direct inspection showed that all crack wire intersections were influenced by corrosion within the test footprint area. Corrosion was found to be uniformly distributed around the perimeter of steel reinforcement in both cases of 0.5 mm and 2.5 mm nominal crack widths. Figure 4.4 shows the extent and distribution of corrosion damage for one of the preexisting crack-wire intersections shown in figure 4.3 (a) in specimen R12. Measurements of extent of corrosion on each side of the crack were performed to determine the size of corrosion influence zone. The average lengths of corrosion zones were found to be in the order of 10 and 5 mm for the cases having nominal crack widths of 2.5 and 0.5 mm, respectively.

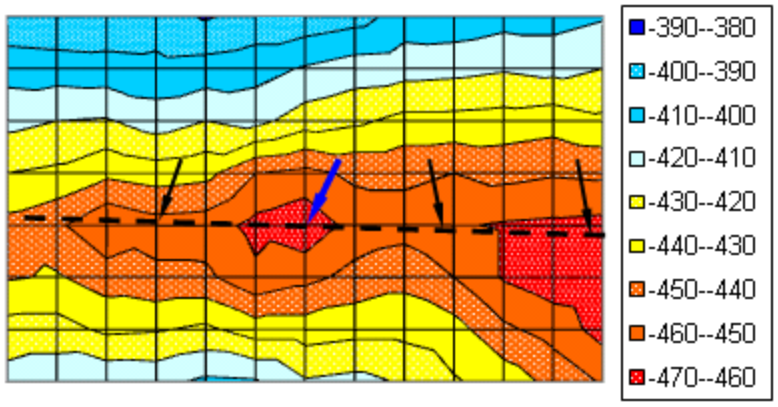

(a)

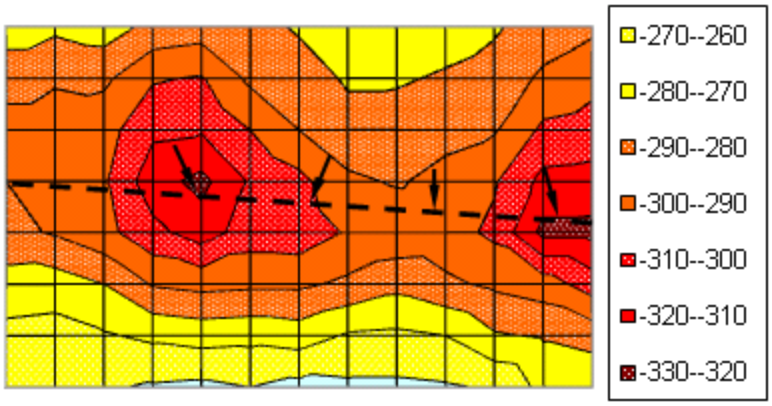

(b)

Figure 4.3 Potential mapping performed at the dry period of the fifth cyclic exposure for pre-cracked specimens having nominal crack widths: (a) 2.5 mm (R12) and (b) 0.5 mm (R3). All potentials are in mV_{SCE}. Broken line and arrows indicate approximate pre-existing crack positions and intersections with steel, respectively.

The depth of corrosion penetration (radius loss in steel wire) was found to be largest at the intersection point and gradually decreasing away from the intersection on each side of the preexisting crack. Actual values of radius loss over the corrosion-affected zones were approximately measured for all specimens and transformed into mass loss. Those results are listed in table 4.1 and will be shown later to be useful in calibrating the EIS-estimated corrosion currents. Considering the concrete cover values shown in figure 3.2, the

corrosion localization may be expressed in terms of the ratio of concrete cover to length corrosion zone (C/L). The values of C/L were found to be ranging from about 1 to 5 when taking into account the standard deviations in concrete cover thickness.

Figure 4.4 Observed corrosion influence zone and morphology at the intersection of preexisting crack with steel after demolishing at end of experiment. For the intersection indicated by the blue arrow in figure 4.3 (a)

4.1.3 Electrochemical Impedance Spectroscopy

Information on evolution of corrosion currents versus time were obtained by various EIS testing of specimens conducted over the three exposure regimes. Since the EIS tests were performed before autopsy, the actual corroding surface areas were not know at the time of measurements. Therefore, the impedance responses shown next represent the integrated values over the total surface area of embedded steel (~400 cm^2). Most of that area was in the passive state whereas the steel in intersection regions underwent active corrosion. No attempts were made at this stage to present surface area-normalized impedance values due to changes in area of influence zone from specimen to another and with time. Estimates of corrosion rates based on the final size of corrosion zones

revealed by autopsy are presented later here. Figure 4.5 shows an example of the impedance spectra for the pre-cracked specimens having nominal crack widths of: (a) 0.5 mm and (b) 2.5 mm. The EIS data shown are testing after 95 days of continuous chloride ponding following the initial DI water exposure. The impedance response in figure 4.5 (a) for specimen R6 is characterized by a straight line reflecting very high polarization resistance and zero corrosion current. The inclined straight line response is a characteristic trend of the CPE element [Sagüés et al. 1992]. The response for specimen R3 is very slightly showing some curvature indicating that the polarization resistance has a finite value but still high which results a negligible amount of current. In contrast, the impedance spectra in figure 4.5 (b) indicates significantly less values of polarization resistance which correspond to much higher corrosion currents. It is worth noting that conclusions on corrosion trends were drawn based on considering results from multiple EIS tests and not only on those exemplified in figure 4.5. Figure 4.6 shows an example of the equivalent circuit fitting for the EIS spectrum of specimen R4 in figure 4.5 (b). It is shown that the low frequency part of the EIS response may reasonably be fitted in accordance with the analogue equivalent circuit in figure 3.8 and extrapolating the fit to determine the value of Rp. The high frequency end of the response was excluded from fitting due to uncertainties arising from fitting complications when considering that part of the spectrum in some EIS spectra. Those uncertainties may be attributed to changes in the high frequency portion due to uneven distribution of EIS excitation current

caused by the high resistivity and corrosion localization [Sagüés et al. 1992 and Kranc et al 1996].

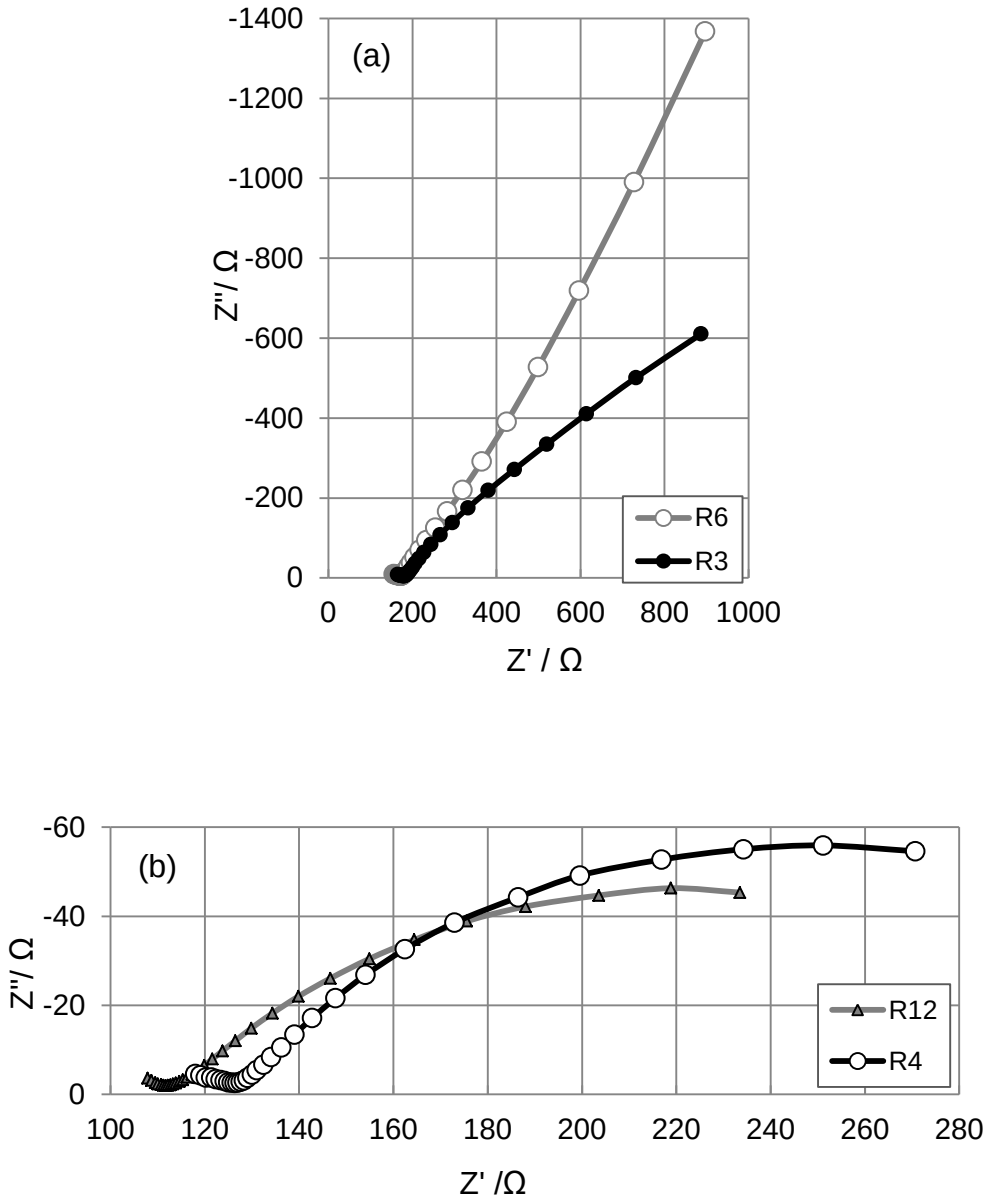

Figure 4.5 EIS integrated response over the entire embedded steel surface (400 mm^2) for pre-cracked specimens having nominal crack widths: (a) 0.5 mm and (b) 2.5 mm after 95 days of continuous chloride ponding. Frequency range 1 mHz to 1000 Hz, 5 points / decade.

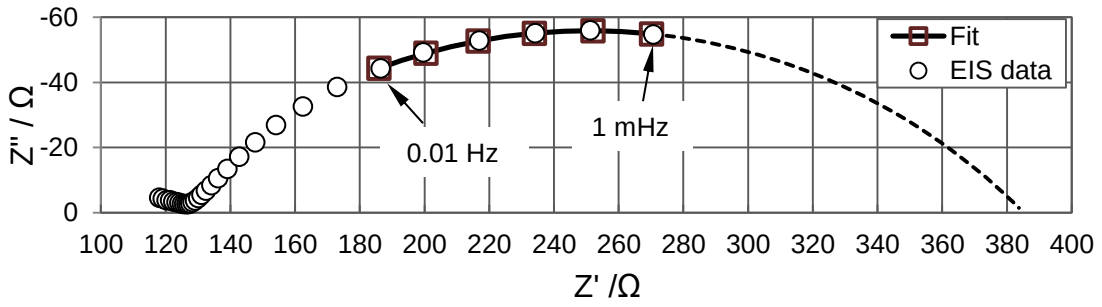

Figure 4.6 Fitting of EIS spectrum of specimen R4 in figure 4.5 (b) using the equivalent circuit fit for the data over the frequency range indicated. The fitting line was extended by a broken line to hit the limit of zero frequency. Impedance values are not normalized to surface area.

It is apparent from the EIS spectrum in figure 4.6 that the phase angle at the high frequency portion goes to zero and deviates from zero as the frequency increases. That end of the spectrum was not considered in the analysis either, because it corresponds to the dielectric properties of the electrolyte medium. Consequently the evaluation of Rp was made based on the selected frequency range indicated earlier. The possible influence of limiting the analysis to the selected range on results of Rp was examined and found to be insignificant. A comparison was made between two analyses of the EIS data of specimen R4 considering two frequency ranges from 1 mHz to 10 Hz (figure 4.6) and 1 mHz to 1000 Hz. The equivalent circuit fitting parameters Rs (Ω), Rp (Ω), Y_o ($sec^n/Ω$) and n were found to be 117, 268, 0.037 and 0.501, respectively for the limited frequency range. Those parameters were found to be 123, 271, 0.042 and 0.509, respectively for the extended frequency range. The change in polarization resistance (Rp) was in the order of 2%.

The solution resistance (Rs) values were estimated from the Nyquist diagram by noting the real impedance value corresponding to the lowest phase angle at the high frequency end of the EIS spectrum. Figure 4.7 shows the Rs values for the pre-cracked and control duplicate specimens averaged over each test environment. The values of Rs increased as the crack width decreased and were highest for the uncracked specimens over all test conditions. The presence of 2.5 mm and 0.5 mm wide cracks resulted in reduction in solution resistance by factors of 2 and 1.5, respectively. The EIS technique was proven to be a promising tool for detecting cracks in reinforced concrete.

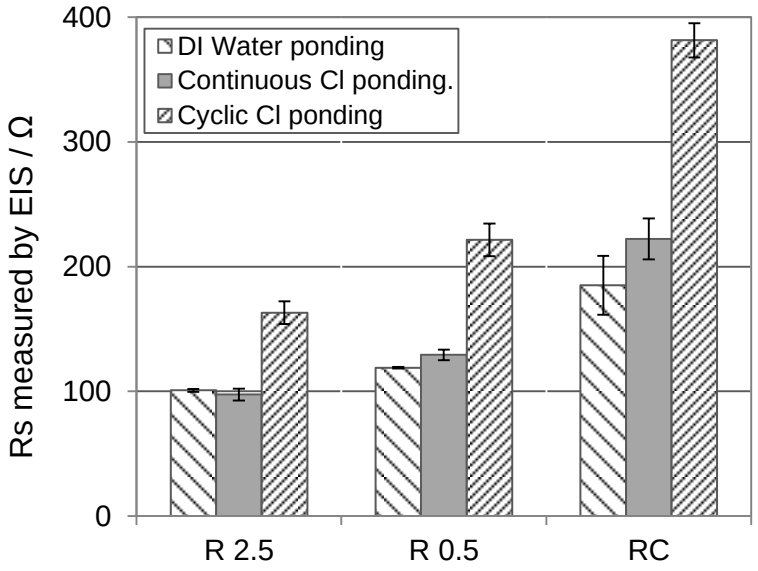

Figure 4.7 Solution resistance (Rs) values obtained from EIS and averaged over each exposure regime for duplicate pre-cracked and control specimens

Figures 4.8 and 4.9 show the parameter values Yo and n of the CPE as determined by EIS data fitting to the equivalent circuit, respectively. The fittings performed for the EIS spectra over the selected frequency range 1 to 10 mHz. The diagrams in figures 4.8 and 4.9 show values for duplicate pre-cracked and

control specimens averaged over each exposure period. The values of Y_o showed an increasing trend with the increase in crack width.

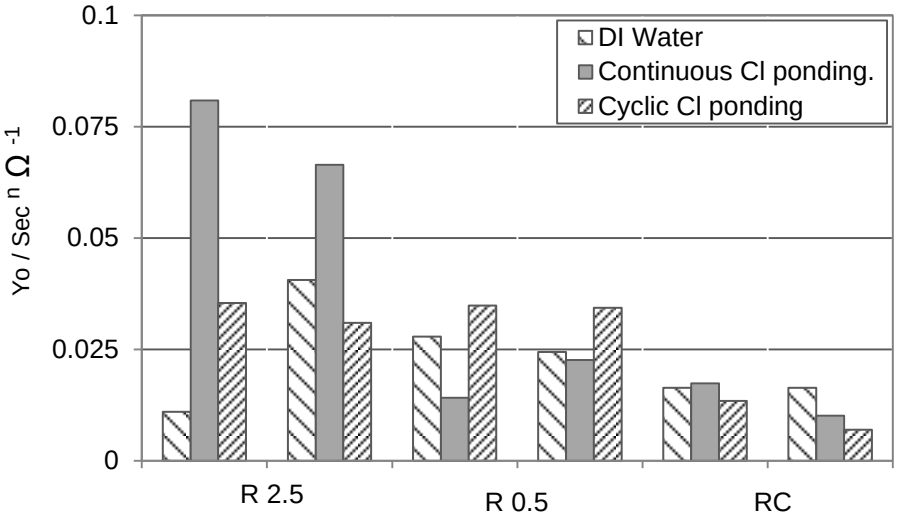

Figure 4.8 The CPE parameter Y_o derived from fitting over the frequency range 0.001 to 0.01 Hz. The values of Y_o averaged over each exposure regime for duplicate pre-cracked and control specimens.

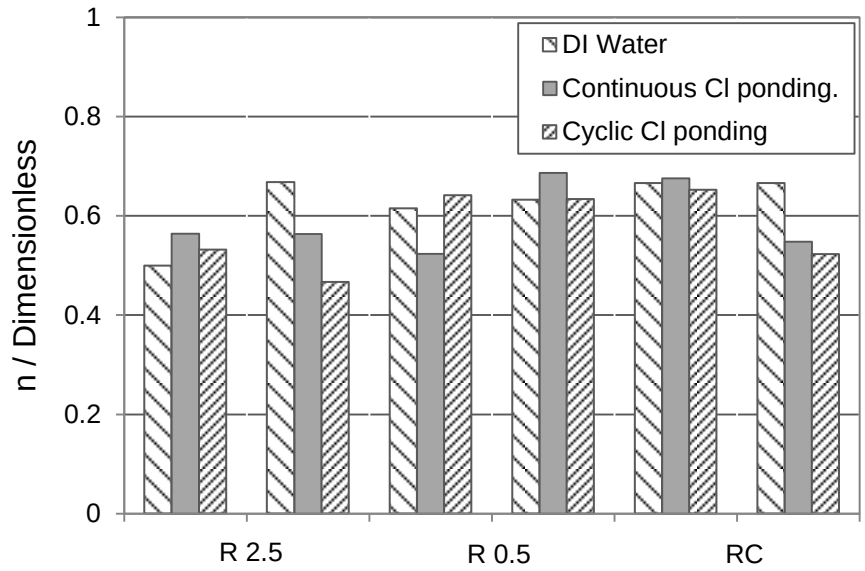

Figure 4.9 The CPE parameter n derived from fitting over the frequency range 0.001 to 0.01 Hz. The values of n averaged over each exposure regime for duplicate pre-cracked and control specimens.

The exponent n was mostly falling between 0.5 and 0.7 which is characteristic of common EIS response of steel in concrete [Sagüés et al. 1992]. It is emphasized that the values of Rp obtained from multiple EIS testing were presented in the form of instantaneous corrosion currents and mass losses as will be shown next.

4.1.4 Evaluation of EIS Results and Estimation of Corrosion Rates

The apparent instantaneous corrosion current (I_{app}) corresponding to each EIS measurement was calculated from equation 3.2. The instantaneous mass loss was calculated from equation 3.3 but replacing the term (I) with (I_{app}). The instantaneous mass loss was calculated over each exposure environmental condition and plotted as a cumulative mass loss versus time for each specimen in figure 4.10. The total mass losses directly estimated earlier based on destructive examinations were also plotted on figure 4.10 for comparison purposes. Comparison of mass loss values from both methods suggested that the EIS-based method underestimated the corrosion currents. That observation may be attributed to the nature of EIS response associated with localized corrosion [Sagüés et al. 1992].

Table 4.1 lists the total mass losses determined based on both EIS and direct measurements. In order to gain improved information on the corrosion current evolution over various exposure times, The EIS-estimated currents had to be calibrated based on direct observations. A calibraion factor (Fc) had to be derived (equation 4.1) and applied to obtain the actual corrosion currents (Icorr). The derived calibration factors listed in table 4.1 were comparable to similar

values previously reported for the correction of underestimated corrosion currents based on EIS performed on cases of localized corrosion [Sagüés et al 1993].

$$Fc = \frac{I_{corr}}{I_{app}} = \frac{\text{Actual Mass Loss}}{\text{EIS-based Mass Loss}} \quad (4.1)$$

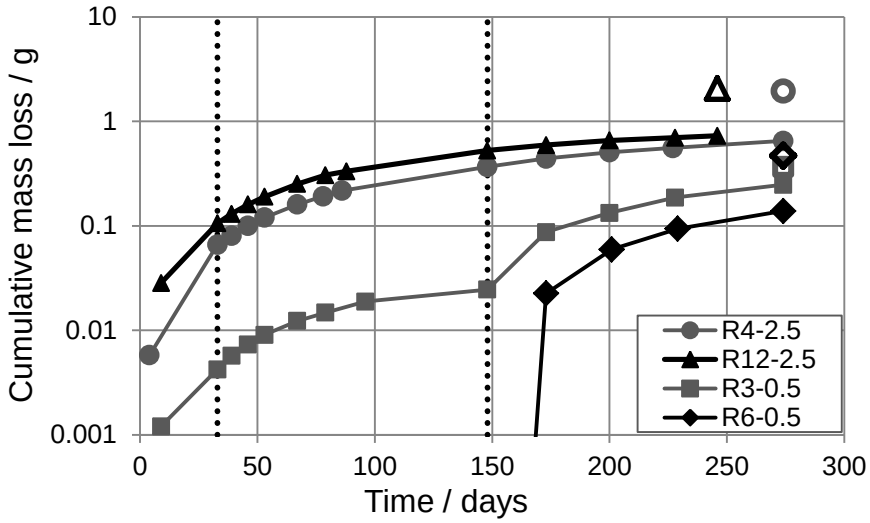

Figure 4.10 Apparent EIS-based mass loss values for various EIS measurements for the pre-cracked and control specimens versus time. Mass losses based on direct measurements of the total loss of steel wire diameter performed after autopsies are shown by hollow symbols. The dotted vertical lines mark three exposure regimes (left to right: DI water, continuous and cyclic chloride ponding)

Table 4.1 The apparent EIS-based mass losses and actual measured values

Sp. No. / Crack width in mm	Time / Days	Total Mass Loss /g		Fc= Icorr/Iapp	Anode / Cathode area ratio	Fc range From [Sagüés et al 1993]	
		Actual	Apparent from EIS			From	To
R4-1.70	274	1.95	0.65	3	0.04	1.7	3.5
R12-2.69	246	2.07	0.73	2.84	0.03	1.74	3.64
R3-0.71	274	0.47	0.25	1.88	0.01	2.35	5
R6-0.45	274	0.37	0.14	2.64	0.01	2.35	5

In order to calibrate the corrosion currents, the EIS-estimated instantaneous currents were multiplyed by a generic calibration factor (Fc) of 3. The calibration factor was assumed to be constant with time and applicable to each individual exposure condition. The corrected values were averaged over each exposure period for each duplicate specimens and plotted on figure 4.11.

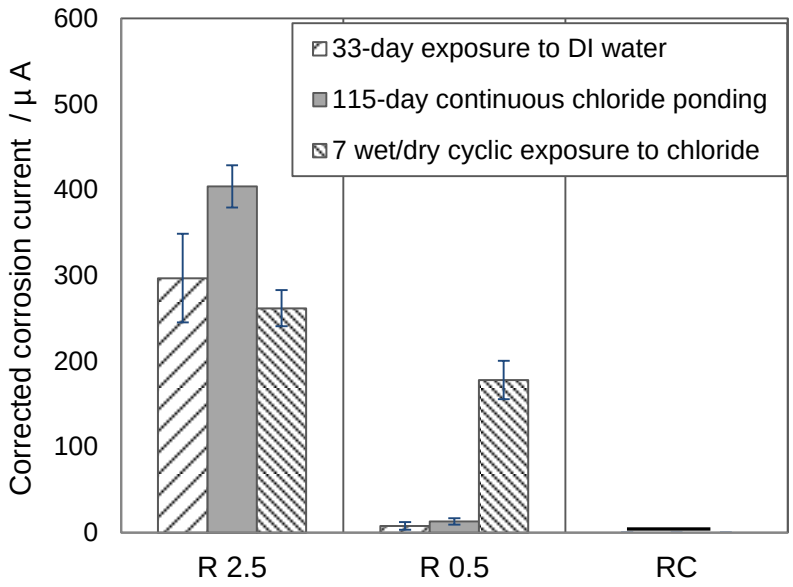

Figure 4.11 Corrosion currents corrected using calibration factors (Fc) for various EIS-measured values averaged over each exposure period for duplicate pre-cracked and control specimens. Values are not surface-area-normalized according to the observed influence zones.

From figure 4.11, the evolution of corrosion over time may be appreciated during each exposure regime. The trends suggested seem to be synonymous to those abstracted from the OCP results and visual signs of rust. There is a clear indication of increased corrosion severity when exposed to chloride-containing environment in the case of 2.5 mm nominal crack widths. On the other hand, the corrosion severity significantly increased (by an order of magnitude) only during

the cyclic exposure of the chloride-containing environment in the case of 0.5 mm nominal crack width. In contrast, no measurable corrosion current was observed in the case of uncracked specimens.

The corrosion rates in (µm/Y) were obtained by Faradaic conversion of total mass losses and using the observed corrosion influence zones. Figure 4.12 show the corrosion rates averaged for each pair of duplicate specimens over the entire exposure period. The corrosion rates may be dominated by the high values during the aggravated intermittent exposure. As indicated earlier, such relatively high values may not be typical of those encountered in service. Those high values may represent an upper bound likely to be reached due to macrocell current effect, characteristic of RC structures having thin concrete cover and / or low quality concrete (see chapter 5).

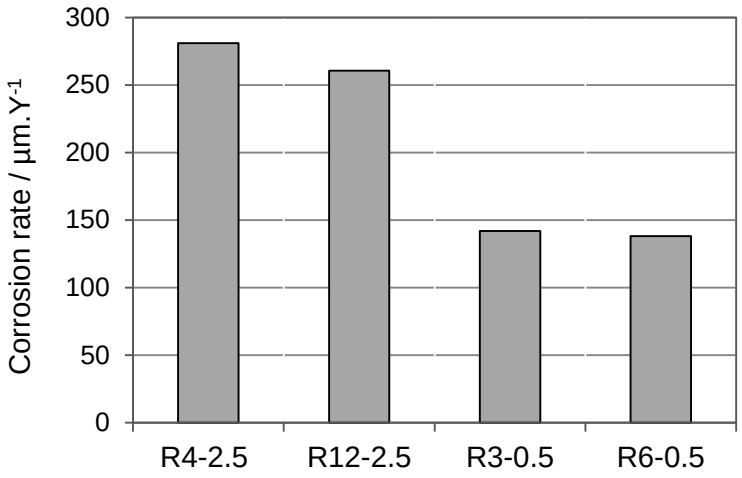

Figure 4.12 Corrosion rates calculated based on direct mass loss measurements, normalized to the observed influence zone surface area. Values represent average corrosion rates over the entire duration of the three exposure regimes for each specimen

4.2 Corrosion-induced Cracking Test

4.2.1 Detection of Surface Cracking and Morphology of Rebar Corrosion

Monitoring of galvanostatic current and driving voltage evolution with time served as an early indicator for appearance of corrosion-induced surface cracking. Figure 4.13 shows an evident rapid increase in driving voltage immediately before onset of concrete surface cracking for a specimen having a ratio of nominal C/L=3. The voltage increase may be attributed to the possible increase in concrete resistance due to emerging micro-cracks at rebar-concrete interface regions but before reaching the external surface. A gradual voltage increase was observed as time progressed likely due to increased resistance around rebar resulting from the dry-out of concrete. That phenomenon may be attributed to the application of electric field and known as the electro-osmotic effect [Marshall et al. 2007]. The cases that took longer to crack were associated with relatively higher driving voltages at cracking, presumably due to the time-dependent nature of the dry-out process. The galvanostatic current appeared to be fairly stable.

As anticipated, the cases of less localized corrosion (lower ratios of nominal C/L) exhibited ~ 0.1 mm wide surface cracks before those with more localized corrosion (higher ratios of nominal C/L) as depicted in table 4.4. Figure 4.14 illustrates corrosion-induced cracking orientations for the cases of uniform and localized corrosion. In the case of uniform corrosion (nominal C/L=0.2), the observed crack was a single longitudinal one parallel to the embedded rebar. On the other hand, cracking in the cases of nominal C/L=1, 2 and 3 was oriented in a

transverse direction to the embedded rebar around one half of the circumference of a cylinder and over the corroding spot. The half-circumferential cracks in the cases of nominal ratios of C/L=1 and 2 were bounded by short longitudinal cracks having lengths similar to those of the corroding steel spot. The commonly encountered concrete cover failure modes due to uniform corrosion of embedded rebars have the form of longitudinal cracking, delamination or spalling. Those cracking modes were reported in the literature to be dependent upon the ratio of C/Ø and the ratio of rebar spacing to rebar diameter [Zhou et al. 2005]. However, the observed transverse cracking mode corresponding to localized corrosion suggested that the ratio of C/L can be an additional significant contributor to defining the governing corrosion-induced failure mode in RC members. The determination of limiting criteria to define the type of governing cracking mode is beyond the scope of this dissertation.

Upon cover cracking, the concrete cylinders were autopsied to retrieve the embedded rebars for examination. Figure 4.15 (a) shows an entirely corroded smooth bar along its length for the uniform corrosion cases that exhibited longitudinal concrete cover cracks (nominal C/L=0.2). Figure 4.15 (b) confirms that corrosion was limited to the central anodic regions for the localized corrosion cases that exhibited circumferential concrete cover cracking (nominal C/L=1, 2 and 3). The areas affected by corrosion were initially defined based on observation of steel corrosion product distribution and subsequently confirmed upon removal of rust. The cases having nominal C/L=1 and 2 exhibited partially corroded surface areas of anodic segments, whereas those having nominal

C/L=3 exhibited entirely corroded surfaces. Table 4.2 shows the percentage of anodic surface areas affected by corrosion for the cases of uniform and localized corrosion. The partially corroded regions, while limited to part of the steel perimeter, were approximately extending along the entire length of anodic segments.

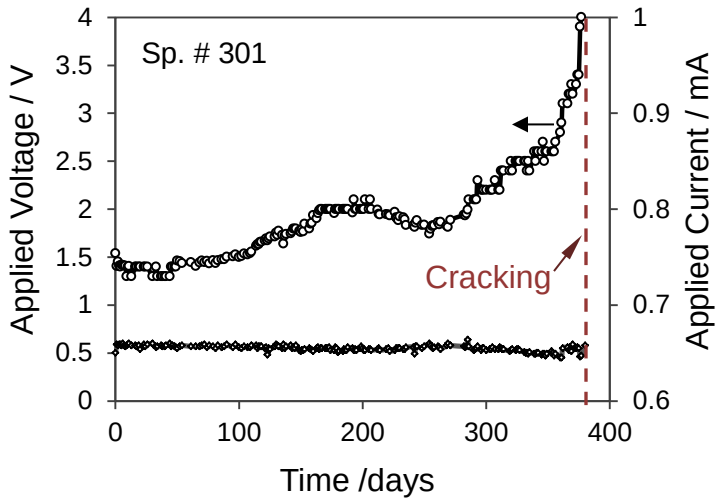

Figure 4.13 Accelerated corrosion under galvanostatic control indicating constant current and gradual increase in voltage immediately before cracking. (For a specimen having a C/L ratio of 3).

Figure 4.14 Illustration of observed orientations of induced cracking. (a) longitudinal and (b) circumferential, both across cylinder half, as a result of uniform and localized corrosion morphology along embedded rebar, respectively.

The cases having nominal C/L= 4 and 5 did not exhibit any corrosion-induced surface cracking even after two years of exposure to accelerated corrosion. Part of the reason for that is likely to be related to the anode size effect resulting in possible increase in chloride threshold as the anode size decreases [Angst et al. 2011b, Li et al. 2004 and Melchers et al. 2009]. The time-dependent transport of chloride ions towards rebar proceeds by migration under the applied electric field. Times to corrosion initiation would therefore vary depending on the level of respective chloride threshold to be exceeded.

Generally, the smooth surface finish is expected to elevate the chloride corrosion threshold by about an order of magnitude compared to the nominal value of 0.4 % by weight of cement [Ghods et al. 2011]. Further, the actual level of chloride in concrete may be reduced as a result of admixing the chloride salt to concrete. It was reported in the literature that some of the admixed chloride become physically entrapped in C-S-H gel during cement hydration in addition to chemical binding expected in the case of penetrating chloride [Enevoldsen et al. 1994]. The aforementioned factors can further prolong time to chloride-induced depassivation. The heterogeneous nature of concrete is likely to cause a non-uniform chloride migration towards rebar which in turn would lead to activation of some anode regions before others. The latter may explain the partially corroded anode regions in the cases of nominal C/L=0.2, 1 and 2. Conversely, in the case of nominal C/L=3, the longer time expected for cracking may allow for chloride ions to reach the threshold level at the entire anode regions under the electric field. The deformed as-received rebars were reported to require from 5 to 14

days for its passive layer to form and stabilize as opposed to smooth bars for which the protective layer forms more rapidly [Ghods et al. 2009]. The reduced ability of passive film to stabilize on deformed bars in the presence of admixed chloride may further support the choice of smooth bars for this investigation.

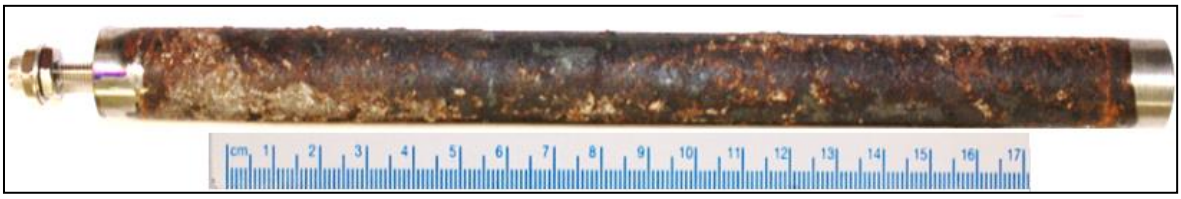

(a)

(b)

Figure 4.15 Corrosion morphologies (a) uniform and (b) localized (C/L=1) along the embedded rebars extracted upon concrete surface cracking. (For specimens U3 and 103, respectively).

In localized corrosion cases, there was a visual evidence of side-wise transport of steel corrosion product along rebar to cover the adjacent ends of the outer C22 segments. The extent of side-wise transport of rust on each side of the carbon steel anodic segment (figure 4.16 a) increased as the degree of corrosion localization increased. Figure 4.16 (b) shows that effect being also evident in the concrete interface surrounding the embedded bar in addition to rust filling the

steel-concrete interfacial zone (ITZ). Figure 4.17 shows the average lengths of lateral rust propagation for the localized corrosion cases.

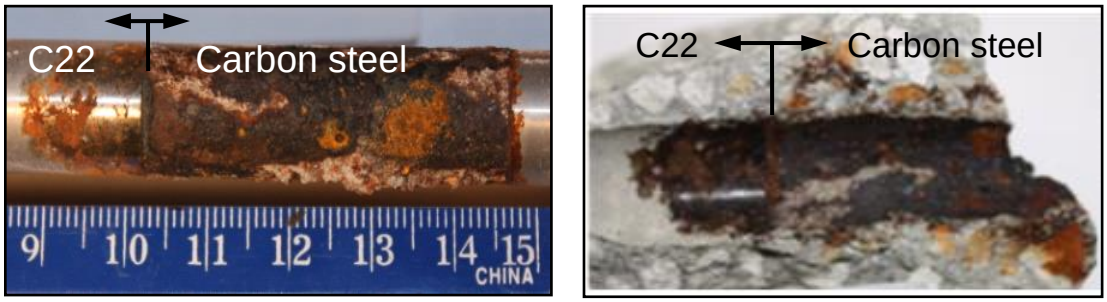

(a) (b)

Figure 4.16 Lateral distribution of steel corrosion product toward the adjacent C22 alloy segments (passive regions) and rust filling of ITZ shown on (a) rebar and (b) concrete interface, respectively. (For specimen 101 with a ratio of C/L=1).

Figure 4.16 (b) shows also some steel corrosion product diffused into the surrounding concrete. The diffused steel corrosion products into concrete surrounding were more evident in the case of uniform corrosion of smooth bar (figure 4.18 a) and deformed bar (figure 4.18 b). Chemical cleaning of steel segments (figure 4.19) revealed that some steel segments exhibited corrosion pits. The pit depths were about four times the average corrosion penetration which is typical of pitting behavior observed under natural exposure conditions [Gonzalez et al. 1995]. However, the calculated penetration depths referred to in the following sections were values obtained by averaging over the corroded region. Figure 4.20 shows the procedure used to determine the average mass of rust removed by cyclic chemical cleaning in accordance with ASTM G01 and to account for any loss of base metal during the cleaning process.

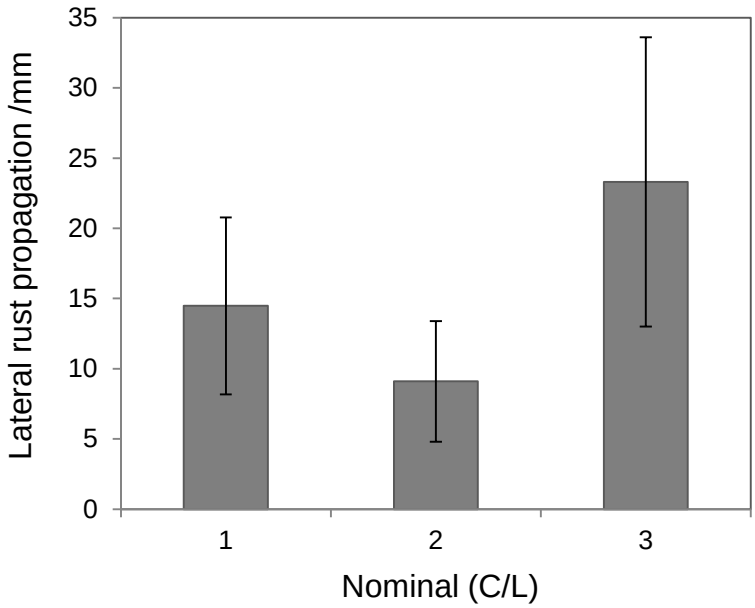

Figure 4.17 Extents of lateral rust propagation measured from each edge of a corroding segment along the rebar at four clock positions around rebar perimeter.

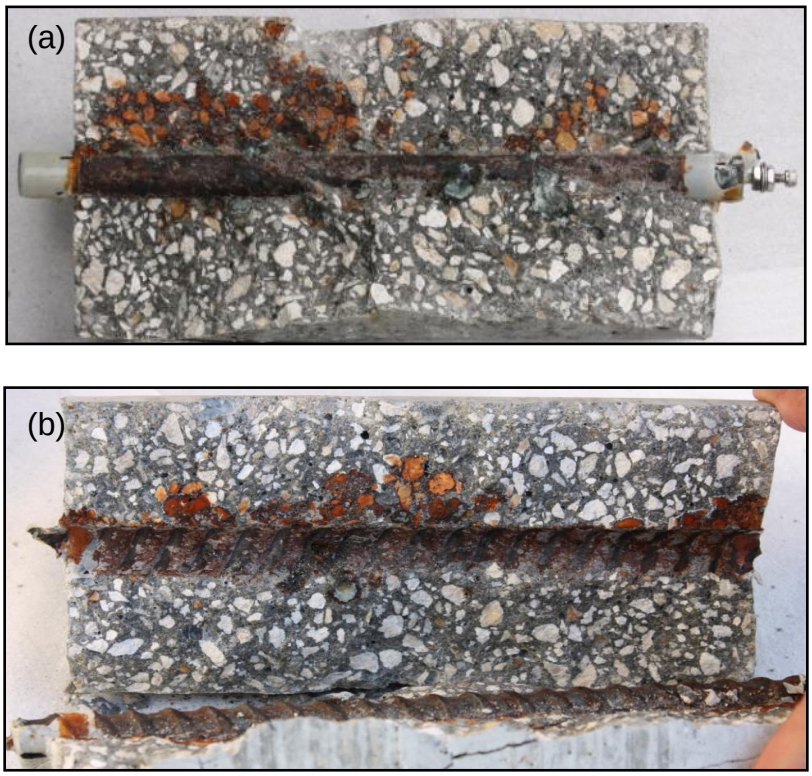

Figure 4.18 Amounts of steel corrosion product transporting into induced longitudinal cracks in cases of uniformly corroding (a) smooth and (b) deformed (ribbed) steel rebars. (For specimens U4 and R3, respectively)

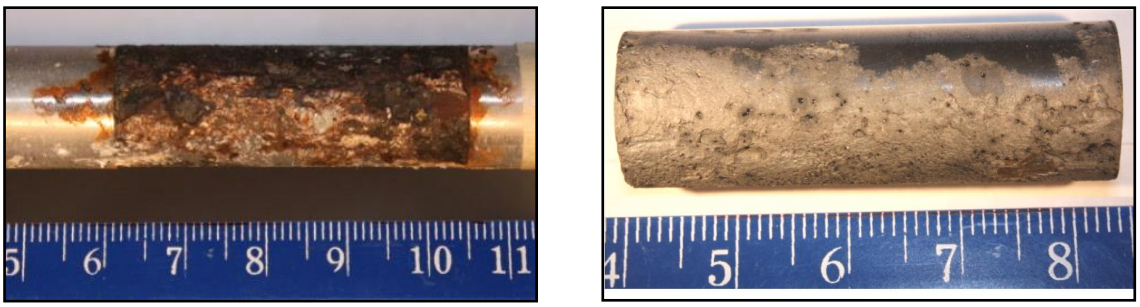

Figure 4.19 Carbon steel segment of the localized rebar corrosion case of C/L=1 for specimen 103 before and after chemical removal of rust. The cleaned specimen revealed partially corroded surface area (for random clock positions)

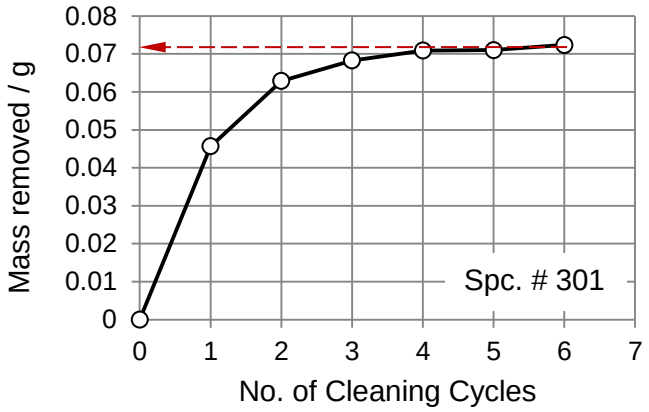

Figure 4.20 An example showing the procedure used to determine the mass of rust removed by cyclic chemical cleaning in Clarke's solution as per ASTM G1-03

4.2.2 Accelerated Corrosion Efficiency

Figure 4.21 shows a correlation for the measured values of mass loss listed in table 4.2 with the Faradaic values calculated based on equation 3.3. The current efficiency, which provides a measure of how much of the impressed current is converted into mass loss, was calculated using equation 3.4 and plotted in figure 4.22 for the various cases. On the one hand, a reasonable agreement was observed between the gravimetric and Faradaic values of mass loss for the case of nominal C/L=0.2 for both the smooth and deformed bars. On

the other hand, the correlation in the case of localized corrosion (nominal C/L=1, 2 and 3) suggested that the Faradaic calculations overestimated the actual values of mass loss. The reduced current efficiencies may be attributed to the oxygen evolution reaction on the steel surface before the chloride threshold level needed for depassivation is reached. The oxygen evolution can also be taking place alongside the iron dissolution reaction at highly positive rebar IR-free potentials which were found to be ranging from +600 to +900 mV_{SCE}. Oxygen evolution (equation 4.2) serves as the electrochemical reaction responsible for the exchange of charge at rebar surface. The occurrence of that reaction may also be possible on the surface of the C22 segments as will be shown later. The decrease in anodic segments in test specimens is associated with an increase in the surface area of the C22 alloy segments. Therefore, the applied current tends to scatter to satisfy the demand by the adjacent C22 segments for O_2 evolution. That unexpected scatter may become more pronounced as the applied anodic current, which was calculated based only on the carbon steel surface area, decreases (table 4.2). The aforementioned analysis may explain the decrease in current efficiency as the length of anodic carbon steel segment decreases (Figure 4.22). The need to exceed the increasing chloride threshold as anode size decreases was shown by Nossoni et al. to reduce the current efficiency at low chloride levels [Nossoni et al. 2012].

$$2H_2O \longrightarrow 4H^+ + 4e^- + O_2 \qquad (4.2)$$

Other general factors responsible for the discrepancy between the Faradaic-estimated and gravimetric values of mass loss may include:

(a) Inaccurate current integration throughout the test duration due to insufficient measuring points resulting in errors in quantifying the Faradaic charge.

(b) Over or under-estimation of gravimetric mass loss due to over- or under-cleaning, respectively. Over-cleaning may result from excessive removal of base metal due to prolonged exposure to chemical cleaning solution or lack of acid inhibitors. Heating during cleaning, or storage of volatile inhibitor-containing solution for reuse, may result in the malfunctioning of inhibitors due to disintegration or evaporation, respectively [Fox et al. 1993]. Over-estimation of mass loss can also be due to failure to adjust for removed base metal following the procedure indicated by red arrows in figures 4.20 and 4.27. It can also be simply due to the chemical removal of pre-existing mill scale on rebar surface which is made up of oxides not caused by the corrosion process. Further, it was reported in the literature that the increase in the amount of alloying elements such as Cu, Cr, Mn and Si reduces the attack of base steel by the acid cleaning solution. Conversely, the increase in the phosphorous content in steel was shown to accelerate the corrosion of base steel [Singh et al. 2003].

(c) Steel specimen subjected to impressed current may experience self-corrosion not caused by the externally applied current which results in values of gravimetric mass loss larger than the Faradaic-estimated ones [Alonso et al. 1998].

(d) The higher the chloride content and the lower the applied current; the higher the current efficiency is expected to be [Nossoni et al. 2012].

The calculated accelerated current efficiencies may have also decreased due to the likely dry-out of concrete caused by the flow of current [Torres-Acosta 2010]. That effect may further substantiate the decreasing trend in current efficiency as the anodic segment decreases as those cases are subjected to current flow for longer durations before cracking.

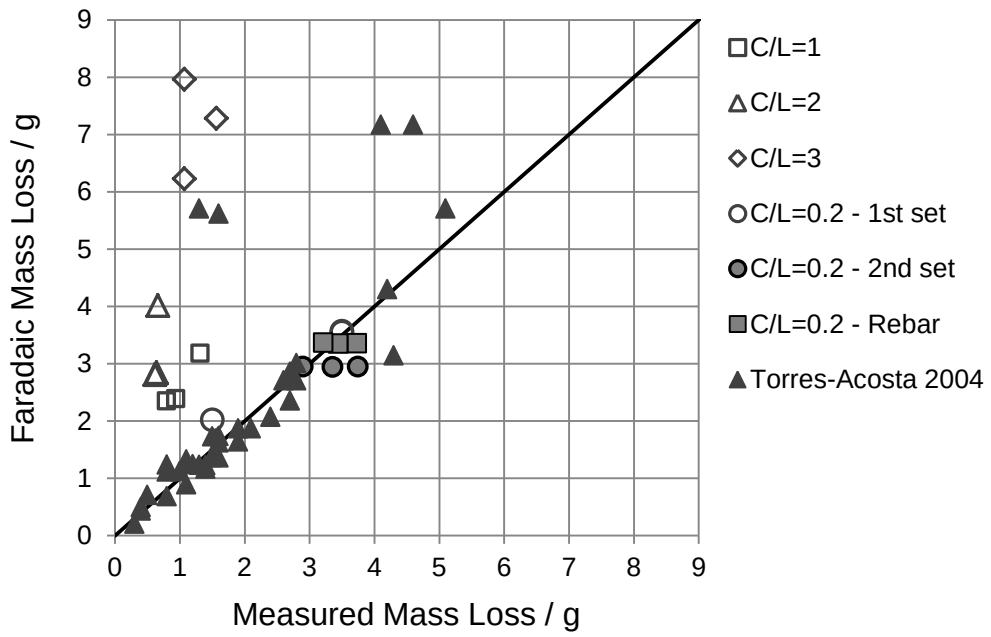

Figure 4.21 Amounts of steel mass loss determined by gravimetric measurements and Faradaic conversion of applied currents

The possible uncommon ion valence from the dissolution of Fe to Fe^{3+} or the dissolution of alloying elements may be another source of erroneous Faradaic estimation of mass loss [Nossoni et al. 2012]. Figure 4.23 shows evidence of tarnish-like yellowish layer only observed in specimen 303. The

observation of only one affected segment of C22 alloy was found to be caused by an improper contact of the counter electrode (CE) facing the unaffected C22 segment. The latter caused the current to flow only through one CE. The tarnish was evidently different in color from the dark brown steel rust directly on the carbon steel segments or extending to the ends of C22 segments.

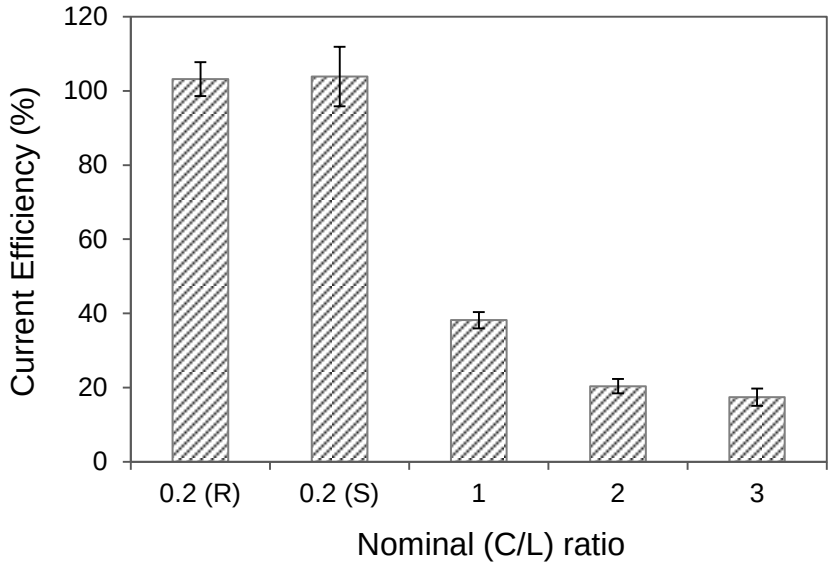

Figure 4.22 Decrease in corrosion current efficiency as anodic area decreases

Figure 4.23 Entirely corroded surface of carbon steel segment covered by dark brown rust and slight tarnish-like yellow deposit over one of the C22 segments. (Indicated by arrows no. 1 and 2, respectively for a specimen having a ratio of C/L=3).

Table 4.2 Gravimetric mass loss data and observed corrosion distribution

Sp. #	Nominal (C/L)	L / cm	Applied Current /mA	Δm_G / g	% Area Corroded
U1	0.21	20.32	9	3.5	100
U2		20.32		1.5	88
U3		20.32		3.5	100
U4		20.32		2.89	98
U5		20.32		3.74	91
U7		20.32		3.35	97
R1		20.32		3.73	100
R2		20.32		3.44	100
R3		20.32		3.21	100
101	1	4.37	1.951	0.8	51
102		4.37		1.32	64
103		4.36		0.94	61
201	2	2.16	0.967	0.66	92
202		2.16		0.62	81
203		2.17		0.64	58
301	3	1.48	0.656	1.07	100
302		1.46		1.57	100
303		1.48		1.07	100
401	4 (Uncracked)	1.07	0.478	Unbroken	
402		1.06		0.45	100
403		1.05		Unbroken	
501	5 (Uncracked)	0.86	0.384	0.67	100
502		0.86		Unbroken	
503		0.86		Unbroken	

The observed slight corrosion on C22 alloy may be attributed to surface acidification caused by O_2 evolution (equation 4.2). That observation is believed to have contributed to the reduced current efficiency calculated for that case. Figure 4.24(a) shows an EDS analysis indicating the presence of Cu in a steel corrosion product sample extracted from the surface of carbon steel. Figure

4.24(b) shows also an EDS analysis result of a tarnish sample obtained from the C22 alloy surface indicating the presence of dissolved C22 alloy elements.

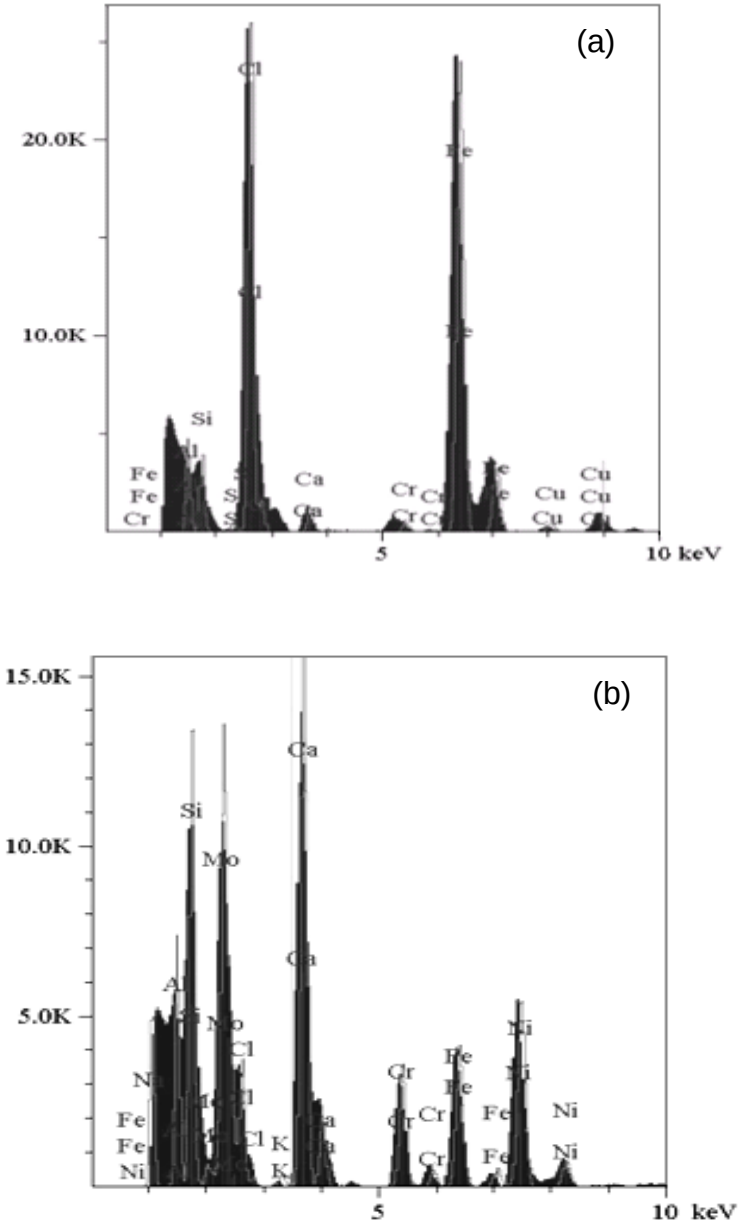

Figure 4.24 Energy dispersive spectroscopy (EDS) analyses indicating the presence of (a) Cu in steel rust extracted from the CS surface and (b) dissolved C22 alloying elements in the light tarnish-like scale scraped off the C22. (From positions indicated on figure 4.23 by the arrows no. 1 and 2, respectively).

Figure 4.21 shows a better agreement between gravimetric and Faradaic values of mass loss obtained from the investigation by Torres-Acosta for cases with nominal C/L from ~ 0.2 to 2 [Torres-Acosta et al. 2004]. The reason for that may be attributed to the relatively high chloride ion concentration of 2% by weight of cement. The higher efficiencies reported in that work may also be related to the lesser dry-out effect of the rebar surrounding due to the shorter exposure durations to impressed currents before cracking (smaller C/Ø). On the other hand, low current efficiencies may have become masked by overestimated gravimetric mass loss values. The use of deformed rebar segments may have contributed to overestimation of mass loss due to removal of mill scale. The absence of alloying elements such as Cr, Si, Mo and Cu in the rebar material used may have caused the susceptibility for base metal attack during chemical cleaning to be relatively high [Torres-Acosta 1999 and Singh et al. 2003]. Similarly, the use of anodic segments obtained from steel pipes with unknown chemical compositions may have been behind excessive susceptibility to over-cleaning leading to overestimated mass loss.

Chloride analysis of concrete powder samples obtained from locations at 5 mm close to rebar and 5 mm close to external surface of specimen U4 showed chloride levels of 2.8 % and 1.7% by weight of cement, respectively. The analysis was performed after de-energizing the specimen upon appearance of surface cracking. As expected, the results suggested that chloride concentration increased at rebar-concrete interface by migration until the critical corrosion threshold level was reached.

Figure 4.25 shows the applied voltage response for a specimen having a single rebar completely composed of C22, subjected to a galvanostatic current density of 100 µA / cm^2. It was shown that current flow through C22-concrete interface is possible within the range of applied voltage values observed at the localized corrosion cases (up to 20 volts). That observation provided additional confirmation for the argument of O_2 evolution on the surface of C22 alloy segments discussed earlier.

Despite the uncertainties associated with current efficiency, the values of critical penetrations (X_{crit}) in this work were only calculated based on gravimetric values of mass loss. Therefore, deviation from Faraday's law due to reasons discussed above will not be of concern. The discussion of those issues was undertaken to highlight some of the pitfalls and uncertainties associated with some of the common procedures used to determine critical penetration (X_{crit})

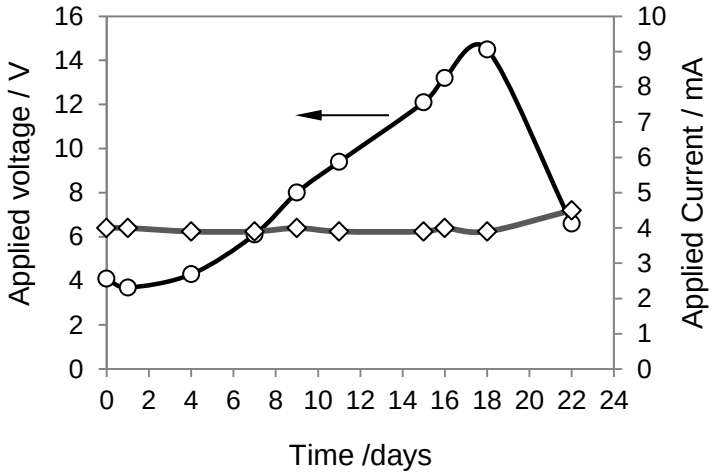

Figure 4.25 Driving voltage response for a cylindrical concrete specimen axially reinforced with a central bar completely made of C22 alloy under galvanostatic control. (Based on a current density of 100 µA/cm^2).

4.2.3 Uncertainties Associated with Gravimetric Evaluation of Rebar Mass Loss

Chemical cleaning as per ASTM G01 is a process of removing the corrosion product (iron oxides) using an inhibited acid solution such as the Clarke's solution in a cyclic fashion. The inhibited acid cleaning (also known as acid pickling) is performed to remove metal oxide with minimum attack to base metal. Figure 4.26 shows a schematic for the main electrochemical reactions likely to be involved In the case of Clarke's solution [Chen et al. 1982]. The kinetics of hydrogen evolution cathodic reaction (Line B) is poisoned by the action of the Sb_2O_3 inhibitor that prevents the recombination of hydrogen atoms. Therefore, the base metal attack (iron dissolution reaction) represented by line C on figure 4.26 is reduced. The function of $SnCl_2$ inhibitor is the reduction of the Fe^{3+} to Fe^{2+} and the stannous ions become oxidized in the process. That effect minimizes the oxidation of base metal [Pearlstein et al. 1967 and Singh et al. 2003].

It appears from the schematic in figure 4.26 that chemical attack to base metal can only be minimized and not completely prevented. The procedure outlined in ASTM G01-03 accounted for the base metal loss by plotting the accumulated removed mass versus the number of cleaning cycles and observing the change in slope. Figure 4.27 (a) shows the rust removal cyclic cleaning for a smooth rebar (free of mill scale) with a clear change in slope. The line with a large slope indicates the rust removal whereas the line with a small slope indicates the base metal attack. On the other hand, figure 4.27 (b) shows the cyclic cleaning for a deformed rebar (with mill scale) with unclear change in slope. The latter suggests continuing removal of mass and make the task of

accurate determination of actual mass loss a difficult one. That observation may be explained by the presence of mill scale on surface of as-received rebars which is made up of high temperature oxides (Fe_2O_3, Fe_3O_4 and FeO). The mill scale thickness was found in the literature to be in the order of 2 to 70 µm as depicted in the SEM images in figure 4.28 [Ghods et al. 2011 and Jaffer et al. 2009]. The mill scale oxides are similar to those produced by aqueous corrosion which makes them equally susceptible to chemical attack during ASTM cleaning [Marcotte 2001]. Therefore, gravimetric evaluation can lead to overestimation of mass loss. The indicated typical thickness of mill scale is in the order of expected depths of critical penetration for the case of uniform corrosion. Therefore, the use of deformed rebar was disqualified in the present investigation.

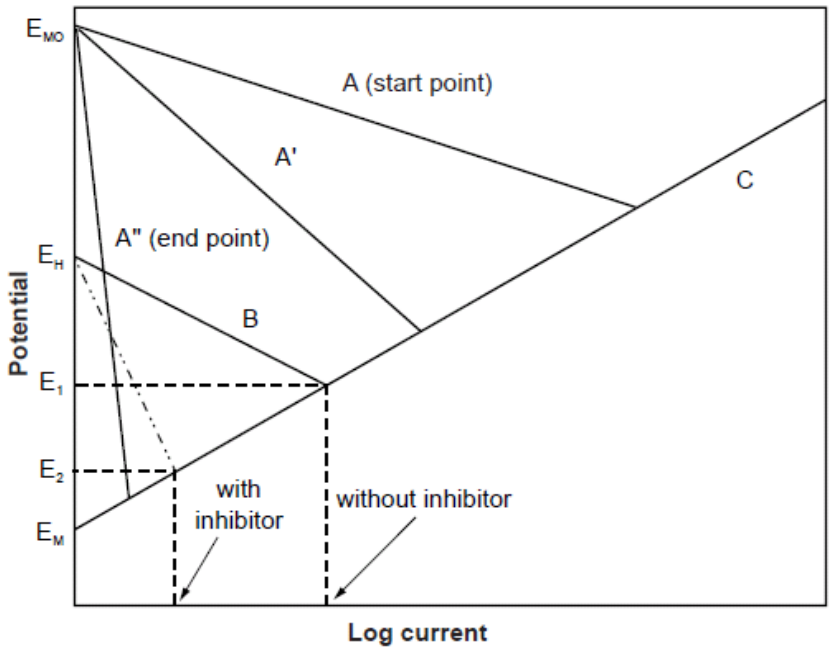

Figure 4.26 E-Log i representation showing effect of cathodic inhibitor on removal rate of metal and metal oxide during chemical cleaning of rust in Clarke's solution [Chen et al. 1982]

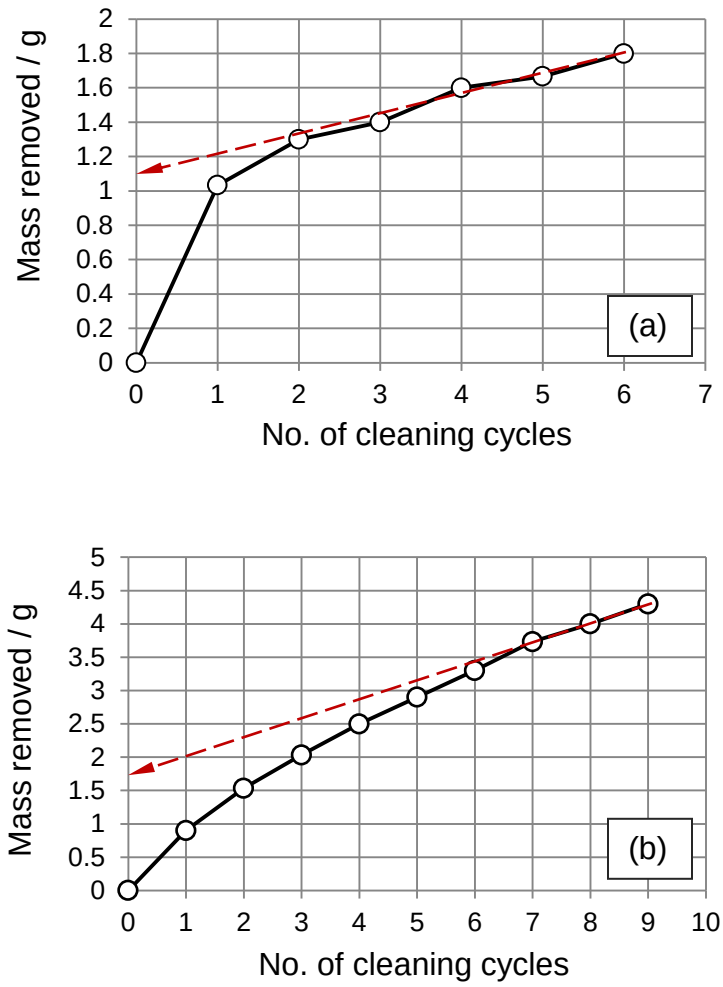

Figure 4.27 Cyclic chemical cleaning process for rust removal showing: (a) clear change in slope for a smooth bar and (b) very slight change in slope for a deformed bar with mill scale. (Smooth: specimen U7, deformed: specimen R2)

The values of mass loss in table 4.2 required for cracking resulting from uniform corrosion of deformed rebars are similar to those in the case of smooth bars. However, it is expected that the mass loss and the corresponding critical penetration be smaller for deformed bars due to the stress concentration effect. The observed larger-than-expected mass loss in the case of deformed rebar may be indicative of mill scale adverse effect in gravimetric measurements. In order to confirm that adverse effect smooth and deformed rebars were cleaned according

to ASTM G01-03 in their as-received conditions without exposure to corrosive conditions.

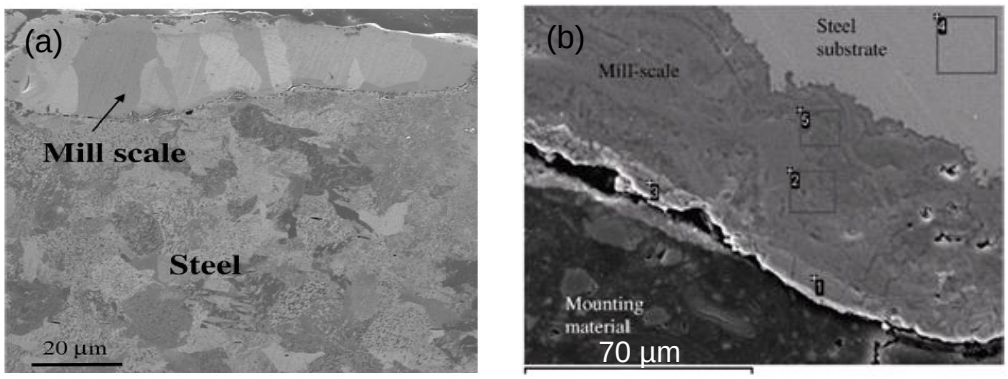

Figure 4.28 SEM images showing a thick mill scale on deformed rebars. (a) [Ghods et al. 2011] and (b) [Jaffer et al. 2009]. By permission from Elsevier Ltd

Table 4.3 shows gravimetric mass loss values for smooth and deformed bars after cleaning in their as-received conditions. The values of mass loss and radius loss in the case of deformed rebars were up to about an order of magnitude greater than those for the case of smooth bars.

Table 4.3 Gravimetric and EIS results of as-received smooth and deformed bars

Steel Bar Type	Sp. #	Gravimetric			EIS				
		Mass loss /g	Radius loss / µm	Average CR /µm.y^{-1}	Rp / Ω	Instantaneous CR / µm.y^{-1}	Rs / Ω	Yo /S^{n}Ω^{-1}	n
Smooth	U8*	0.03	0.42	7	16	151	0.4	0.014	0.79
	U9+	0.13	1.67	29	-	-	-	-	-
Deformed	R4*	0.37	4.04	71	0.49	5307	0.15	0.219	0.83
	R5+	0.47	5.17	91	-	-	-	-	-

(*) Continuous and (+) Cyclic chemical cleaning for 30 minutes in Clarke's solution per ASTM G-01.

The electrochemical impedance results for smooth and deformed bars are shown in table 4.3 and in figures 4.29 and 4.30. The EIS results suggest that the deformed bars with mill scale have a significant reactivity in the Clarke's solution.

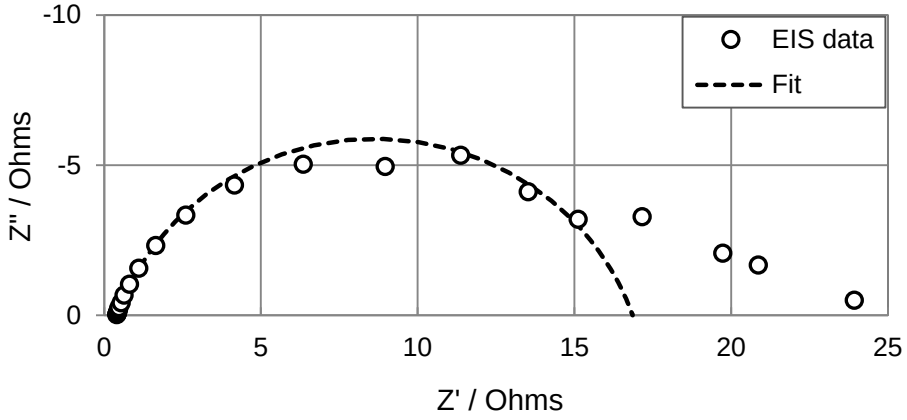

Figure 4.29 EIS response for as-received smooth bar (specimen U8) immersed in Clarke's solution. For a frequency range 0.017 to 10000 Hz at 4 points / decade with equivalent circuit fitting adjusted only over 0.1 to10000 Hz

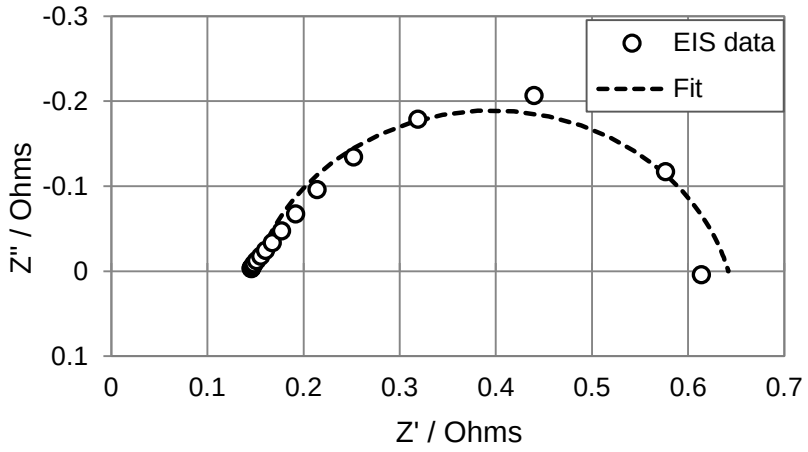

Figure 4.30 EIS response for as-received deformed bar (specimen R4) immersed in Clarke's solution. For a frequency range 0.562 to 10000 Hz at 4 points / decade with equivalent circuit fitting for the entire spectrum.

The above discussion suggested that the as-received deformed rebars can be misleading when used in corrosion experiments involving gravimetric evaluation of mass loss.

4.2.4 Evaluation of Critical Penetration (X_{crit})

Table 4.4 lists the results of calculated critical penetrations (X_{crit}) for the cases of uniform and localized corrosion. The cases of partially corroded surface area of anodic segment were treated in accordance with approaches 1 and 2. The respective values of critical penetration (X_{crit}) from each approach were shown along with their equivalent geometric parameters.

The values of X_{crit} obtained from the present investigation were analyzed along with results from similar previous works. The existing empirical relationship by Torres-Acosta (equation 2.9) was used as a starting formulation due to its simplicity and ease of application. The existing relationship was updated using new data from cases overlapping with that previous investigation and cases extending to larger ratios of C/L. The exponent 2 of the second term $(1+C/L)^2$ in the existing relationship was replaced by (n) to update its value by regression analysis of the new and existing experimental data.

$$X_{crit}/\mathrm{mm} \approx 0.011 \left(\frac{C}{\emptyset}\right) \left(\frac{C}{L} + 1\right)^{n} \qquad (4.3)$$

For the case of uniformly corroding bars (i.e. C/L≈0), equation (4.3) reduces to equation (4.4).

$$X_{crit}/mm \approx 0.011\left(\frac{C}{\emptyset}\right) \quad (4.4)$$

As an additional evaluation, the results of X_{crit} for the cases of full length rebar exposure were compared with data from literature compiled by Torres-Acosta [Torres-Acosta et al. 2004]. As shown in table 4.2, even those cases of uniform corrosion did not exhibit corrosion over the entire rebar surface. The results for those cases of partially affected anode surface were interpreted according to approach 2 treatments. Figure 4.31 displays a graphic comparison indicating a close agreement of the X_{crit} values both with the predictions of equation (4.4) and with the experimental data from literature. The data scatter observed is considered to be falling within typical experimental error expected to prevail in such tests.

In order to determine the value of the exponent (n) to improve equation (4.3), the estimated values of X_{crit} were normalized to the ratio of C/Ø and plotted versus the term representing the degree of localization (1+C/L). Figure 4.32 (a) shows the X_{crit} values for both partially and entirely corroded surface of anode segments using approach (1) treatment wherever needed. Figure 4.32 (a) also shows similar data obtained by Torres-Acosta from cylindrical and prismatic specimens for comparison purposes [Torres-Acosta et al. 2004]. The model

predictions obtained from equations (2.9) and (2.10) for the cases examined were also plotted for comparison. Examination of the experimental data from Torres-Acosta suggested that the normalized critical penetrations X_{crit} / (C/Ø) for the prismatic geometry were generally greater than those for the cylindrical geometry. Although that differentiation was not emphasized in that previous work, it merits consideration here. As discussed earlier, the estimated critical penetrations in that previous work may be associated with uncertainties due to issues related to mass loss determination procedure. Nevertheless, the reported results were used here in combination with the present ones due to lack of similar relevant data in the literature for localized corrosion cases. The present results generally tended to follow the overall trend exhibited by the cylindrical specimens of the previous work. The similarity in trends was confirmed by numerically analyzing the results. A fit of equation (4.3) to the present data yielded an exponent value n=1.23, whereas when fitted to those of Torres-Acosta for cylindrical geometry, it yielded a value of n=1.56. However, when applying the fit to the combined present and previous data obtained for cylindrical geometry, it yielded a value of n=1.26, which is approaching the value obtained from the present work. It may be argued that extending the data set over a range of greater C/L ratios such as those probed here tended to moderate the exponent (n) of dependency in equation (4.3). Likewise, when combining the present data with those of the previous work obtained for both cylindrical and prismatic geometries, the fit yielded a reduced exponent value n=1.38. Application of similar analysis to the previous data by itself yielded values of n=2.02 and n=1.90

for only prismatic and for combined cylindrical with prismatic geometries, respectively. The exponent values obtained here for the cases reported by Torres-Acosta are consistent with the published rounded-off exponent in equation (2.9).

Table 4.4 Critical penetration results including cases exhibiting partially corroded surface interpreted with approaches 1 and 2

Sp. #	Nominal (C/L)	X_{crit} /µm			L_{eq} /cm	(C/L_{eq})	Time To Crack /days
		Entirely Corroded	Partially Corroded				
			Approach 1	Approach 2 (X_{crit} eq)			
U1	0.21	49	-	-	-	-	16
U2		-	24	21.4	17.78	0.25	9
U3		50	-	-	-	-	16
U4		-	41.61	40.91	19.98	0.01	13
U5		-	57.04	52.13	18.57	0.01	13
U7		-	48.94	47.68	19.80	0.01	13
R1		47	-	-	-	-	15
R2		41	-	-	-	-	19
R3		40	-	-	-	-	15
101	1	-	103	51.84	2.21	1.98	48
102		-	133	85.48	2.81	1.55	65
103		-	100	60.83	2.64	1.65	49
201	2	-	95	87.19	1.99	2.2	166
202		-	100	81.49	1.76	2.49	116
203		-	145	84.19	1.26	3.47	117
301	3	206	-	-	-	-	380
302		304	-	-	-	-	443
303		206	-	-	-	-	485
401	4 (Uncracked)	Unbroken					
402		122	-	-	-	-	654
403		Unbroken					
501	5 (Uncracked)	223	-	-	-	-	668
502		Unbroken					
503							

The predictions corresponding to equation (2.9) by Torres-Acosta shown on figure 4.32(a) tended to overestimate critical penetrations for cases with C/L ratios greater than 2. On the other hand, the predictions of equation (2.10) plotted on figure 4.32(a) tended to underestimate the values of critical penetration corresponding to cases having C/L ratios greater than 2.

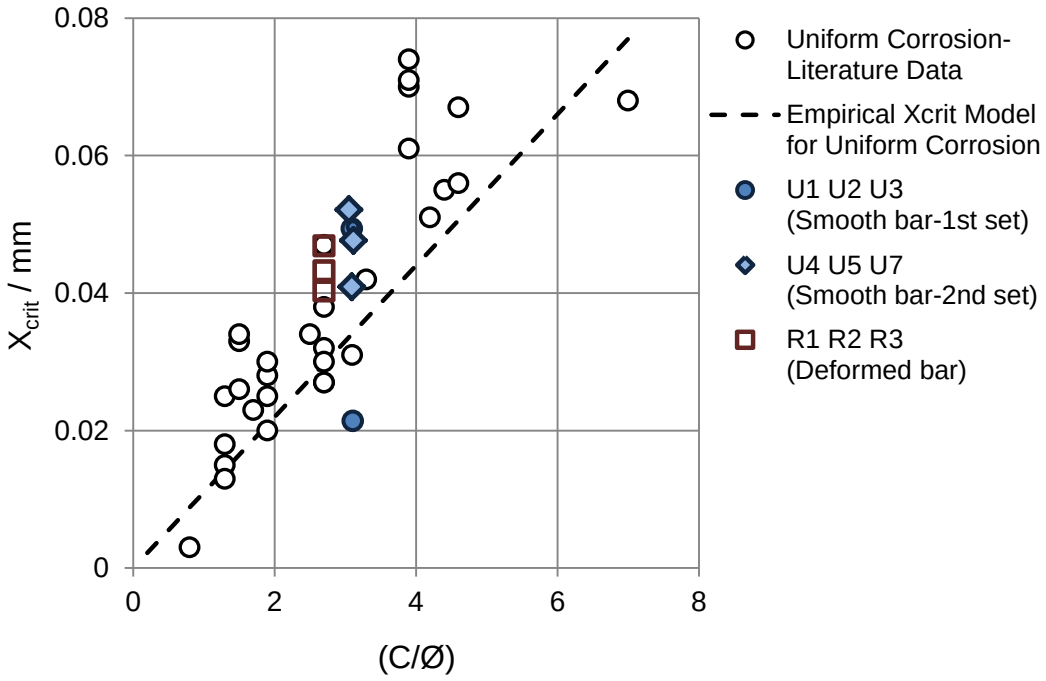

Figure 4.31 Experimental X_{crit} results for the case of uniform corrosion of smooth and deformed bars. The data were treated per approach 2 where necessary and compared with literature data compiled in [Torres-Acosta et al 2004]. The dashed line shows the empirical model prediction for uniform corrosion (equation 4.4)

Figure 4.32 (b) similarly shows the estimated critical penetrations but with the cases of partially corroded surface treated according to approach 2. Proceeding similarly as for approach 1, a fit of equation (4.3) to the present results only yielded an exponent n=1.22. However, when fitting the present results (following approach 2 wherever necessary) in combination with those of

the previous work for cylindrical and prismatic geometries, the exponent was 1.48. The results obtained from both approaches 1 and 2 are comparable and essentially leading to similar conclusions. Therefore, the comparisons of present data with existing model predictions and the comments made on approach 1 in figure 4.32 (a) fairly apply to approach 2 in figure 4.32 (b).

Based on the exponent values obtained from fitting the combined new and existing data using the two approaches, an average generic exponent value n=1.4 was obtained. Therefore, the following modified relationship was proposed as an empirical tool for estimating the critical penetrations for cases affected by localized or uniform corrosion:

$$X_{crit}\ /\mathrm{mm} \approx 0.011\left(\frac{C}{\emptyset}\right)\left(\frac{C}{L}+1\right)^{1.4} \tag{4.5}$$

The present results, extending to more localized corrosion cases than those probed earlier, agree with previous work in finding that more corrosion penetration is needed to induce cracking when the corrosion is localized. The new results suggest that the increase in X_{crit}, while still significant, proceeds following a smaller exponent than that proposed earlier by Torres-Acosta at least for tests with cylindrical specimens. The analysis of results obtained using the approaches 1 and 2 parametric descriptions, for instances where only part of the segment perimeter was affected by corrosion, were not strongly differentiated at

least given the size of the data set and the extent of scatter. In general, the present findings support considering the use of equation (4.5) for application over an extended range of C/L values.

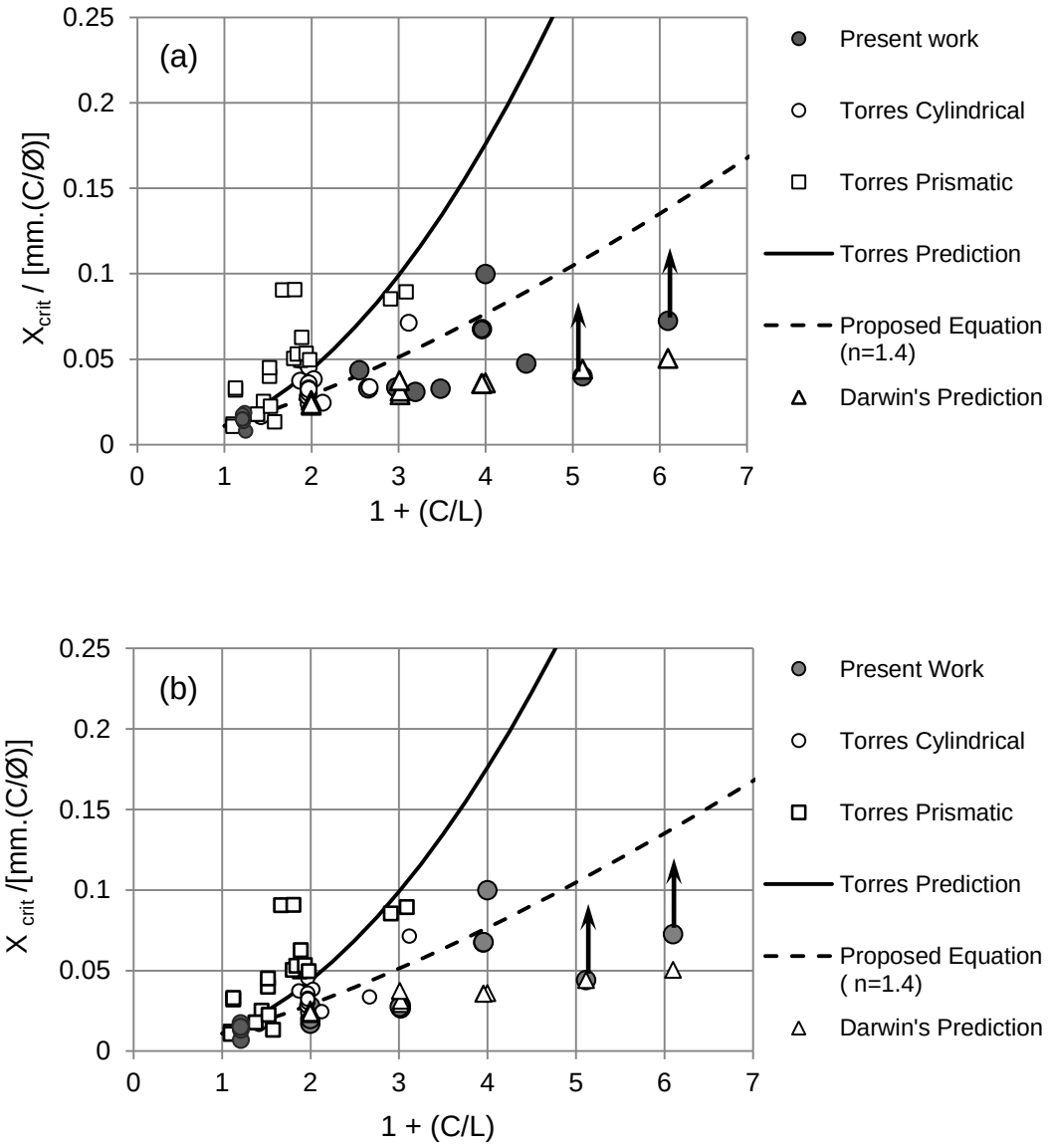

Figure 4.32 Comparison of present experimental X_{crit} results with predictions of proposed equation (4.5) and similar experimental and model prediction data from previous investigations for cases of uniform and localized corrosion. Using approaches (a) 1 and (b) 2, for cases of partially corroded surface area. The symbols indicated with arrows represent uncracked specimens.

5. MODELING

5.1 Introduction

In pursuit of the research objectives (b) and (c), two numerical models were developed using a commercially available finite element (FE) code, Comsol Multiphysics® [Comsol 2008]. The models were formulated to simulate the mechanical and electrochemical aspects of corrosion localization and associated induced cover cracking due to rust expansion. The models highlight the individual effect of each of those two aspects on the onset of corrosion-induced cracking. Numerical formulation was adopted over analytical methods mainly due to the ability of the former to handle the level of complexity introduced by the nature of localized corrosion. Part of that complexity is related to the stress-strain conditions associated with rust expansion in the case of localized corrosion. The mechanical corrosion-induced cracking model is intended to validate and calibrate (if necessary) the modified empirical relationship (equation 4.5) on a theoretical basis. On the other hand, the electrochemical model aims to highlight the possible negative effect of the expected corrosion rate increase on time to concrete cover cracking as corrosion becomes localized. The models simulated the uniform and localized corrosion cases for singly reinforced concrete cylinders having the same geometric parameters as those tested experimentally (figure 5.1). Complicated configurations, representative of real structure conditions, may

be performed by similar procedures. The mechanical and electrochemical behaviors of the corroding segment of the embedded rebar were modeled as an axisymmetric problem around the z-axis as shown in figure 5.2. Those behaviors are deemed to be independent of the angle θ. Likewise, the geometric and material properties are also treated as being symmetric around the z-axis. Therefore, only the rectangular half cross-section shown in figure 5.2 was considered and modeled. The 2D-axisymmetric modeling about the z-axis is a way to simplify 3-D modeling problems [Bennitz et al. 2011].

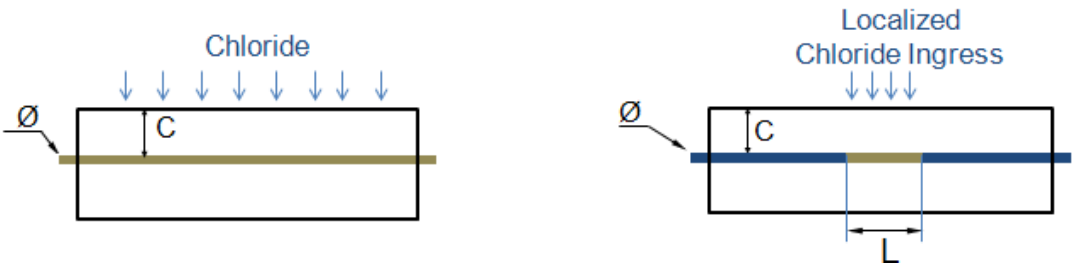

Figure 5.1 Uniformly and locally corroding reinforcing steel in concrete cylinders

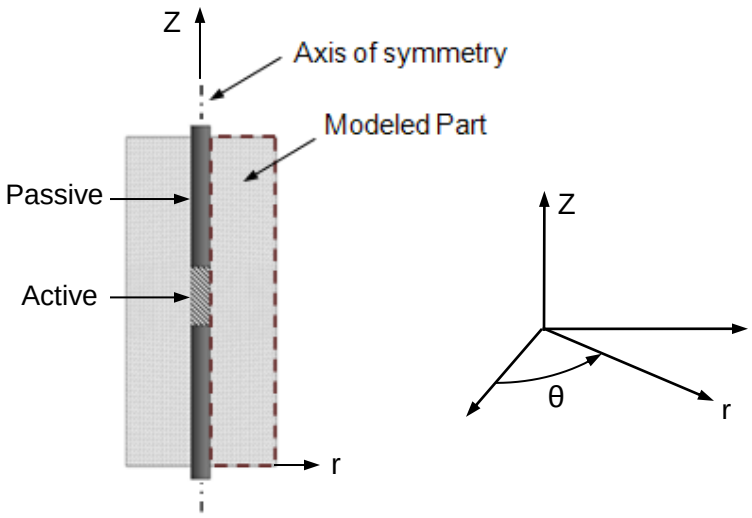

Figure 5.2 2D-Axisymmetric modeling of steel corrosion and cover cracking

5.2 Mechanical FE Modeling of Corrosion Localization Effect on Critical Penetration (X_{crit})

5.2.1 Modeling Approach and Basic Assumptions

5.2.1.1 General

The phenomenon of corrosion-induced concrete cover cracking is known to be caused by the progressive formation of expansive corrosion products around steel reinforcement. Those corrosion products (generally referred to as rust) are characteristic of higher values of relative volume (α_V) ranging from 2.2 to 3.3 compared to that of steel from which they formed [Jaffer et al. 2009]. The produced rust generally tends to occupy the new space left behind by the lost steel before diffusing radially into the surrounding region to fill the concrete pores [Allan et al.1989, Wong et al. 2010]. The porous layer immediately surrounding the rebar is referred to as Interfacial Transition Zone (ITZ). The ITZ is assumed here to have a thickness (d_o) ranging from 15 to 40 μm [Liu et al. 1998, El Maaddawy et al. 2007 and Lazari et al.2000].Generally, once those two available spaces have become filled with rust, the corrosion progression causes internal pressure (P_i) to build up resulting in radial (σ_r) and hoop (σ_θ) stresses in the surrounding concrete. The resulting radial displacement (u) due to those stresses continues to increase and the associated additional space created accommodates further rust product until the stress conditions satisfy the crack initiation and propagation failure criteria. The total radial displacement (u_r) is marked by the appearance of a visible crack on the external concrete surface having a surface crack width of 0.1 mm [Torres-Acosta et al. 2004]. The generated cover cracks are assumed to provide further space to be filled with

rust either partially or completely before full cover cracking occurs [Lu et al. 2011 and Hanjari 2010]. The process of rust formation and concrete cracking is illustrated in figure 5.3 (a). The effect of rust deformability and possible densification when under stress was shown previously to be minimal (less than 10%) and therefore neglected here for simplicity [Chernin et al. 2011].

In order to gain insight on the governing underlying mechanism, complicating factors such as external mechanical loading were disregarded at this time. Therefore, the simplified case of a concrete cylinder axially reinforced with single smooth steel round rebar was modeled, in an attempt to reproduce the experimentally obtained results. The 2D-axisymmetric model treatment indicated above implies that the corroding rebar length was assumed to be uniformly corroding around its perimeter. The concrete surrounding the rebar was considered to be homogeneous and initially isotropic material. The concrete properties were also considered to be time-independent for simplicity. The values of compressive (f'_c=38 MPa) and tensile (f_t=4.438 MPa) strengths used in the model calculations were the actual measured ones obtained from compressive and splitting tensile strength testing, respectively. The strength testing was conducted for non-reinforced concrete cylinders prepared in parallel to the test specimens. The concrete elastic modulus (E=32.39 GPa), shear modulus (G= 13.1 GPa) and Poisson's ratio (ν=0.24) were adopted from a previous work as generic properties [Castorena et al. 2008].

The corrosion-induced stresses and subsequent cracking were modeled as a thick-walled cylinder subjected to internal radial displacement [Bazant 1979, Liu et al. 1998, Chernin et al. 2011, Bhargava et al. 2006 and Pantazopoulou et al. 2001]. Figure 5.3 (b) illustrates the concept of a thick-walled cylinder model. The term thick-walled cylinder typically corresponds to the general case of a pressure vessel with geometric parameters such that the ratio of internal radius to wall thickness is equal to or smaller than ten. The basis for that definition is related to a minimum difference of about 10% between the maximum and minimum hoop stresses across the wall thickness [Poworoznek 2008]. In the present model of thick-walled cylinder, the wall thickness represents the minimum concrete cover depth whereas the internal radius represents the sum of the rebar radius (r) and the thickness of ITZ (d_o).

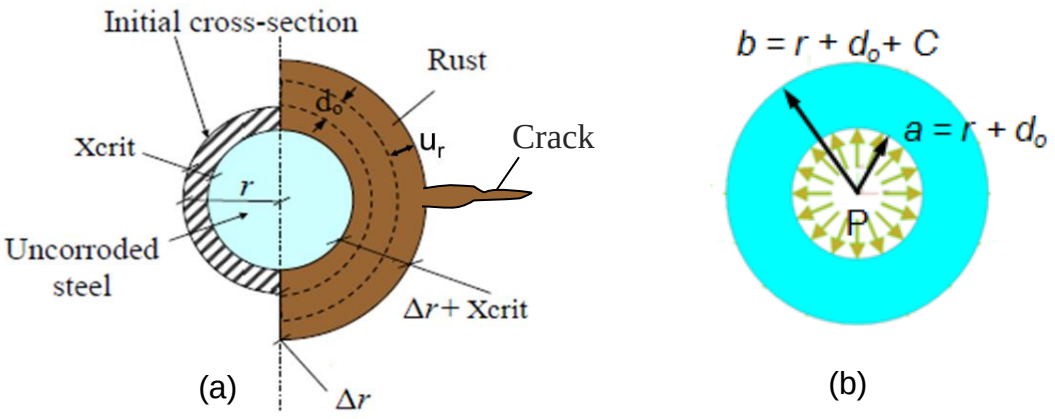

Figure 5.3 Corrosion product formation around reinforcement and cracking: (a) process parameters, (b) equivalent physical model. Modified from [Hanjari 2010]

5.2.1.2 Crack Initiation and Propagation

In both uniform and localized corrosion cases, concrete cover cracking is assumed to initiate at the steel-concrete interface at an arbitrary angle θ and to propagate radially until it reaches the external surface. The cracking process was therefore represented in the finite element model formulation by the concept of smeared cracking [Jendele et al. 2001 and Chen et al. 2008]. The crack width (C_W) was assumed to have a uniform approximate value of 0.1 mm across the concrete cover thickness once it has reached the external concrete surface [Al Harthy et al. 2007].

For uniform corrosion, an empirical cracking criterion was used to indicate full cover cracking (from rebar to external surface). The empirical criterion (equation 5.1) has previously been calibrated and suggested by Nossoni based on the simple Rankine failure criterion of maximum principal normal (tensile) stress [Nossoni 2010]. That empirical criterion requires that the average hoop tensile stress ($\overline{\sigma_\theta}$) through concrete cover be equal to or greater than 0.72 times the concrete tensile strength (f_t) for the cover to fully crack. The concrete material was treated as an isotropic material throughout the entire cracking process.

$$\overline{\sigma_\theta} = 0.72 f_t^{'} \tag{5.1}$$

The cover failure was represented by a single longitudinal parallel to the embedded rebar (figure 5.4) which is generally consistent with the experimental observation presented earlier.

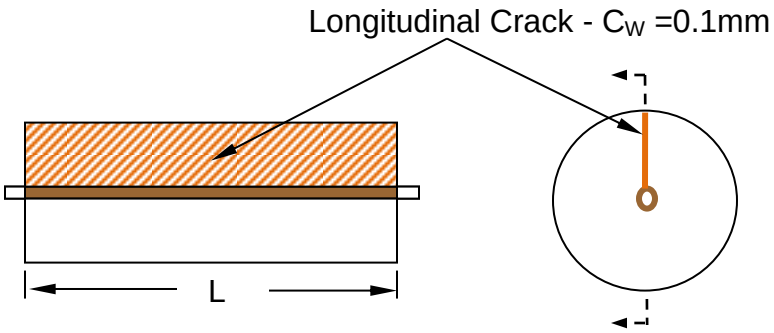

Figure 5.4 Longitudinal cracking in the case of uniform corrosion

On the other hand, no similar cracking failure criterion was found in the literature for detecting full cover cracking for the case of localized corrosion. Therefore, a new approximate approach was established to address both crack initiation and propagation stages using an existing theoretical cracking failure criterion. Cracking was assumed to initiate when the following tension-compression (T-C) criterion was satisfied as illustrated in figure 5.5 [Hu et al. 2003 and Luc 2010]:

$$\left(\frac{\sigma_\theta}{f_t}\right)^3 + \left(\frac{|\sigma_r|}{f_c'}\right) = 1 \qquad (5.2)$$

assuming that the tensile hoop (tangential) stress and the compressive radial stress represent the first and second principal stresses, respectively. Equation (5.2) is originally based on the Niwa model derived for the tension-compression domains of biaxial loading of uncracked concrete [Niwa 1980, Niwa et al. 1981 and Maekawa et al 2003].

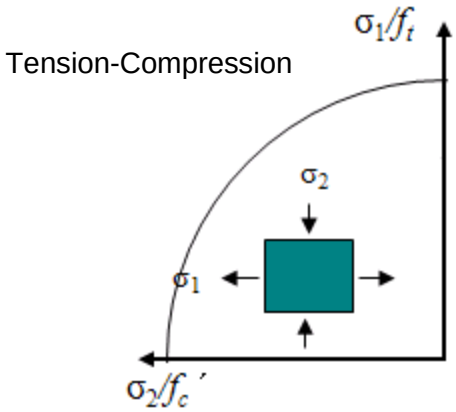

Figure 5.5 Cracking failure envelope in Tension-Compression domain [Luc 2010]

The cover cracking in the case of localized corrosion was represented by a circumferential crack transverse to the embedded rebar also consistent with the experimental observations indicated earlier. Figure 5.6 illustrates the crack modality for its ultimate, full cracking condition.

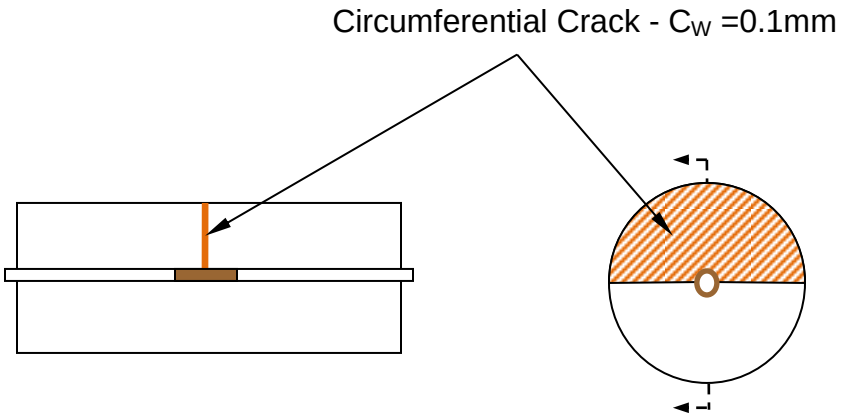

Figure 5.6 Fully developed circumferential cracking for localized corrosion

The following addresses the crack evolution from initiation until reaching the external surface. Concrete cracking does not exhibit an elastic-perfectly brittle

behavior. Therefore it may not accurately be modeled as a linear elastic fracture mechanics (LEFM) problem [Maekawa et al. 2003, Bazant 1979]. Therefore, a new approximate non-linear approach is introduced here as a simple tool capable of addressing the tension-softening behavior of concrete which reflects its residual strength after cracking [CEB-FIP 1990, Hillerborg et al. 1976 and Abdalla et al. 2004]. Previous analytical models of corrosion-induced cover cracking involved the partition of a hollow concrete cylinder into an inner cracked part and an outer un-cracked part. The inner cracked cylinder was treated such that the modulus of elasticity in the direction perpendicular to the crack is reduced. The partitioning method was an attempt to account for concrete tension softening behavior. Detailed description of the thick-walled double cylinder (TWDC) analytical method may be found elsewhere [Chernin et al. 2010].

A similar approach to the TWDC approach was employed in the present model but introducing the use of multiple cylinders (figure 5.7) taking advantage of the capability of numerical methods. This multiple - partition approach facilitates the application of the principles of applied elasticity in modeling the crack initiation and propagation in a non-linear fashion as follows:

(a) The free concrete cover thickness was evenly divided into a number of (m) partitions so that the modeling of an RC cylinder was represented by m concentric concrete cylinders. Each partition had a width (ΔW) equivalent to (1/m) of the cover thickness. The number of partitions was selected here to be five for simplicity and to minimize the model processing time (figure 5.7).

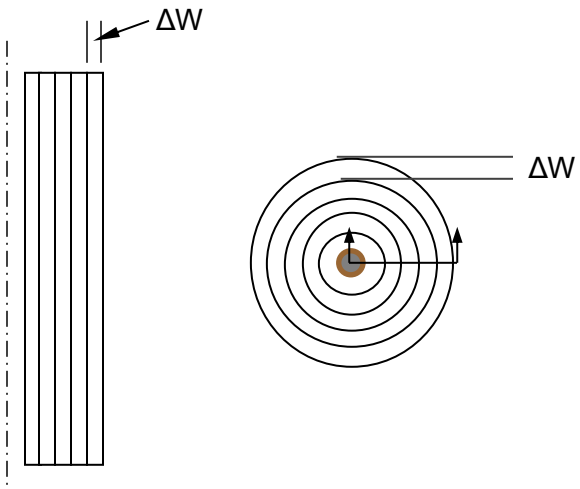

Figure 5.7 Illustration of multiple-partition thick-walled cylinder

(b) Initially all partitions were treated as isotropic material. Incremental steps of prescribed radial displacement were applied along the corroded region of rebar until the cracking criterion is met at the outer radius of the first partition. The amount of radial displacement needed to fully crack the first partition (u_{r1}) is thus obtained.

(c) After the first partition has fully cracked, it is assumed that it completely loses its stiffness properties (E) in the direction perpendicular to the crack direction. The material properties of the cracked partition was therefore adjusted so that the modulus of elasticity was zero ($E = 0$) in the axial direction, if corrosion was localized and in the hoop direction, if corrosion was uniform along the rebar. As such, the cracked partition material is known as orthotropic material since the elastic modulus in the direction of crack propagation is maintained at its original value.

(d) Further displacement (u_{r2}) was applied until the second partition fully cracks and so on until the concrete cover is entirely cracked. Each partition is treated after cracking as an orthotropic material [Pantazopoulou et al 2001].

(e) The total radial displacement (u_r) is made up of the summation of all radial displacements needed to crack each partition as follows:

$$u_r = \sum(u_{r1} + u_{r2} + u_{r3} + u_{r4} + u_{r5}) \quad (5.3)$$

Generally, it should be noted that the empirical cracking failure criterion for the case of uniform corrosion was only used to compare cases of uniform corrosion with different ratios of concrete cover to rebar diameter. The empirical criterion was also used as a verification tool to test the applicability of the multiple-partition cylinder approach by comparing the results of a uniform corrosion case when analyzed by both approaches. The multiple-partition approach was then applied for all uniform and localized corrosion cases for consistency purposes.

As indicated earlier, rust may be accommodated in the space provided by the ITZ porous zone and in spaces made available by the lost steel and the displaced region along the corroded rebar length. Rust may also be accommodated in the generated cracks. In the case of localized corrosion, it was further assumed that the slightly displaced regions along the adjacent passive areas form an additional rust-accommodating space. That displaced regions

along the passive zone extends to a distance (S) on each side of the corroding zone. As a result, the length of ITZ porous zone to be filled with rust along the rebar had to be extended to cover the total length of displaced concrete regions (figure 5.8). Regions where the amount of radial displacement is less than one micrometer were not considered displaced.

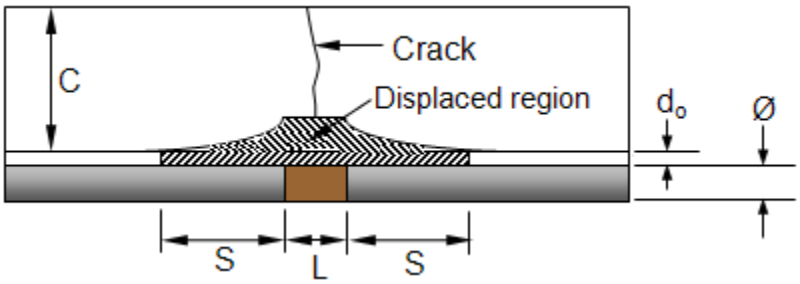

Figure 5.8 Illustration of extent of displaced regions due to localized corrosion

5.2.1.3 Equilibrium Equations and Constitutive Relationships

The stress equilibrium on a three-dimensional element for the general case is shown in figure 5.9 in the cylindrical coordinates for a thick-walled cylinder subjected to internal pressure. The differential equations assuming rotational symmetry ($\partial/\partial\theta=0$, $\tau_{r\theta} = \tau_{\theta r} = 0$, $\tau_{\theta z} = \tau_{z\theta} = 0$) and given that $\tau_{rz} = \tau_{zr}$ are represented by [Sadd 2009]:

$$\frac{\partial \sigma_r}{\partial r} + \frac{\partial \tau_{rz}}{\partial z} + \frac{1}{r}(\sigma_r + \sigma_\theta) = 0 \tag{5.4a}$$

$$\frac{\partial \tau_{rz}}{\partial r} + \frac{\partial \sigma_z}{\partial z} + \frac{1}{r}\tau_{rz} = 0 \tag{5.4b}$$

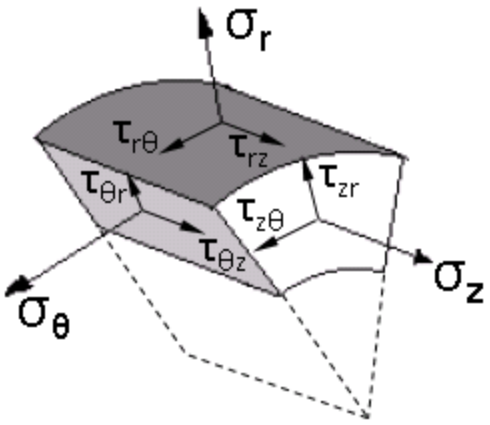

Figure 5.9 Stress equilibrium on a 3D-infinitesimal element within a thick-walled cylinder wall

From Hooke's law, the stress-strain relationships corresponding to axial symmetry ($\gamma_{\theta r} = \gamma_{r\theta} = 0, \gamma_{\theta Z} = \gamma_{Z\theta} = 0$ and $\gamma_{Zr} = \gamma_{rZ}$) are given by the following set of equations:

$$\varepsilon_r = \frac{1}{E}[\sigma_r - \nu(\sigma_\theta + \sigma_Z)] \quad (5.5a)$$

$$\varepsilon_\theta = \frac{1}{E}[\sigma_\theta - \nu(\sigma_Z + \sigma_r)] \quad (5.5b)$$

$$\varepsilon_Z = \frac{1}{E}[\sigma_Z - \nu(\sigma_r + \sigma_\theta)] \quad (5.5c)$$

$$\gamma_{rz} = \frac{1+\nu}{E} + \tau_{rz} \quad (5.5d)$$

The resulting displacement in the r-θ plane is shown in figure 5.10. The strain – displacement relationships considering the tangential displacement $u_\theta=0$ may be given by the following [Bennitz et al. 2011]:

$$\varepsilon_r = \frac{\left(u+\frac{\partial u}{\partial r}\Delta r\right)-u}{\Delta r} = \frac{\partial u}{\partial r} \tag{5.6a}$$

$$\varepsilon_\theta = \frac{(r+u)\Delta\theta - r\Delta\theta}{r\Delta\theta} = \frac{u}{r} \tag{5.6b}$$

$$\varepsilon_Z = 0 \tag{5.6c}$$

$$\gamma_{Zr} = \frac{1}{2}\left(\frac{\partial u}{\partial Z} + \frac{\partial w}{\partial r}\right) \tag{5.6d}$$

where w is the axial displacement. The three sets of equations 5.4, 5.5 and 5.6 may be combined by substitution. The resulting differential equations may be solved numerically for stresses, strains and displacements at all points within the concrete cover using the boundary conditions shown in figure 5.11. The pressure is equivalent to the amount of radial stress at the rebar to concrete interface.

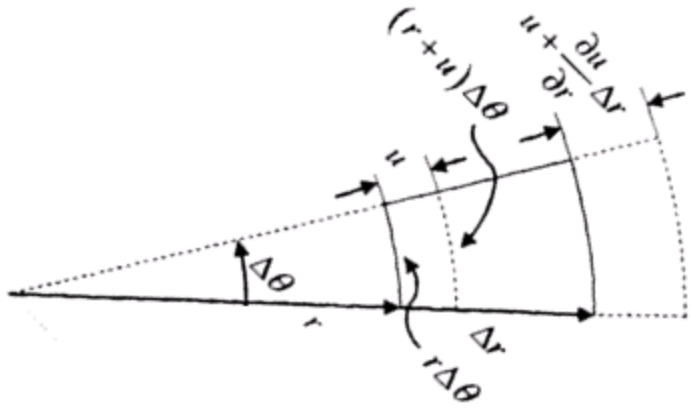

Figure 5.10 Generated radial and hoop displacements [Bennitz et al. 2011]

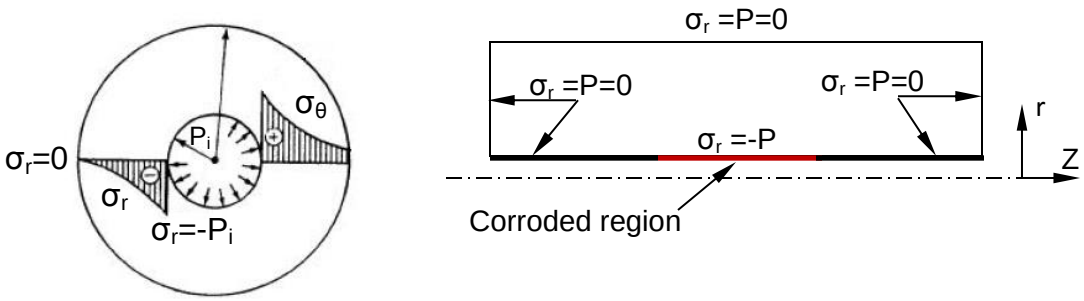

Figure 5.11 Boundary conditions. Schematic on left modified from [Sadd 2009]

5.2.2 Model Implementation

The Comsol Multiphysics® FE code was employed to solve the governing equations and implement the implied assumptions using a mesh size having at least 20,000 triangular elements. The model sensitivity to mesh size was tested to ensure reliable model outputs (appendix B, figure B.18). The radial displacement at the cylinder inner radius was treated as an input parameter in the model and the model yielded the stresses and strains at all points as well as the corresponding internal pressure. The following formulations were used to calculate the critical penetration (X_{crit}):

(a) Uniform Corrosion

For the unit length of a rebar, the following applies:

$$Vr - Vs = \pi [(r+\Delta r)^2 - r^2] \quad (5.7)$$

where Vr and Vs are volumes per unit length of rust and lost steel, respectively. Parameters r and Δr are shown in figure 5.3. Considering $\Delta r \ll r$, assuming the ITZ porosity is very high, and rearranging gives:

$$Vs\,(\alpha_v - 1) = 2\pi r \Delta r$$

$$2\pi r X_{crit}\,(\alpha_v - 1) = 2\pi r \Delta r$$

replacing Δr with $(u_r + d_o)$ from figure 5.3, the critical penetration X_{crit} without considering the rust filling the induced crack is given by:

$$X_{crit} = \frac{u_r + d_o}{(\alpha_V - 1)} \quad (5.8)$$

The critical penetration (X_{crit}) in the case of rust completely filling the induced crack (longitudinal in the uniform corrosion case) is given by:

$$X_{crit} = \frac{u_r + d_o}{(\alpha_V - 1)} + \frac{C_W\, C\, L}{(\alpha_V - 1) 2\pi r L} \quad (5.9)$$

where C_W is crack width, C is concrete cover and L is the length of rebar affected by corrosion.

(b) Localized Corrosion

The total volume of rust needed for cover cracking (V_T) is given by:

$$V_T = V_s + V_u + V_{do} \tag{5.10}$$

where V_s is the original volume of lost steel that turned into rust and estimated by:

$$V_s = 2\,\pi\, r\, X_{crit}\, L \tag{5.11}$$

V_u is the new volume created around rebar along the displaced region (L+2S) and given by:

$$V_u = A_u\, 2\pi\, (r + d_o) \tag{5.12}$$

where the area A_u is the radial displacement (u_r) integrated along the axial direction over the displaced region (L+2S), at full cracking obtained from the FE model. And V_{do} is the volume of interfacial transition zone (filled with rust) along the length of displaced regions and may be approximated by:

$$V_{do} = d_o(L+2S)\, 2\pi r \tag{5.13}$$

Since $V_s = V_T/\alpha_V$, it follows then that:

$$V_S = \frac{V_u + V_{do}}{(\alpha_V - 1)} \tag{5.14}$$

and by inserting equation 5.11 into 5.14, the critical penetration (X_{crit}) without considering any rust filling the induced crack (circumferential in the localized corrosion case), is as follows:

$$X_{crit} = \frac{V_u + V_{do}}{2\pi r\, L\, (\alpha_V - 1)} \tag{5.15}$$

If considering that the induced crack is completely filled with rust, the critical penetration (X_{crit}), may be approximated by:

$$X_{crit} = \frac{V_u + V_{do}}{2\pi r\, L\, (\alpha_V - 1)} + \frac{1/2}{2\pi r\, L\, (\alpha_V - 1)}\, [\pi(r + d_o + C)^2 - \pi(r + d_o)^2]C_W \tag{5.16}$$

5.2.3 Model Input Parameters and Cases Considered

Tables 5.1, 5.2 and 5.3 list the input parameters for the modeled cases with values generally representative of those obtained experimentally. The input radial displacement increment employed was as small as 0.1 μm [Zhou et al. 2005].

Table 5.1 General model parameters

Parameter	Value
Tensile strength [f_t] / MPa	4.438
Compressive strength [f'_c] / MPa	38
Elastic modulus [*E*] / GPa	32.39
Shear modulus [G] / GPa	13.1
Poisson's ratio [v]	0.24
Thickness of interfacial transition zone [d_o] / μm	15, 20, 40
Relative volume of rust [α_V]	2.2, 3, 3.5
Surface crack width [Cw] / mm	0.1

Table 5.2 Parameters for the uniform corrosion cases

Parameter	Base Case	Case 1	Case 2
Concrete Cover [C] / mm	43.7	28, 56	43.7
Rebar diameter [Ø] / mm	14	14	21.85, 10.92
(C/Ø)	3.1	2, 4	2, 4
Rebar length affected by corrosion [L] /mm	203.3		
Total length of embedded rebar / mm	203.3		
Partition width [ΔW] / mm	8.738	-	-
Cracking failure criterion	Empirical, Tension-Compression	Empirical	

Table 5.3 Parameters for the localized corrosion cases

Parameter	Value
Concrete Cover [C] / mm	43.7
Rebar diameter [Ø] / mm	14
(C/Ø)	3.1
Rebar length affected by corrosion [L] /mm	43.1, 21.6,14.7, 10.6, 8.6
Total length of embedded rebar / mm	203.3
(C/L)	~ 1, 2, 3, 4, 5
Partition width [ΔW] / mm	8.738
Cracking failure criterion	Tension-Compression

5.2.4 Model Results

The results obtained from the FE code for the case of uniform and localized corrosion are given in appendix B (figures B.1 to B.15). Table 5.4 shows a

comparison between the values of critical penetration (X_{crit}) obtained by applying both the empirical and tension-compression cracking criteria, for the base case in table 5.2. The values of X_{crit} were in a good agreement with each other based on the two criteria whether or not the induced crack was filled with rust. The commonly reported parameter values of α_v=3 and d_o=20 µm were selected for comparison purposes [El Maaddawy et al. 2007, Chernin et al. 2011 and Jamali et al. 2013]. Likewise, the pressure needed for crack initiation using both cracking criteria showed also a reasonable agreement. The values of cracking pressure were found to be in a good agreement with the results of the cracking pressure model for uniformly corroding rebars, proposed by Munoz et al [Munoz et al. 2007]. The calculated pressure from Munoz's cracking pressure model (equation 5.17) was found to be 17.81 Mpa.

$$\frac{P_C}{f_t} = \left(2.3384\frac{C}{\phi}\right)^{0.7017} \tag{5.17}$$

Table 5.4 Comparison of results for the case of uniform corrosion obtained from analysis by the empirical and Tension-Compression cracking failure criteria

(For α_v=3, do=20 µm, Ø=14 mm and C=43.7 mm)		Cracking Failure Criterion	
		Empirical	Tension-Compression
X_{crit}/µm	0% rust in crack	12.75	15.15
	100% rust in crack	62.24	64.64
Critical Pressure for Crack Initiation/Mpa		19.47*	17.84

* Empirical cracking criterion implies entire cracking of concrete cover at the indicated pressure

Based on the above description, the theoretical tension-compression criterion may reasonably be employed as a valid cracking criterion for crack detection in the non linear FE analysis of uniform and localized corrosion cases.

In order to examine the effect of the ratio of C/Ø on the value of X_{crit}, the base case in table 5.2 was compared with cases 1 and 2. The ratio of C/Ø was varied either with the concrete cover held constant or with the rebar diameter held constant. The latter was intended to verify whether any of those two parameters has an individual effect different from that manifested by the ratio. The empirical cracking criterion was used in this analysis for speedy processing. Figure 5.12 confirmed the previously well-established increase in the amount of X_{crit} with the increase in the ratio of C/Ø. The effect of the C/Ø ratio on the X_{crit} was found to be nearly the same for a given C/Ø value regardless of the specific values of concrete cover and rebar diameter. The results of X_{crit}, obtained from the FE analysis (for α_v=3 and d_o=20 μm), with the induced cracks being half full of rust seem to be nearly coinciding with the values predicted by the empirical X_{crit} model for uniform corrosion (equation 4.5). Figure 5.13 shows that the X_{crit} results obtained by FEM corresponding to crack filling-conditions of 0% and 100% form an envelope enclosing experimental results from the present and previous investigations. The uniform corrosion X_{crit} data indicated on figure 5.13 include data previously compiled by Torres-Acosta [Torres-Acosta et al. 2004]. The empirical X_{crit} model prediction seems to be equivalent to about 50% rust-filling condition which is in agreement with the experimental observation.

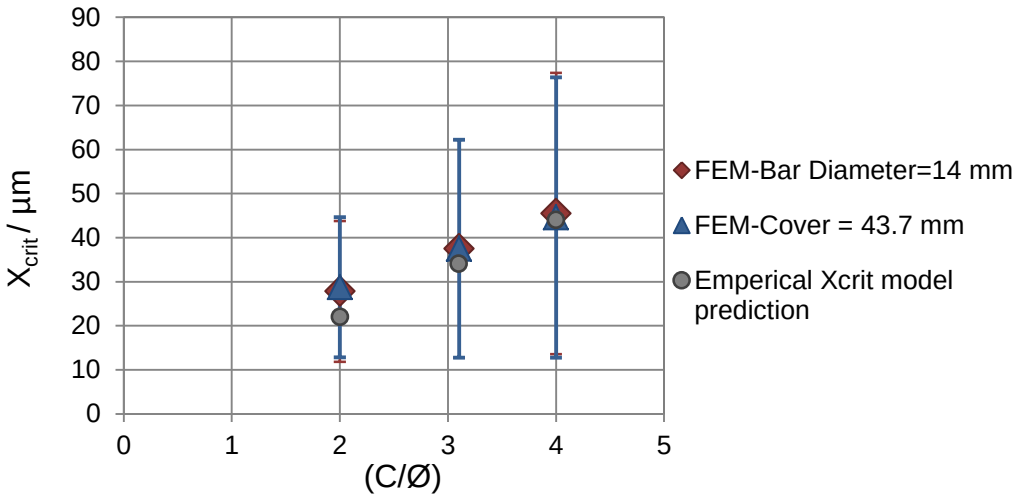

Figure 5.12 Effect of variability in cover and rebar diameter on X_{crit}. The effect was examined for α=3 and d_o=20 µm. The lower and upper ends of error bars represent zero and 100% rust in crack, respectively

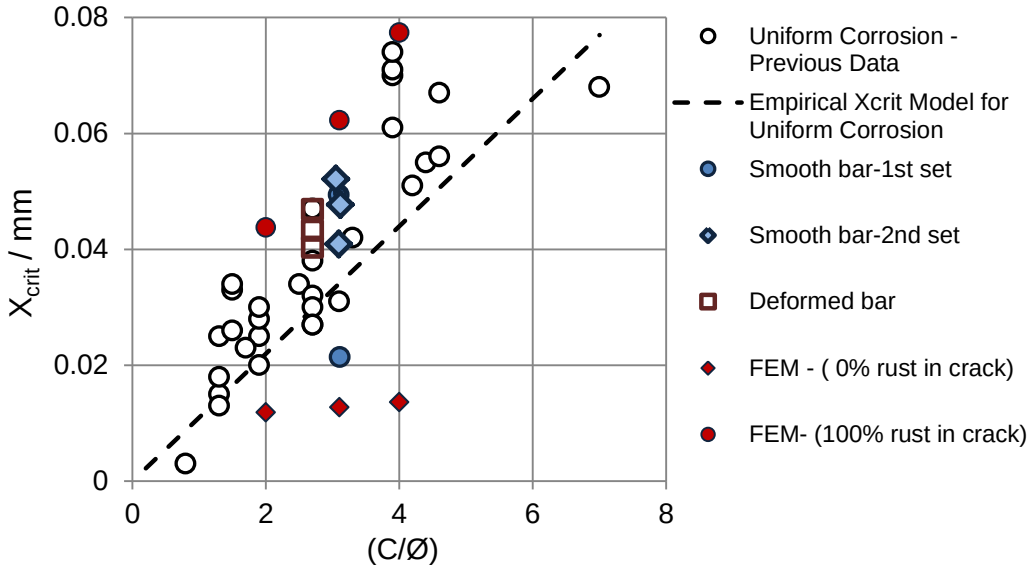

Figure 5.13 Effect of cover to rebar diameter ratio on X_{crit}. The FEM results shown are for constant rebar diameter (Ø=14 mm), α=3 and d_o= 20 µm

The tension-compression cracking criterion was used for the analysis of the base case of uniform corrosion in table 5.2 and for the localized corrosion cases in table 5.3. The critical penetration values (X_{crit}) were calculated using the parameters of rust relative volume and thickness of ITZ from table 5.1. Rust-

filling conditions for cracks of zero and 100% were considered. Figures 5.14 to 5.16 show that the amount of X_{crit} increases as corrosion becomes more localized and that increase is more pronounced when considering the amount of rust filling the induced crack. That finding confirms the experimental observation.

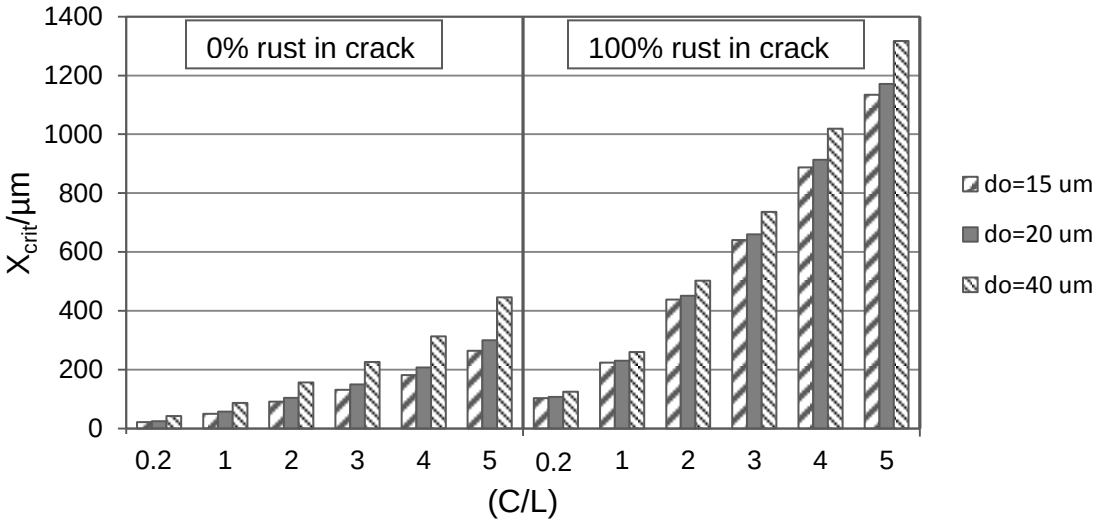

Figure 5.14 FE model results of X_{crit} increasing with the degree of localization for Ø=14 mm, C=43.7 and α_V=2.2. The effects of the size of interfacial transition zone (d_o) and the amount of rust filling the induced crack are shown.

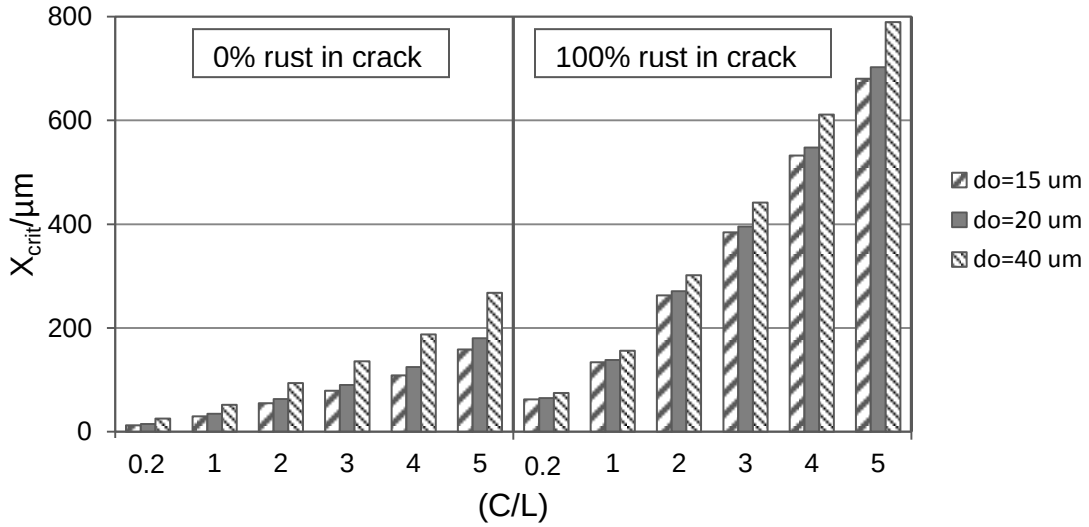

Figure 5.15 FE model results of X_{crit} increasing with the degree of localization for Ø=14 mm, C=43.7 and α_V=3. The effects of the size of interfacial transition zone (d_o) and the amount of rust filling the induced crack are shown.

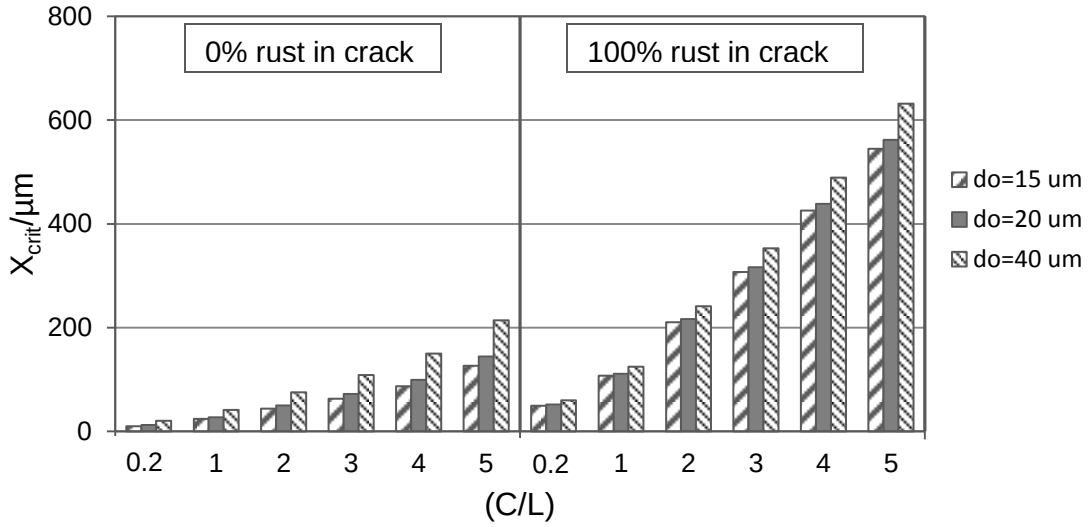

Figure 5.16 FE model results of X_{crit} increasing with the degree of localization for Ø=14 mm, C=43.7 and α_V=3.5. The effects of the size of interfacial transition zone (d_o) and the amount of rust filling the induced crack are shown.

Figures 5.14 to 5.16 also highlight the effect of type of rust (α_V) and the quality of interfacial transition zone (d_o) on the amount of X_{crit}. As expected, the increase in the rust relative volume (α_V) caused the amount of X_{crit} to decrease whereas the increase in ITZ thickness (d_o) caused it to increase. The decrease in rust relative volume (type of rust) from 3.5 to 2.2 seemed to have increased the amount of X_{crit} by up to about a factor of two. The influence of ITZ thickness tended to diminish when the induced cracks become either partially or completely filled with rust. The rust-filling condition of induced cracks appeared to be a significant factor influencing the amount of X_{crit}. A crack full of rust can result in an increased value of X_{crit} by up to four folds compared to a similar case having an empty crack.

Figure 5.17 (a) illustrates the contribution of each partial radial displacements (u_{r1} to u_{r5}) needed to crack each partition in the overall radial

displacement (u_r) needed for full cover cracking. The radial displacements required for both crack initiation and propagation increase as the degree of localization increases, regardless of the rust-filling condition of the induced cracks. It can be observed from figure 5.17 (a) that the cases of uniform (C/L=0.2) and localized (C/L=1 to 4) exhibited full cover cracking once partition 4 has cracked. On the other hand the case of localized corrosion (C/L=5) has not fully cracked until partition 5 has cracked. That observation implies that the length of stable crack, beyond which sudden unstable cracking occurs, increases also as corrosion becomes highly localized. Figure 5.17 (b) shows that the total radial displacement needed for full cover cracking increases linearly as the degree of localization increases.

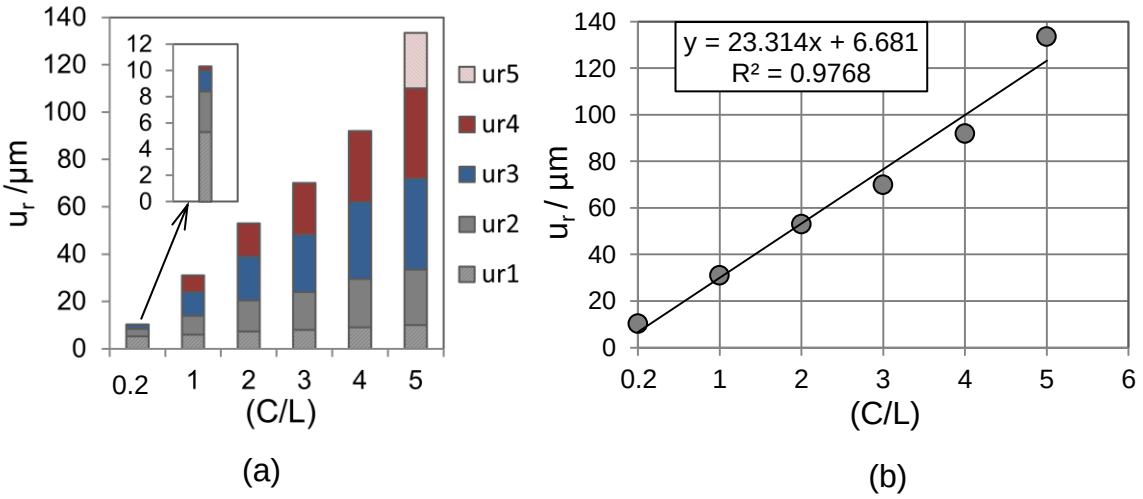

Figure 5.17 Radial displacement required for concrete cracking of: (a) each cylinder partition wall thickness and, (b) entire cover thickness

The critical pressure for crack initiation was also observed to be linearly increasing as the degree of localization increased as depicted in figure 5.18. The pressure required for crack initiation in the case of highly localized corrosion of

C/L=5 tended to be about three times as high as that of uniform corrosion. Comparison with the critical cracking pressure values calculated based on Torres-Acosta's cracking pressure model (equation 5.18) showed slightly higher values than the FEM-obtained ones for the case of uniform corrosion. Similar comparison trends between FEM and TWDC models of uniform corrosion were reported in the literature [Chernin et al. 2011]. The FEM-derived pressure values were increasingly less than those obtained by Torres-Acosta as corrosion became more localized. That difference may be attributed to the procedure by which the empirical equation (5.18) was derived. The procedure involved collecting strain data from strain gauges attached to the external concrete surface upon onset of cracking. The concept of thick-walled cylinder was applied using those data to calculate the corresponding failure pressure for the geometry of test specimens. That analysis did not account for crack propagation which implies that cracking was assumed to have initiated at the same time as it appeared on the external surface. Therefore, the resulting overestimation tended to increase as corrosion became more localized likely due to the relatively longer crack propagation times required as was predicted from the trends in figure 5.17.

$$\frac{\text{Cracking Pressure}}{f_t} = 1.54\frac{C}{\emptyset}\left(\frac{C}{L}+1\right)^{0.72} \qquad (5.18)$$

Figure 5.19 shows the total radial displacements (u_r) indicated in figure 5.17 and the adjacent radial displacement along the passive regions on both sides of the corroding zone. The length of displaced region (S) along the passive zone

increased as corrosion became more localized. Since that length is likely to provide a space for rust accommodation, experimental evidence was needed for verification.

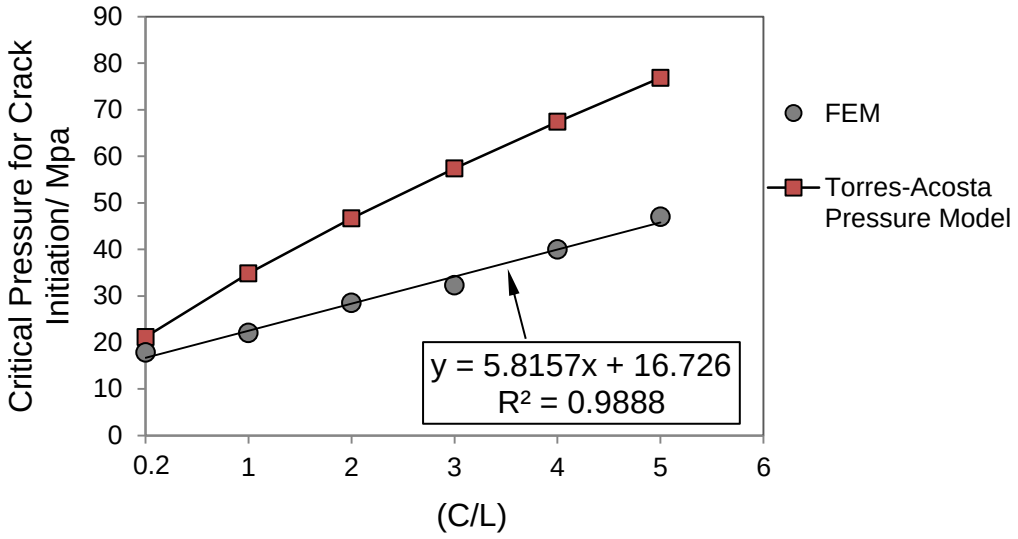

Figure 5.18 Critical internal pressure required for initiation of cover cracking

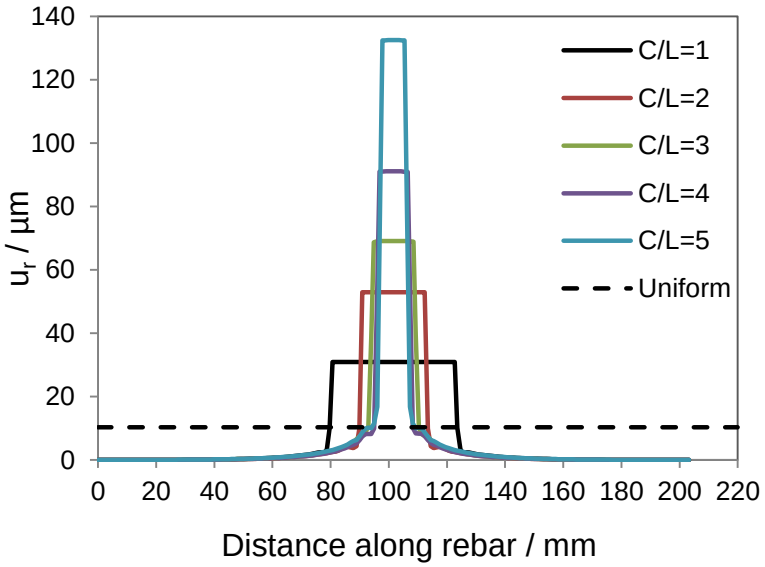

Figure 5.19 Radial displacement along rebar at full cover cracking and extent (s) of displaced regions along adjacent non-corroding zones expected to accommodate further rust for cases of localized corrosion

Figure 5.20 shows a comparison between the lengths of displaced region (S) obtained from the FEM analysis and the lateral rust propagation along rebar observed experimentally. The comparison exhibited a reasonable agreement with slight deviations likely to be due to possible presence of air voids or the non-uniform distribution of corrosion around rebar perimeter. The former results in longer than expected extent of rust while the latter may be associated with non-uniform radial expansion leading to shorter displaced regions.

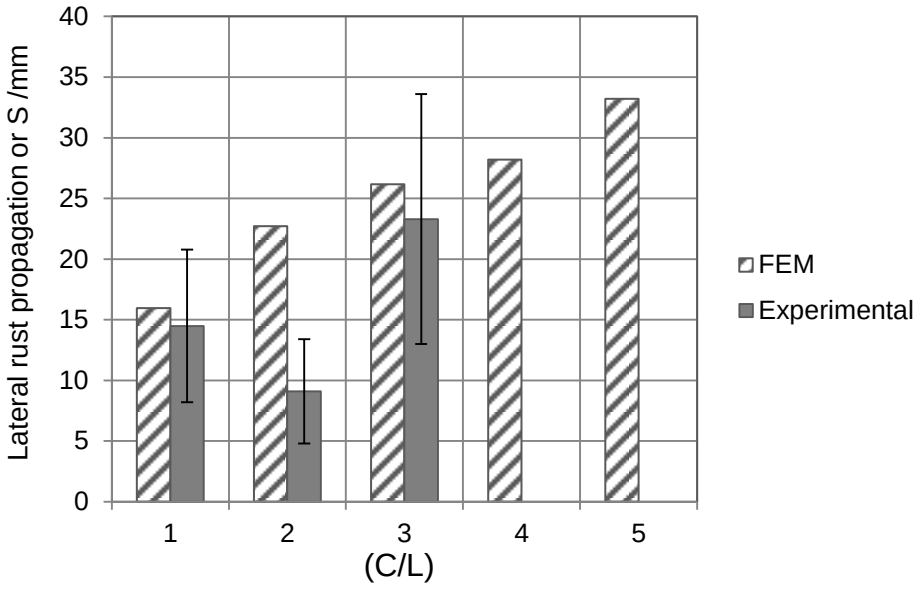

Figure 5.20 Lengths of displaced regions (s) compared to the observed extents of rust transported on each side of a corroding spot

5.2.5 Validation of the Modified Empirical Relationship

The FE analysis results were used to test the validity of the modified empirical relationship (equation 4.5) on a theoretical basis. The FE results of X_{crit} in figure 5.15 obtained using parameter values of rust relative volume (α_V=3) and thickness of ITZ (d_o=20 μm) were used for the verification process. Part of the

reason is that those parameter values are the commonly selected ones in the literature for modeling of uniform corrosion [Jamali et al. 2013]. As noted earlier, those parameter values provided reasonable predictions in the case of uniform corrosion with induced cracks being half full of rust. Therefore, the same parameter values were adopted for both uniform and localized corrosion since they are independent of corrosion morphology.

Figure 5.21 and 5.22 compare the FEM results of X_{crit} with the current and previous experimental results and predicted results obtained from the existing models for X_{crit} due to localized corrosion. Figure 5.21 and 5.22 involve experimental data obtained from specimens having partially corroded perimeter treated according to approach (1) and (2), respectively. The FEM results were plotted on the graphs as floating bars covering the range of all possible rust-filling conditions of induced cracks (i.e. 0 to 100%). For all tested C/L ratios, the FEM predicted X_{crit} values tended to form envelopes enclosing all experimental data except some previous data correspondent to prismatic RC specimens [Torres-Acosta et al. 2004]. The greater values of X_{crit} associated with those prismatic specimens may be attributed to the prismatic geometry likely to require greater pressure to crack due to the greater effective depth of cover. That possible geometric effect however was not tested in the FEM analysis. It may also be related to the multiple-cracking failure mode reported for that geometry which provides additional space to accommodate further rust [Torres-Acosta 1999]. Another reason may be related to over-cleaning issues of as-received rebars discussed earlier. The lower bound of FEM results, corresponding to 0% rust in

crack, seemed to coincide with the model predictions by Darwin et al. for all ratios of C/L [Darwin et al. 2011]. On the other hand, the upper bound of FEM results, corresponding to 100% rust in crack, seemed to approach the model predictions by Torres-Acosta up to C/L ratio of 2. Nevertheless, the present experimental results tend to be located at about 50% rust-filling. The proposed modified relationship (equation 4.5) also seems to be positioned at about 50% rust-filling which reflects a reasonable agreement with experimental findings.

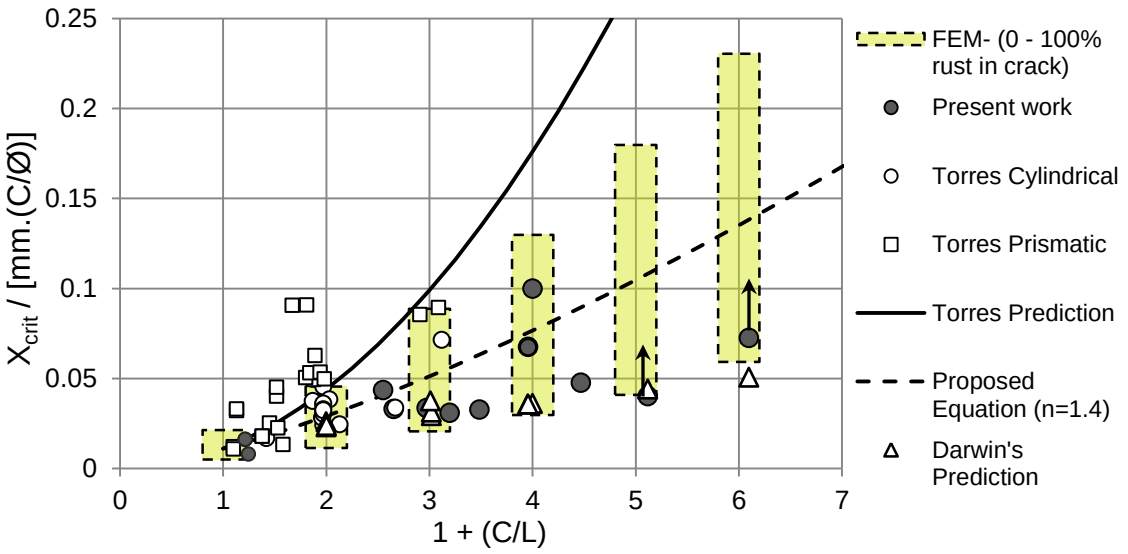

Figure 5.21 Comparison of FE model findings (for α=3 and d_o=20 µm) with current and previous experimental results and existing model predictions with partially corroded cases treated as per approach 1. The bottom and top ends of the yellow floating bars represent zero and 100% rust in crack, respectively. The symbols shown with arrows indicate un-cracked specimens.

Even though there was no reliable experimental means to quantify the actual amount of rust in cracks, it was observed that the induced cracks were partially filled with rust. Partial rust filling may be attributed to the tendency of a crack to suddenly propagate (unstable growth) up to failure when reaching a

critical length, thereby not permitting further rust filling. Another likely reason for not completely filling an induced crack is the possible exerted pressure by the rust filler on the crack faces leading to rapid cracking. It may therefore be concluded that equation 4.5 can be considered a useful tool to provide reasonably reliable information on the amount of critical penetration required for concrete cover cracking.

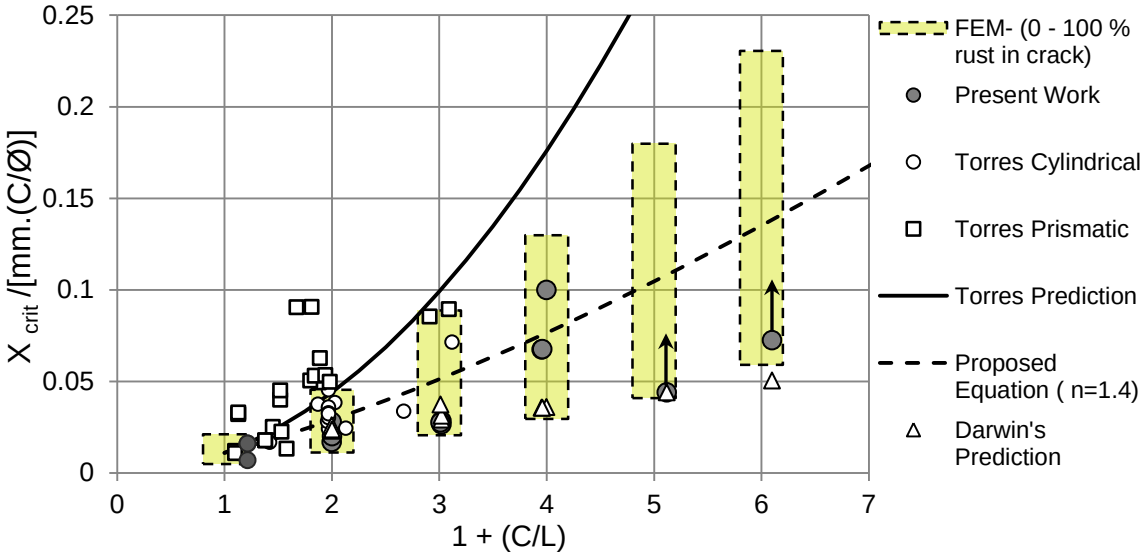

Figure 5.22 Comparison of FE model findings (for α=3 and d_o=20 µm) with current and previous experimental results and existing model predictions with partially corroded cases treated as per approach 2. The bottom and top ends of the yellow floating bars represent zero and 100% rust in crack, respectively. The symbols shown with arrows indicate un-cracked specimens.

5.3 Electrochemical FE Modeling of Corrosion Localization Effect on Corrosion Rate

5.3.1 Introduction

The cases of localized corrosion tested experimentally were simulated to determine their freely-corroding behaviors (with no external current being

applied). The simulation aims to explore the possible variation in corrosion rate (CR) as a function of the degree of corrosion localization (corroding to passive area ratio). Corrosion rate is expected to be affected by various factors such as level of oxygen and moisture [Hussain et al. 2012 and Busba et al. 2013b]. It was therefore decided to consider two scenarios thought to approximately define the upper and lower bounds of possible steel corrosion rates in concrete under the modeled conditions [Subramaniam et al. 2010]. The upper bound is a situation in which the total corrosion current is entirely induced by the action of macrocell current flowing between a pure anode (active region) and a pure cathode (passive regions). The lower bound however is where the total corrosion current is completely due to the action of microcell current effect taking place on the anode region only with no macrocell current effect from passive regions. The 100% macrocell current scenario represents a case where oxygen access is possible to the adjacent passive regions through concrete cover to fuel the cathodic reaction. On the other hand, the 0% macrocell current scenario represents a case where oxygen access is only possible to the anode region such as through a narrow crack in high quality concrete [Raupach 1996, Schiessl et al. 1997 and COIN 2008]. Further, it is known that corrosion rate does not remain constant over time but gradually decreases over time. That decrease has been attributed to corrosion product build-up on the anode region which limits the anodic reaction kinetics [Otieno et al. 2011, Vu et al. 2000, Liu et al. 1998, Glass 2000 and Tuutti 1982]. In order to account for corrosion rate evolution with time, the results from the FE analysis outputs were used to calculate both time-

invariant and time variant corrosion rates. Variation of corrosion rate with time is not well understood due to seasonal variations and uncertainties of measurements. Therefore, the currently available simple predictive model suggested by Vu and Steward [Vu et al. 2000] was used here for completeness only. That CR predictive model is intended for the case of uniform corrosion and was derived for 75% relative humidity and 20^{o}C temperature conditions. In the case of localized corrosion however the corrosion product build-up is expected to accumulate faster on the anode resulting in earlier reduction in corrosion rate. The latter may be considered another mitigating factor (similar to that of X_{crit}) associated with corrosion localization. Nevertheless experimental evidence is yet to be established to confirm that behavior. In the absence of such an evidence the currently available predictive model for uniform corrosion were applied to all cases considered here. The time-variant CR model is expressed in equation 5.19 in terms of corrosion current density [Vu et al. 2000].

$$\mathrm{icorr_t} = 0.85\ \mathrm{icorr_{to}}(\mathrm{t/Year})^{-0.29} \tag{5.19}$$

where $\mathrm{icorr_t}$ is the corrosion current density in μA/cm^2 at time (t ≥1) in years and $\mathrm{icorr_{to}}$ is the initial corrosion current density in μA/cm^2 averaged over the first year. The initial current densities for the cases considered here were calculated according to the procedure described next and assumed to be constant over the first year period after corrosion initiation.

5.3.2 Procedure

The system considered for simulation is shown in figures 5.1 with dimensions given in table 5.3. In the case of 100% macrocell current scenario of localized corrosion, the central anode region is considered to support only anodic reaction which is iron dissolution. The rest of rebar is treated as supporting only cathodic reaction which is oxygen reduction.

Anodic reaction: $Fe \longrightarrow Fe^{2+} + 2e$ (5.20)

Cathodic reaction: $O_2+2H_2O+4e \longrightarrow OH^-$ (5.21)

In the case of uniform corrosion and 0% macrocell current scenario of localized corrosion, anodic and cathodic reactions were assumed to be taking place on the same corroding region of rebar.

The anodic reaction was assumed to be operating under activation polarization control whereas the cathodic reaction being under mixed activation-concentration polarization control. Both anodic and cathodic reactions were assumed to follow the Butler-Volmer kinetics. Both reactions were considered to be sufficiently removed from their equilibrium potentials to neglect the reverse reactions of those in equations 5.20 and 5.21. The anodic and cathodic current densities on rebar surface (i_a and i_c, respectively) were determined by the following current-potential relationships:

$$i_a = i_{oa} e^{\frac{2.3}{b_a}(E_s - E_{oa})} \quad (5.22)$$

and

$$i_c = i_{oc} \frac{C_S}{C_o} e^{\frac{2.3}{b_c}(E_{oc} - E_S)} \quad (5.23)$$

where C_s and E_s are oxygen concentration and steel potential on the rebar surface, respectively. The other calculating parameters and their values are given in table 5.5. Those parameters were selected to reflect generic concrete electrochemical properties with no significant impact anticipated of their variability on the general trends. The oxygen surface concentration was considered constant on the external concrete surface. Concrete is treated as a medium of uniform resistivity and oxygen is considered transporting through concrete only by diffusion with a uniform effective diffusion coefficient (D) following Fick's first law (equation 5.24). The oxygen diffusion was assumed to be radial only with no oxygen transport is allowed through cylinder ends.

$$J = -D\nabla C \quad (5.24)$$

where J is oxygen flux. The oxygen flux on rebar surface according to Faraday's law is equivalent to (i_c/nF) where n=4 from equation 5.21 and F is Faraday's constant.

In view of the above assumptions it follows that the electrical potential with respect to steel rebar and the oxygen concentration in the bulk concrete should comply with Laplace's equation to satisfy conservation of charge and mass at steady state condition [Sagüés et al. 1992]:

$$\nabla^2 E=0 \qquad (5.25)$$

$$\nabla^2 C=0 \qquad (5.26)$$

Solving the partial differential equations 5.25 and 5.26 in cylindrical coordinates may be achieved using FE analysis considering the axisymmetry described in figure 5.2. The boundary conditions were obtained by simultaneously solving equations 5.22, 5.23 and 5.24 for anodic and cathodic current as well as oxygen concentration, respectively on rebar surface. The solution yielded the electrical potential E and oxygen concentration *C* at all positions in concrete. The electrical potentials of steel with respect to concrete are the negative of the calculated potentials at concrete points in contact with the rebar. The corresponding values of electrical current density and oxygen flux on rebar surface were obtained by taking the normal derivative of E and *C* on the rebar surface. The total corrosion current was computed by integrating the iron

dissolution current density over the anode area or alternatively by integrating the equivalent cathodic current density over the rebar cathodic regions.

Table 5.5 Calculation electrochemical parameters

Model Parameters [Sagüés et al. 2013, Kranc et al.1992 & 1993]	Values
Unpolarized cathode potential, E_{oc} (V, SCE)	0
Cathodic exchange current density, i_{oc} (A/m^2)	2×10^{-4}
Cathodic Tafel slope, b_c (V)	0.16
Unpolarized anodic potential, E_{oa} (V, SCE)	-0.78
Anodic exchange current density, i_{oa} (A/m^2)	3×10^{-4}
Anodic Tafel slope, b_a (V)	0.06
Concrete Resistivity ,ρ_c (Ohm.m)	100
Oxygen concentration at external concrete surface, *C*o (mol/m^3)	0.25
Effective oxygen diffusion coefficient, D (m^2/s)	1×10^{-9}

5.3.3 Results

The electrochemical FE simulation results of electrical potentials and resulting current across concrete cover are given in appendix B (figures B.16 and B.17). The figures shown in appendix B are only intended to illustrate the general trends. The FE analysis results of the 0 % macrocell current scenario for cases of localized corrosion exhibited similar general trends to those of uniform corrosion shown in appendix B but with electrochemical reactions only limited to the corroded central regions.

Figure 5.23 shows the electrical potential distribution along the test cylinder length for the localized corrosion (C/L=1) when affected by 100% macrocell current and for the uniform corrosion. The potential values represent readings taken both on the concrete external surface and directly over the rebar. The case of uniform corrosion did not exhibit any difference between the surface-measured and on-rebar measured potentials. That effect is presumably due to the absence of macrocell action, which would otherwise cause voltage (IR) drop due to current flowing through concrete resistance [Kranc et al. 1992]. Conversely, the case of localized corrosion exhibited an IR drop resulting in a difference between the potential values calculated on concrete surface and those calculated on rebar [Gulikers 2006]. The potential on the concrete surface at the center of anode was less negative than the true potential on the rebar for all C/L ratios. However, the potentials on the concrete surface over the passive regions were more negative than the true values on the rebar. The IR drop over the passive regions for all C/L ratios tended to be in the order of 10 mV. On the other hand, the IR drop over the anode region increased as the ratio of C/L increased. The negative and positive changes in potential due to IR drop component may be explained by the direction of macrocell current flowing onto or discharging from the affected region. The values of IR drop at the center of anodic spots were 25, 40, 50, 62 and 70 mV for the ratios of C/L=1, 2, 3, 4 and 5, respectively. The increased sensitivity of the potential reading over the anode as anode size decreased may possibly be due to the associated increase in macrocell currents (table 5.6). On the other hand, the potential values for the localized corrosion cases when treated according to

the 0% macrocell current scenario showed no IR-drop between surface and rebar readings. The potential value for a ratio of C/L=1 was -689 mV (SCE) and became slightly more positive as the ratio of C/L increased.

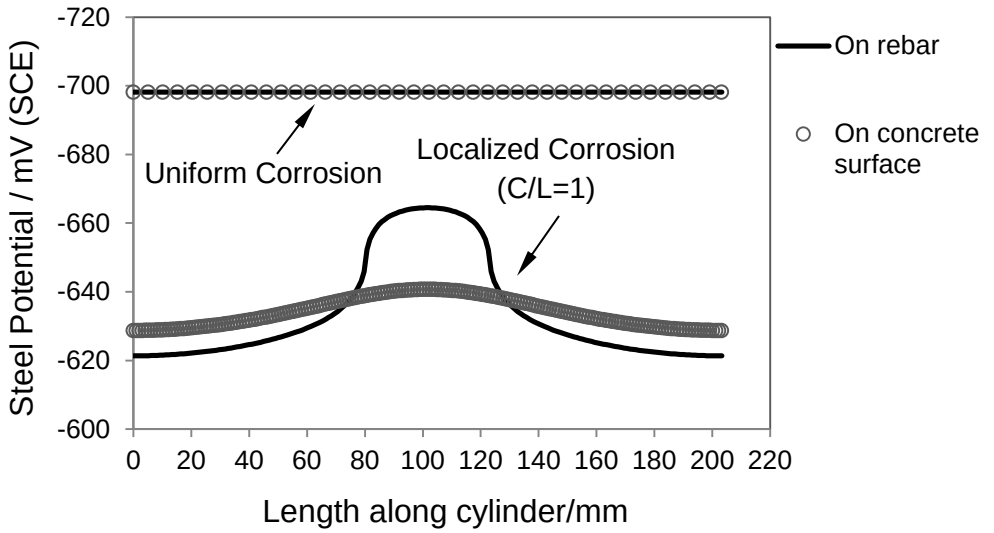

Figure 5.23 Distribution of steel potential along cylinder length directly on rebar and on concrete surface for the case of uniform corrosion and C/L=1. (100% macrocell current scenario)

Figure 5.24 shows the distribution of potential along cylinder close to rebar (IR-free values) for the uniform and localized corrosion cases considering the scenario of 100% macrocell current effect. The potentials on concrete surface over the anodes were comparable to the experimental values observed by the author on cracked RC pipes exposed to cyclic exposure to chloride solution [Busba et al. 2013b]. The potential values are also comparable to those obtained from a previous similar model for a corroding anodic spot in a nuclear containment steel liner [Sagüés et al. 2013]. Table 5.6 lists the total corrosion current for all modeled cases when treated according to both scenarios of 100%

macrocell current and 0% macrocell current. Those corrosion currents were comparable to values of previous experimental and modeling work [Kranc et al. 1992, COIN 2008, Raupach 1996, Redaelli et al. 2006, and Broomfield 2003].

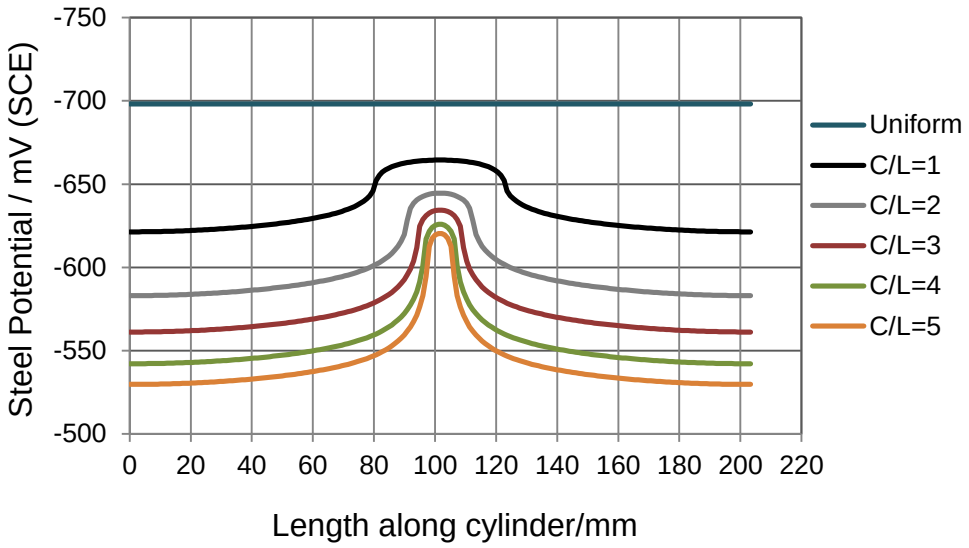

Figure 5.24 Distribution of steel potential along cylinder length directly on rebar for the case of uniform corrosion and C/L=1, 2, 3, 4 and 5. (100% macrocell current scenario)

The corrosion currents and potential values for the 100% macrocell current scenario in table 5.6 and figure 5.24, respectively were illustrated in figure 5.25 in terms of E-log I diagram (Evans diagram). The plotted potential values were those taken on the center of anode and at the edge of cathode corresponding to distances of 101.65 and 0 mm on the x-axis, respectively on figure 5.24. An approximate schematic representation of the cathodic and anodic reactions was shown to illustrate the effect of surface area of electrode on reaction kinetics [Jones 1996].

Table 5.6 Summary of calculated corrosion currents for the 0 and 100% macrocell current scenarios

Type of Corrosion	(C/L)	Corroding to Passive Area Ratio	Corrosion Current (I_{corr}) / µA	
			100% Macrocell Current	0% Macrocell Current
Uniform	0.2	1	-	62.18
Localized	1	0.27	53.22	18.59
	2	0.12	58.24	11.82
	3	0.08	58.35	9.28
	4	0.06	59.05	7.89
	5	0.04	59.39	7.17

It may be inferred from figure 5.25 that increasing the corroding to passive area ratio tended to cause the role of concentration polarization to increase. An independent analytical verification confirmed that the corrosion current density for the case of uniform corrosion is approaching the diffusional limitation condition with a value of ~ 7 µm/Y. The corresponding corrosion current densities based on the FE model predictions for the two scenarios are plotted in figure 5.26 versus the ratios of corroding to passive area. The trends of the FE model predictions in figure 5.26 seem to be in a good agreement with the findings of a recent state-of-the-art report [COIN 2008]. That study generally concluded that macrocell current effect (if present) can cause corrosion rate increases by 10% in dry concrete and by more than 90% in wet concrete. Figure 5.26 shows experimental values of corrosion current densities to test the validity of the FE model. Data previously obtained by the author [Busba et al. 2013b] from cracked RC pipe specimens showed a reasonable agreement with the scenario assuming macrocell current being present. The corrosion rates from that RC pipe study

were derived from accelerated cyclic exposure to chloride environment. Therefore the resulting corrosion rates may be more severe than those expected in service. Schissel et al studied the macrocell corrosion behavior of steel in cracked concrete under simulated service conditions of 80% relative humidity for comparable concrete cover depth [Schissel et al. 1997]. The findings of that study are shown in figure 5.26 to be ranging between the two model scenarios. Therefore, it may reasonably be assumed that actual variations in macrocell current can cause it to fall anywhere between the two considered scenarios. Those variations are expected to occur due to environmental conditions, concrete cover and concrete quality.

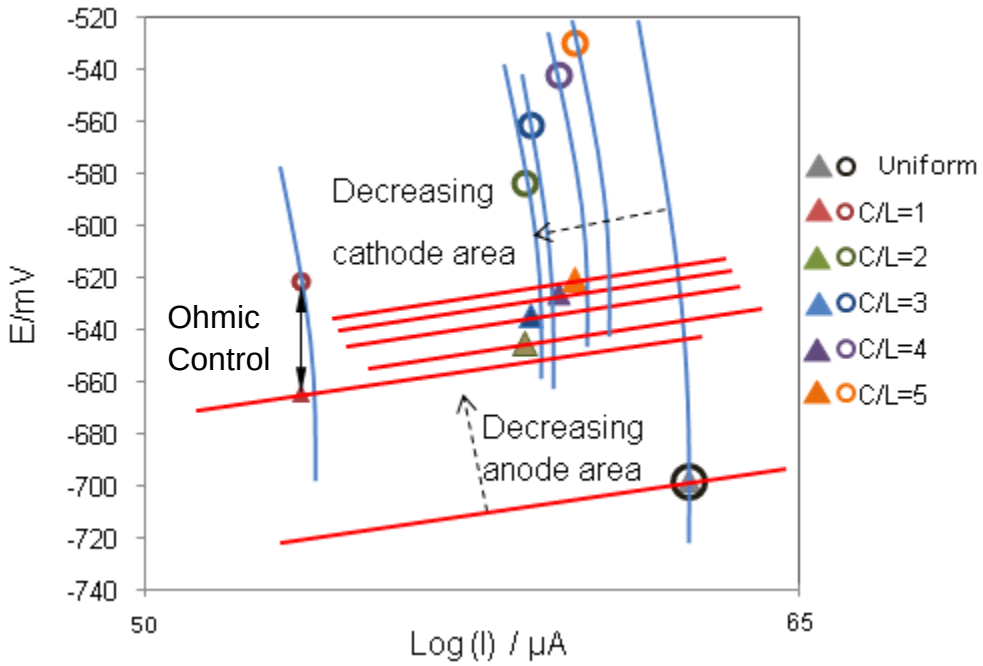

Figure 5.25 Schematic representation of the effect of corroding to passive area ratio on corrosion currents and potentials (on rebar surface) for the modeled cases using the 100% macrocell current scenario. The triangular and circular symbols indicate potentials at center of anodes and at edge of cathodes plotted versus the corresponding corrosion currents, respectively.

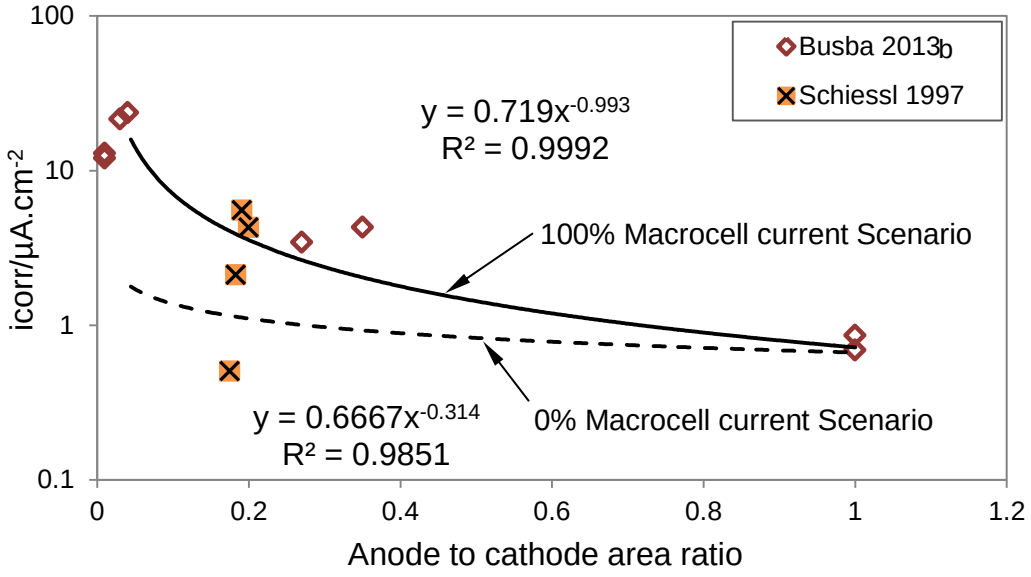

Figure 5.26 Model predictions showing corrosion current density increase with decrease in the corroding to passive surface area ratio for 0 and 100% macrocell current scenarios.

5.4 Overall Effect of the Influence of Corrosion Localization on Time to Concrete Cover Cracking

The corrosion rates (CR) in terms of corrosion penetration depth per year were calculated for the two 0% and 100% macrocell current scenarios using Faraday's law. Figure 5.27 shows the increase in CR for the two scenarios and the increase in X_{crit} per the proposed equation (equation 4.5) versus the degree of corrosion localization. The time to first corrosion-induced cracking (T_{cr}) was calculated by dividing the critical penetration (X_{crit}) by the corrosion rate (from the two scenarios) assuming that the corrosion rate is not varying with time. Figure 5.28 shows the results of time to cracking from both scenarios for various degrees of corrosion localization. The envelope between the two dashed lines represents the range of times to cracking expected corresponding to the range of 0 to 100% macrocell currents at various ratios of C/L.

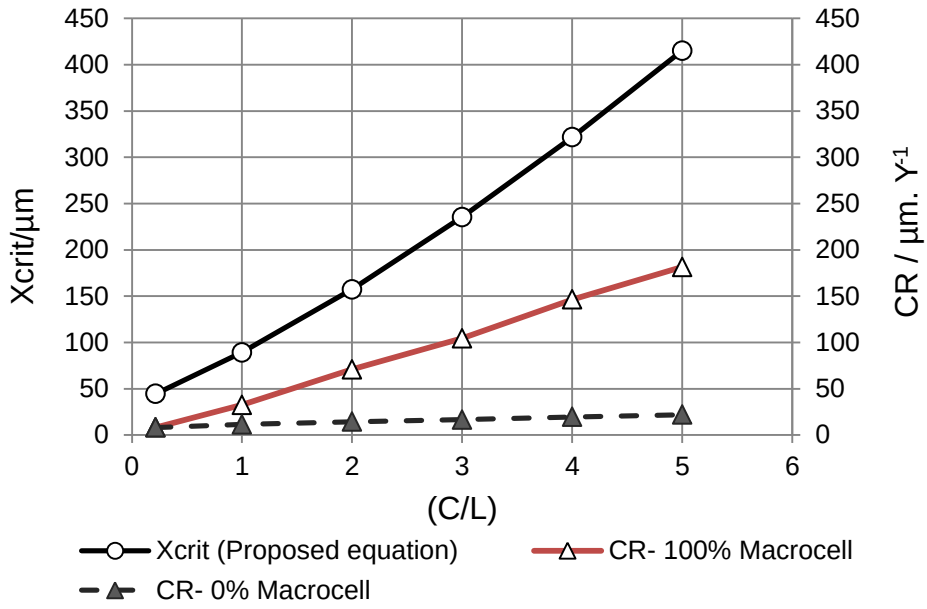

Figure 5.27 Critical penetrations (X_{crit}) per the proposed equation and the time-invariant corrosion rates (0 and 100% macrocell effects) as a function of corrosion localization

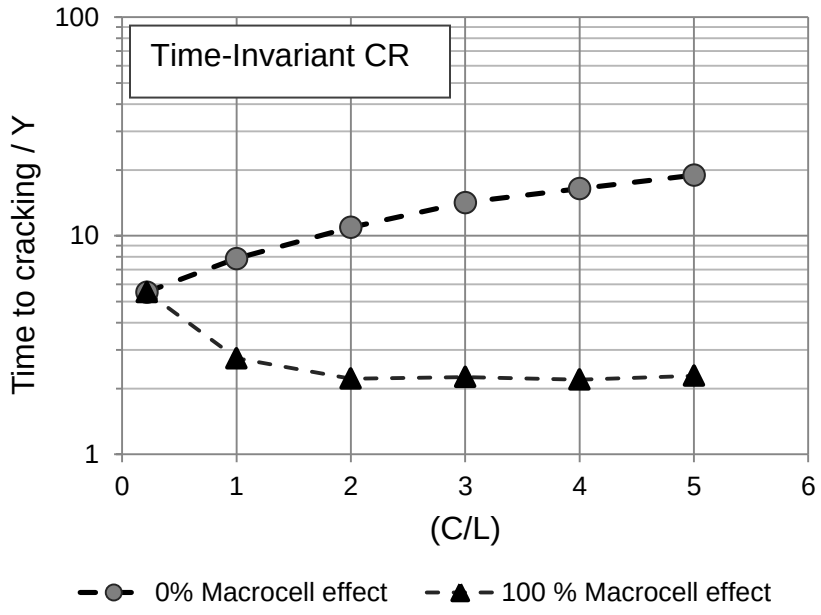

Figure 5.28 Predicted time to cracking as a function of corrosion localization due to time-invariant corrosion rates calculated for 0 and 100% macrocell effects

The time-variant corrosion rates were estimated based on equation 5.19 for the two considered macrocell current scenarios for various degrees of corrosion localization. Figure 5.29 shows the results of time-variant CR corresponding to (a) 0% and (b) 100% macrocell effects. The predicted times to first cracking for various ratios of C/L based on time-variant corrosion rates were calculated using equations 5.27 and 5.28.

$$X_{crit} = \sum_{t=0}^{Tcr} CR(t)\,\Delta t \tag{5.27}$$

$$\text{Time to Cracking } (Tcr) = n\,\Delta t \tag{5.28}$$

where CR(t) is the instantaneous corrosion rate from figure 5.29, Δt is a constant time interval in years and n is the number of time intervals up to the onset of cracking.

The results are shown in figure 5.30. The average time to first cracking may be increased in highly localized corrosion cases by up to twice the time needed for the cover cracking of a uniformly corroding reinforcement.

As indicated earlier, equation 5.19 had been developed for the case of uniform corrosion and was used for localized corrosion cases in the absence of a relevant predictive time-variant CR model in the literature for localized corrosion. There is also an increasing trend of using high quality concrete and increased concrete cover thickness in construction industry [Subramaniam et al. 2010].

Therefore, the macrocell current effect would be expected to be significantly reduced. Considering the latter along with the expected much faster reduced CR with time for localized corrosion cases, the corrosion localization may be regarded as a desirable mitigating factor for extending time to cracking.

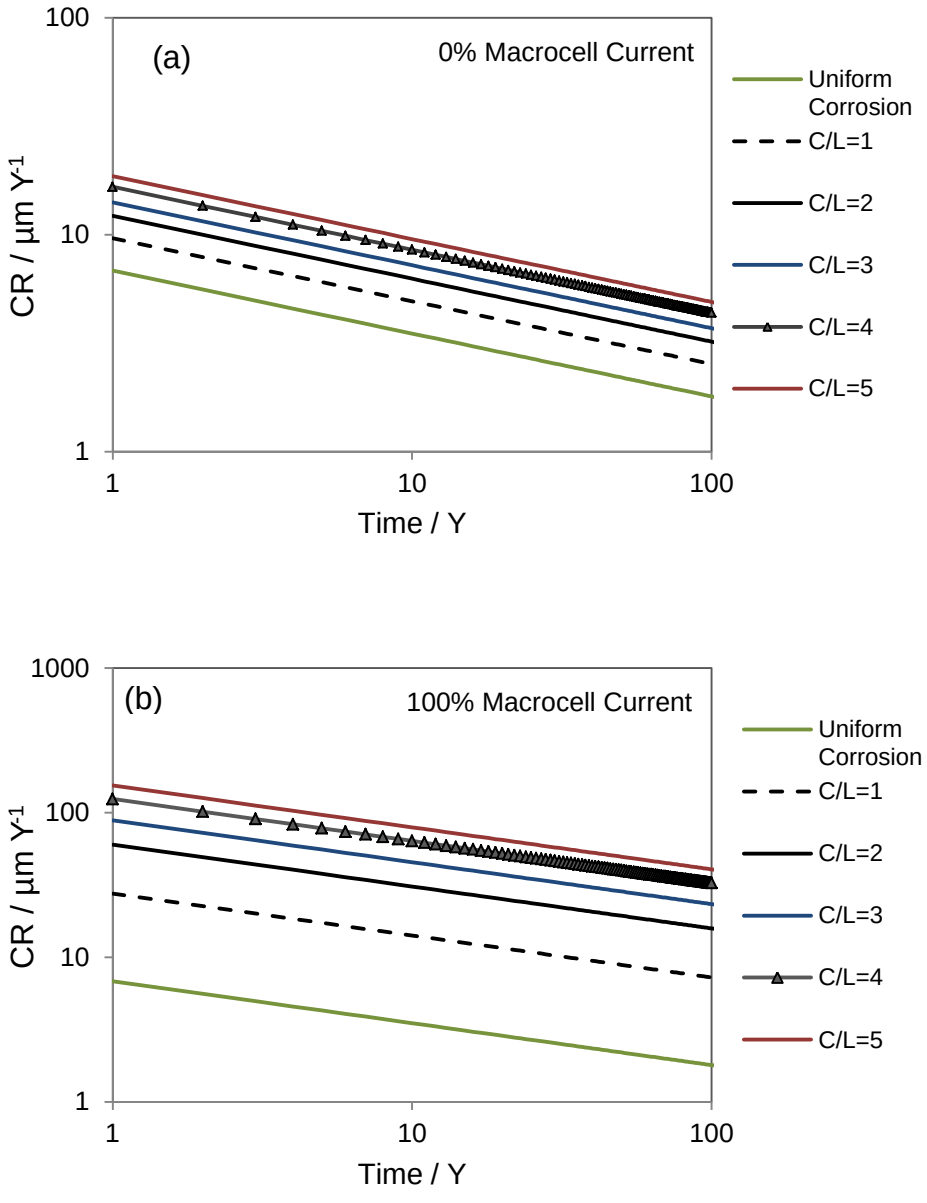

Figure 5.29 Time-variant corrosion rates calculated based on equation 5.19 for (a) 0% macrocell effect and (b) 100% macrocell effect

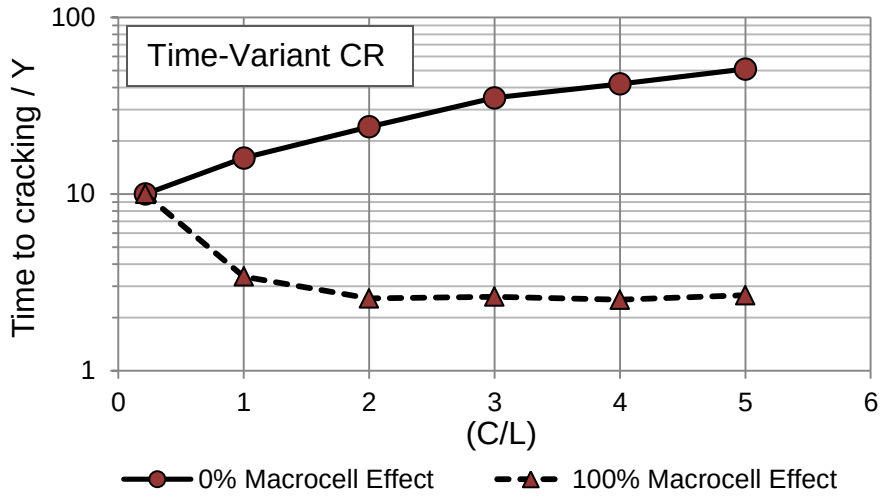

Figure 5.30 Predicted time to cracking as a function of corrosion localization due to time-variant corrosion rates calculated for 0 and 100% macrocell effects

The previous analysis thus far considered that the only reaction taking place on the corroding segment is the anodic reaction for the case of 100% macrocell effect. In the following, examination of the possible case where the corroding zone supports both anodic and cathodic reactions was undertaken to verify the validity of the findings obtained earlier. The latter case imply that both macrocell and microcell current effects are present. The problem was also solved numerically using the same electrochemical parameters in table 5.5 for the cathodic and anodic reactions. Figure 5.31 shows a comparison of times to cracking for the case where the corroding zone supports only the anodic reaction with those for the case where the corroding zone supports both cathodic and anodic reactions under time-invariant corrosion rate conditions. The comparison indicated that both cases exhibited the general decreasing trend of time to cracking as corrosion becomes more localized in the presence of macrocell effect. The results in the case where the corroding zone supported both anodic

and cathodic reactions yielded slightly less values of time to cracking by not more than ~ 14% (for C/L=1) compared to the case where there is only anodic reaction on the corroding zone. Therefore, the general trends obtained for the effect of corrosion localization on time to cracking remain essentially the same.

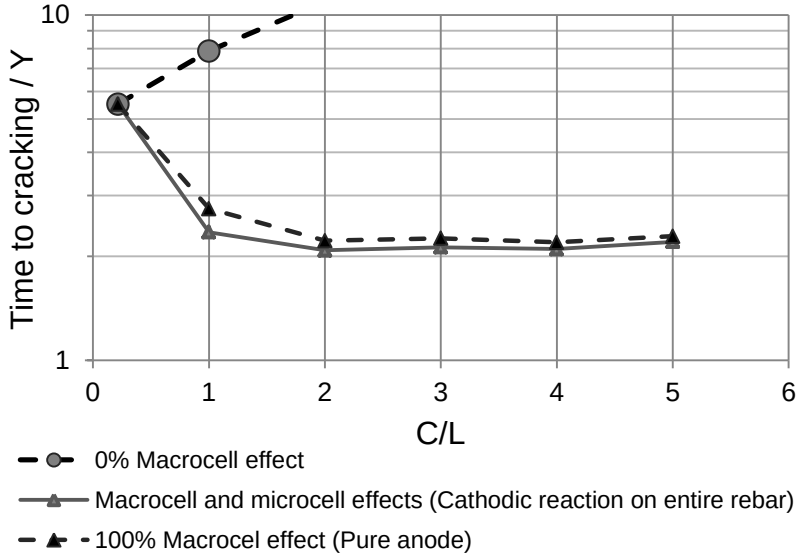

Figure 5.31 Comparison of times to cracking when considering both anodic and cathodic reactions on the corroding zone (cathodic reaction on entire rebar) with the case where there is only anodic reaction on the corroding zone (cathodic reaction only on passive regions). (Under time-invariant corrosion rate conditions)

6. CONCLUSIONS

The following conclusions were drawn based on the experimental and model findings.

(a) Electrochemical and direct examinations suggested that corrosion tends to be localized at the locations of rebar intersection with preexisting narrow (~ 0.5 mm) and wide (~ 2.5 mm) cover cracks in RC pipes exposed to a chloride-containing environment. Corrosion was observed to be more localized at the narrower crack intersections. Corrosion was shown to be uniformly distributed around rebar perimeter along the affected zone. The observed depths of corrosion penetration (radius loss) were found to be largest at the intersection and gradually decreasing further away on each side of the intersection.

(b) Rebar corrosion penetrations (X_{crit}) needed to cause a 0.1 mm-wide crack to appear on external concrete surface increased as corrosion became more localized. For the considered geometry, the amount of X_{crit} in the case of uniformly corroding rebar (C/L=0.2) was in the order of 30-50 µm and increased by up to ten folds (300 µm) for a locally corroding rebar (C/L=3).

(c) Concrete cover cracking was oriented parallel to the embedded rebar when corrosion was uniform. On the other hand, Cover cracking tended to be circumferentially oriented around reinforced cylinders in the case of localized corrosion. The latter case of transverse cracking with respect to rebar may be

expected to be manifested in practice by delamination. The observed crack orientations in both cases were theoretically substantiated by mechanical FE modeling.

(d) In corrosion-induced cracking experiments, uncertainties associated with gravimetric and Faradaic evaluations of mass loss can lead to incorrect estimations of critical penetrations. The use of deformed rebars in as-received surface condition tended to increase susceptibility to over cleaning due to the presence of mill-scale. Further, in accelerated corrosion experiments, Faradaic-based amounts of mass loss tended to be overestimated due to the reduced current efficiencies caused mainly by oxygen evolution reaction.

(e) An improved relationship was proposed for predicting X_{crit} as a function of geometric parameters and the degree of corrosion localization. The relationship was theoretically verified by an independent mechanical FE modeling of the underlying phenomena responsible for corrosion cracking.

(f) The mechanical FE model formulation permitted the simulation of both crack initiation and propagation and therefore was capable of accounting for the tension-softening behavior of concrete after cracking.

(g) The mechanical FE modeling suggested that the critical penetration is mainly controlled by the degree of corrosion localization and the capacity of generated cracks to accommodate the produced rust. The properties of concrete-rebar interface (ITZ) and type of oxides (rust) generated were also found to have a significant effect on X_{crit}. The amount of X_{crit} was found to be proportional to the ITZ thickness and inversely proportional to the relative

volume of the produced corrosion products. It was inferred that corrosion-induced cracks were only possible to become partially filled with rust. It was theorized that rust filling progresses as long as a crack continue to grow in a stable fashion up to a critical length. Beyond that critical length, unstable crack growth results in sudden full cover cracking without allowing further rust filling. The FE analysis has shown that the Increase in corrosion localization is associated with increase in radial displacement along the corrosion-affected zone with adjacent concrete regions slightly displaced. The latter is thought to provide an additional space to accommodate the produced rust.

(h) The mechanical FE model yielded values of critical pressure for initiation of cover cracking less than those predicted by some existing models that inaccurately assume linear elastic behavior of concrete cover. The FEM-derived critical pressure values, for the situations considered, ranged from 18 MPa for the case of uniform corrosion to ~ 45 MPa for the case of highly localized corrosion (C/L=5).

(i) Electrochemical FE modeling suggested that corrosion localization effect on aggravation of corrosion rate decreases as the macrocell effect decreases.

(j) The propagation periods were estimated based on existing time-variant corrosion rate prediction models and on the proposed X_{crit} relationship for various degrees of corrosion localization. The results indicated that corrosion localization may reasonably be considered a desirable mitigating factor for extending the propagation stage in cases where macrocell effect is not significant such as in high quality concrete with large depth of concrete cover.

The following may constitute the basis for further research suggested to resolve some of the related outstanding issues.

Experimental / numerical investigations of more sophisticated cases such as beams reinforced with multiple rebars with and without stirrups to examine:

- The effect of rebar spacing and the presence of localized corrosion spots on parallel rebars or along the same rebar with various spacing apart on defining cracking failure mode (delamination, cracking or spalling) and on X_{crit}.
- The possible mitigating effect of using non-metallic (e.g. CFRP) stirrups or concrete containing non-metallic fibers on confining the corrosion-induced stresses and hence increasing critical penetration of main rebars.
- The possible role of pre-existing narrow cracks with various crack widths in providing space for rust accommodation and for stress relaxation.
- The effect of partially corroded surface around rebar perimeter on X_{crit}.
- The extent to which stress concentrations introduced by the presence of rips on deformed rebars can accelerate corrosion-induced cracking or affect its orientation.
- Explore the factors responsible for controlling the growth of surface crack width as a result of corrosion of reinforcement such as the factor of rust-induced pressure on crack walls.
- The application of FEM modeling to evaluate resistance to corrosion-induced cracking of repair coating overlays using various candidate repair materials over a bridge deck (e.g. conventional high density overlay and silica fume overlays) versus full depth monolithic decks [Lindquist et al. 2005].

REFERENCES

Abdalla, H. M. and Karihaloo, B., L. (2004), “A Method for Constructing the Bilinear Tension Softening Diagram of Concrete Corresponding to its True Fracture Energy”, Magazine of Concrete Research, Vol. 56, No. 10, pp. 597-604

Al Harthy, A., Mullard, J., Stewart, M. (2007), Cracking in Concrete Due to Corrosion of Steel Reinforcement”, In: Concrete under Severe Conditions: Environment & Loading, CONSEC’07, Tours, France

Allan, M. L. and Cherry, B.W. (1989), “Mechanical Simulation of Corrosion-Induced Cracking”, Corrosion / 1989, Paper No.377, Houston, TX, USA

Alonso, C., Andrade, C. and Rodriguez, J. (1998), “Factors Controlling Cracking of Concrete Affected by Reinforcement Corrosion”, Materials and Structures, Vol. 31, No. 7, pp. 435 – 441

Al-Sulaimani, G. J., Kaleemullah, M., Basunbul, I. A. and Rasheeduzzafar (1990), “Influence of Corrosion and Cracking on Bond Behavior and Strength of Reinforced of Reinforced Concrete Members” ACI Structural Journal, Vol. 87, No. 2, pp. 220-231

Andrade, C. and Gonzalez, J. A. (1978), “ Quantitative measurements of corrosion rate of reinforcing steels embedded in concrete using polarization resistance measurements”, Werkstoffe und Korrosion, Vol. 29, No. 8, pp. 515-519

Angst, U. M., Elsener, B., Larsen, C. K. and Vennesland, Ø. (2011a), “Chloride Induced Reinforcement Corrosion: Electrochemical Monitoring of Initiation Stage and Chloride Threshold Values”, Corrosion Science, Vol. 53, No.4, pp. 1451-1464

Angst, U., RØnnquist, A., Elsener, B., Larsen, C. K. and Vennesland, Ø. (2011b), “Probabilistic Considerations on the Effects of Specimen Size on the Critical Chloride Content in Reinforced Concrete”, Corrosion Science, Vol 53, No.1, pp.177-187

ASTM A615/A615M-03a (2003), “Standard Specification for Deformed and Plain Billet-Steel Bars for Concrete Reinforcement”, American Society for Testing and Materials, Philadelphia, PA, USA

ASTM C33 – 03 (2003), “Standard Specification for Concrete Aggregate”, American Society for Testing and Materials, Philadelphia, PA, USA

ASTM C39 – 03 (2003), “Standard Test Method for Compressive Strength of Cylindrical Concrete Specimens”, American Society for Testing and Materials, Philadelphia, PA, USA

ASTM C496 – 11 (2011), “Standard Test Method for Splitting Tensile Strength of Cylindrical Concrete Specimens”, American Society for Testing and Materials, Philadelphia, PA, USA

ASTM C76-11, (2011), “Standard Specification for Reinforced Concrete Culvert, Storm Drain, and Sewer Pipe”, American Society for Testing and Materials, West Conshohocken, Philadelphia, PA, USA

ASTM C876 – 09, (2009), “Standard Test Method for Half-Cell Potentials of Uncoated Reinforcing Steel in Concrete”, American Society for Testing and Materials, West Conshohocken, Philadelphia, PA, USA

ASTM E337 – 01 (1984), “Standard Test Method for Measuring Humidity with a Psychrometer (the Measurement of Wet- and Dry-Bulb Temperatures”, American Society for Testing and Materials, Philadelphia, PA, USA

ASTM G1 – 03 (2003), “Standard Practice for Preparing, Cleaning, and Evaluating Corrosion Test Specimens”, American Society for Testing and Materials, Philadelphia, PA, USA

ASTM G102 – 89, (1989), “Calculation of Corrosion Rates and Related Information from Electrochemical Measurements”, American Society for Testing and Materials, West Conshohocken, Philadelphia, PA, USA

Badwe, S., Raja, K. S. and Misra, M. (2006), “A study of Corrosion Behavior of Ni-20 Cr-13 Mo-3W Alloy under Hygroscopic Salt Deposits on Hot Surface”, Electrochimica Acta, Vol. 51, No.26, pp.5836-5844

Bains, H. and Sagüés, A. A. (1989), “ Durability of Conductive Polymer for Cathodic Protection of Rebars in Concrete Piling”, Final Report to Florida Dept. of Transportation, Project No. 99700-7424-119, Tallahassee, FL, USA

Balafas, I. and Burgoyne, C. J. (2011), “Modeling the Structural Effects of Rust in Concrete Cover”, Journal of Engineering Mechanics, ASCE, Vol. 137, No.3, 175 - 185

Bazant, Z. (1979), “Physical model for Steel Corrosion in Concrete Sea Structures – Application, J Struct Div, Vol. 105, No. 6, pp. 1155-1166

Bennitz, A., Grip, N., Schmidt, J. (2011), “Thick-walled Cylinder Theory Applied to Conical Wedge Anchorage”, Meccanica, Vol. 4, No. 5, pp. 959-977

Bhargava, K., Ghosh, A., Mori, Y., Ramanujam, S. (2006), “Model for Cover Cracking Due to Rebar Corrosion in RC Structures”, Eng Struct, Vol. 28, No.8, pp. 1093-1109

Bohni, H. (2005), “Corrosion in Reinforced Concrete Structures”, CRC Press, Boca Raton, USA

Broomfield, J. P. (2003), “Corrosion of Steel in Concrete”, London, England, Taylor & Francis (Chalmers e-Library), 240 pp.

Busba, E. and Sagüés, A. A. (2013a), “Critical Localized Corrosion Penetration of Steel Reinforcement for Concrete Cover Cracking”, Corrosion, Paper No.2747, Houston, TX, USA

Busba, E. and Sagüés, A. A. (2013b), “Localized Corrosion of Embedded Steel in Cracked Reinforced Concrete Pipes”, Corrosion, Vol. 69, No. 4, pp.403-416

Busba, E. R., Sagüés, A. A. and Mullins, G. (2011), “Reinforced Concrete Pipe Cracks- Acceptance Criteria”, Final Report to Florida Dept. of Transportation, Contract No. BDK84 977-06. (Accessed on-line: Jan. 19, 2012) (www.dot.state.fl.us/research-center)

Castorena, J., Almeraya-Calderon, F., Velasquez, J, Gaona-Tiburcio, C., Cardenas, A, Barrios-Durstewitz, C. (2008), “ Modeling the Time-to-Corrosion Cracking of Reinforced Concrete Structures by Finite Element, Corrosion, Vol. 64, No. 7, pp. 600-606

Castro, P., Sagüés, A. A., Moreno, E. I., Maldonado, L. and Genesca, J. (1996), “Characterization of Activated Titanium Solid Reference Electrodes for Corrosion Testing of Steel in Concrete”, Corrosion, Vol. 52, No. 8, pp. 609-617

CEB - Comité Euro-International d'Beton (1985), “Draft CEB Guide to Durable Concrete Structures”, Bulletin d'Information, No.166, CEB, Lausanne, Switzerland

CEB-FIP Model Code (1990), Bulletin d’information No. 213/214. Comité Euro-International du Beton, Lausanne, Switzerland

Chen, C. M. and Theus, G. J. (1982), “Chemistry of Corrosion-Producing Salts in Light Water Reactors”, Report NP-2298, Electric power Research Institute, Palo Alto, CA, USA

Chen, D., Mahadevan, S. (2008), “Chloride-induced reinforcement corrosion and concrete cracking simulation”, Cement and Concrete Composites, Vol. 30, No. 3, pp. 227-238

Chernin, L., Val, D. V. and Volokh, K.Y. (2010), “Analytical Modeling of Concrete Cover Cracking Caused by Corrosion of Reinforcement”, Materials and Structures, Vol. 43, No. 4, pp. 543-556

Chernin, L. and Val, D. (2011), “Prediction of corrosion-induced cover cracking in reinforced concrete structures”, Construction and building Materials, Vol. 25, No. 4, pp.1854-1869

Comsol Multiphysics user’s guide (2008), version 3.5 a, Comsol AB, (Accessed online: June 5, 2013), http://math.nju.edu.cn/help/mathhpc/doc/comsol/guide.pdf

Concrete Innovation Center (COIN) (2008), “Modelling of Reinforcement Corrosion in Concrete – State of the Art”, SINTEF Building and Infrastructure, Report no. 7, ISBN: 978-82-536-1081-8 (pdf), http://www.coinweb.no

Crank, J. (1975), “The Mathematics of Diffusion”, 2nd edition, Oxford University Press, USA

Darwin, D., Browning, J. and O’Reilly, M. “Multiple Corrosion-Protection Systems for Reinforced Concrete Bridge Components” (2011), Federal Highway Administration report no. FHWA-HRT-11-060, University of Kansas Center for Research, Inc., SM Report No. 101, Lawrence, KS. (Accessed online: October 9, 2012) (http://www.iri.ku.edu/projects/corrosion/SM101.pdf)

El Maaddawy, T. and Soudki, K., (2003), “Effectiveness of Impressed Current Technique to Simulate Corrosion of Steel Reinforcement in Concrete”, Journal of Materials in Civil Engineering, Vol. 15, No. 1, pp. 41 – 47

El Maaddawy, T. and Soudki, K. (2007), “A Model for Prediction of Time from Corrosion Initiation to Corrosion Cracking”, Cement and Concrete Composites, Vol. 29, No. 3, pp. 168 – 175

Enevoldsen, J. N. and Hansson, C. M. (1994), “Binding of Chloride in Mortar Containing Admixed or Penetrated Chlorides”, Cement and Concrete Research, Vol. 24, No. 8, pp. 1525-1533

FM5-516 (2009), “Florida Method of Test for Determining Low-Level of Chlorides in Concrete and Raw Materials”, Florida Dept. of Transportation, Tallahassee, FL, USA

Fox, T. J., Randall, C. D. and Gross, D. H. (1993), “Steel Pickling: A profile”, Draft report to US Environmental Protection Agency, EPA Contract No. 68-D1-0143, Office of Air Quality Planning and Standards, Cost and Economic Impact Section, Research Triangle Park, NC, USA

Gellings, P. J. (2005), “Introduction to Corrosion Prevention and Control”, Edition 2005, Enschede, the Netherlands

Ghods, P. Isgor, O. B., McRae, G. A., Li, J. and Gu, G. P. (2011), “Microscopic Investigation of Mill Scale and Its Proposed Effect on the Variability of Chloride-Induced Depassivation of Carbon Steel Rebar”, Corrosion Science, Vol. 53, No.3, pp. 946-954

Ghods, P., Isgor, O. B., McRae, G. and Miller, T. (2009), “The Effect of Concrete Pore Solution Composition on the Quality of Passive Oxide Films on Black Steel Reinforcement”, Cement and Concrete Research, Vol. 31, No. 1, pp. 2-11

Glass, G. K. and Buenfeld, N. R. (1997), “The Presentation of the Chloride Threshold Level for Corrosion of Steel in Concrete”, Corrosion Science, Vol. 39, No. 5 pp. 1001-1013

Glass, G. and Buenfeld, N. R. (2000), “Chloride-Induced Corrosion of Steel in Concrete, Progress in Structural Engineering Materials, Vol. 2, No.4, pp. 448-458

Gonzalez, J. A., Andrade, C., Alonso, C. and Feliu, S. (1995), “Comparison of Rates of general Corrosion and Maximum Pitting penetration on Concrete Embedded Steel Reinforcement”, Cement and Concrete Composites, Vol. 25, No. 2, pp. 257 – 264

Gonzalez, J. A., Miranda, J. M., Birbilis, N. and Feliu, S. (2005), “Electrochemical Techniques for Studying Corrosion of Reinforcing Steel: Limitations and Advantages”, Corrosion, Vol. 61, No. 1, pp.37-50.

Gulikers, J and Raupach, M. (2006), “Numerical Models for the Propagation period of Reinforcement Corrosion”, Materials and Corrosion, Vol. 57, No. 8, pp. 618-627

Hanjari, K. (2010). “Structural Behavior of Deteriorated Concrete Structures” Ph.D. Thesis, Department of Civil and Environmental Engineering, Chalmers University of Technology, Gothenburg, Sweden

Hansson, C., Poursaee, A. and Jaffer, S. (2007), “Corrosion of Reinforcing Bars in Concrete”, Portland Cement Association, PCA R&D Serial No. 3013, Skokie, Illinois, (http://www.cement.org)

Hillerborg, A., Modeer, M., Petersson, P-E. (1976), “Analysis of Crack Formation and Crack Growth in Concrete by Means of Fracture Mechanics and Finite Elements”, Cement and Concrete Research, Vol. 6, No. 6, pp. 773-782

Hu, O. E., Teng, S., lrawan, P. and Cheong, H. K. (2003), “Prediction of Failure Load of Reinforced High Strength Concrete Beams by Non-Linear Finite Element Analysis”, 28th Conference on “Our World in Concrete & Structures”: 28 – 29th August 2003, Singapore, On-line article is available from Singapore Concrete Institute at: http://cipremier.com/100028038 (Last accessed on July 11, 2013)

Hussain, R., Ishida, T. and Wisam, M. (2012), “Oxygen Transport and Corrosion of Steel in Concrete under Varying Concrete Cover, W/C and Moisture”, ACI Materials Journal, Vol. 109, No. 1, pp. 3-10

Jaffer, S. and Hansson, C. (2009), “Chloride-Induced Corrosion Products of Steel in Cracked Concrete Subjected to Different Loading Conditions”, Cement and Concrete Research, Vol. 39, No. 2, pp. 116 -125

Jamali, A., Angest, U., Adey, B. and Elsener, B. (2013), “Modeling of Corrosion-Induced Concrete Cover Cracking: A Critical Analysis”, Construction and Building Materials, Vol. 42, No. 12, pp.225-237

Jang, B. (2010), “Failure Analysis of Reinforced Concrete Due to Pitting Corrosion of Reinforcing Bar”, Concrete Under Severe Conditions – Environment and Loading, Castro-Borges et al., Vol. 1, Taylor & Francis Group, London, ISBN 978-0-415-59316-8

Jendele, L., Cervenka, J., Saoma, V. and Pukl, R. (2001), "On the Choice between Discrete or Smeared Approach in Practical Structural FE Analyses of Concrete Structures", the Fourth International Conference on Analysis of Discontinuous Deformation, 6-8th June, Glasgow, Scotland UK

Johns, D. A. (1996), “Principles and Prevention of Corrosion”, 2nd Edition, Prentice Hall, Inc. Upper Saddle River, NJ, USA

Kranc, S.C. and Sagüés, A. A. (1992), “Computation of Corrosion Macrocell Distribution and Electrochemical Impedance of Reinforcing Steel in Concrete”, American Society for Testing and Materials (ASTM), Philadelphia, Pennsylvania, USA, Standard technical publication 1154, pp. 95-112,

Kranc, S.C. and Sagüés, A. A. (1993), “Calculation of Extended Counter Electrode Polarization Effects on the Electrochemical Impedance Response of Steel in Concrete”, American Society for Testing and Materials (ASTM), Philadelphia, PA, USA, Standard technical publication 1188, pp. 365-383,

Lau, K. and Sagüés, A. A. (2010a), “Approach to Modeling Corrosion Progression of Epoxy Coated Rebar in Structures with Cracked Concrete”, Corrosion / 2010, Paper No.10128, Houston, TX, USA

Lau, K., A. (2010b), “Corrosion of Epoxy-Coated Reinforcement in Marine Bridges with Locally deficient Concrete” Ph.D. Dissertation, Department of Civil & Environmental Engineering, University of South Florida, Tampa, Florida, USA

Lazari, P., Gerard, B. (2000), “Mechanical Behavior of Corrosion Products formed at the Steel Concrete Interface- Testing and Modeling”, Conditions Monitoring of Materials and Structures. In: Proceedings EM2000, 14th Engineering Mechanics Conference, ASCE, Austin, TX, USA

LePatner, B. (2012), Save Our Bridges, http://www.saveourbridges.com, last accessed on: August, 22nd, 2013

Lee, S. K. (2012), “Current State of Bridge deterioration in the U.S.- part 1”, Materials performance, Vol.51, No. 1, pp. 62-67

Lee, S. K. (2012), “Current State of Bridge deterioration in the U.S.- part 2”, Materials performance, Vol.51, No. 2, pp. 40-45

Li, L. and Sagüés, A. A. (2001), “Metallurgical Effects on Chloride Ion Corrosion Threshold of Steel in Concrete”, Final Report to Florida Dept. of Transportation, Contract No. BA 501, Tallahassee, Fl, USA

Li, L. and Sagüés, A. A. (2004), “Chloride Corrosion Threshold of Reinforcing Steel in Alkaline Solutions – Effect of Specimen Size”, Corrosion, Vol. 60, No. 2, pp. 195-202

Lindquist, W. D., Darwin, D. and Browning, J. P. (2005), “Cracking and Chloride Contents in Reinforced Concrete Bridge Decks”, Report to Kansas department of transportation, Report no. K-TRAN: KU-01-9, Bureau of Materials and Research, Topeka, KN, USA

Liu Y. and Weyers R. (1998), “Modeling the Time to corrosion Cracking in Chloride Contaminated Reinforced Concrete Structures”, ACI materials J., Vol. 95, No. 6, pp. 675 – 681

Lu, C., Jin, W. and Liu, R. (2011), “Reinforcement Corrosion-Induced Cover Cracking and Its Time Prediction for Reinforced Concrete Structures”, Corrosion Science, Vol. 53, No. 4, pp. 1337-1347

Luc, D. (2010), “Numerical Analysis of Degradation of Concrete Structures Subjected to a Chloride-Induced Corrosion Environment”, Ph.D. Thesis, Department of Civil and Environmental Engineering, Yonsei University, Seoul, South Korea

Maekawa, K., Pimanmas, A. and Okamura, H. (2003), “Nonlinear Mechanics of Reinforced Concrete”, New York and London, Spon Press, Taylor & Francis Group

Mansfeld, F. (1988), “Don’t Be Afraid of Electrochemical Techniques – But use them with care!” Corrosion, Vol. 44, No.12, pp. 856-868

Marcotte, T.D. (2001), “Characterization of Chloride-Induced Corrosion Products that Form in Steel-Reinforced Cementitious Materials”, Ph.D. Thesis in Mechanical Engineering, University of Waterloo: Waterloo, Canada.

Marshall, O. S., Mclnerney, M. K., Morefield, S. and Hock, V. F. (2007), “Electro-Osmotic Pulse Technology: A Novel Solution to Severe Water Intrusion Problems in Earth Covered Magazines”, Corrosion, Paper No.7232, Houston, TX, USA

Materials Property Data, MatWeb LLC, http://www.matWeb.com, last accessed on: September, 9th, 2013

Melchers, R. E. and Li, C. Q. (2009), “Reinforcement Corrosion Initiation and Activation Times in Concrete Structures Exposed to Severe marine Environments”, Cement and Concrete Research, Vol. 39, No.11, pp. 1068-1076

Mindess, S., Young, J. and Darwin, D. (2003), “Concrete”,2nd edition, Prentice Hall, Pearson education, Inc., Upper Saddle, N.J., USA

Mohammed, T.U. and Hamada, H. (2003), “Corrosion of Steel Bars in Concrete at Joints under Tidal Environment”, ACI Materials Journal, Vol. 100, No. 4, pp. 265-273

Mullard, A. and Stewart, M. (2011), “Corrosion-Induced Cover Cracking: New Test Data and Predictive Models”, ACI Structural J., Vol. 108, No. 1, pp. 71 – 79

Munoz, A., Andrade, C. and Torres, A. (2007), “Corrosion Products Pressure Needed to Crack the Concrete Cover”, In: Advances in Construction Materials, pp. 359-370. Springer Link, ISBN: 978-3-540-72448-3 (On-line)

Neville, A. (2002), "Autogenous Healing - a Concrete Miracle?", Concrete International, Vol. 24, No. 11, pp. 76-82

Niwa, A. and Clough, R. W. (1980), “Shaking Tables Research on Concrete Dam Models”, EERC Report No. 85-05, University of California, Berkeley, California. 113 pp (Available online: http://nisee.berkeley.edu/documents/EERC/EERC-80-05.pdf)

Niwa, J., Maekawa, K. and Okamura, H. (1981), “Non-Linear Finite Element Analysis of Deep Beam, IABSE Colloquium, Delft, Vol. 34, pp. 625 – 638

Nossoni, G. (2010), “Holistic Electrochemical and Mechanical Modeling of Corrosion-Induced Cracking in Concrete Structures” Ph.D., Civil Engineering, Michigan State University, East Lansing, Michigan, USA

Nossoni, G. and Harichandran, R. (2012), “Current Efficiency in Accelerated Corrosion Testing of Concrete” Corrosion, Vol. 68, No. 9, pp. 801-809

Otieno, M., Beushausen, H. and Alexander, M. (2011), “Prediction of Corrosion Rate in Reinforced Concrete Structures – A critical Review and Preliminary Results”, Materials and Corrosion, Vol. 62, No.9, pp. 1-14

Pantazopoulou, S. and Papoulia, K. (2001), “Modeling Cover Cracking Due to Reinforcement Corrosion in RC Structures”, J. of Engineering Mechanics, ASCE, Vol. 127, No. 4, pp. 342-351

Pearlstein, F. and Weightman, R. F. (1967), “Derusting Corrosion Specimens: Stannous Chloride as an Acid Derusting Inhibitor”, Corrosion, Vol. 6, No. 3, pp.45-46

Poworoznek, P. (2008), “Elastic-Plastic Behavior of a Cylinder Subject to Mechanical and Thermal Loads”, Master Thesis, Department of Mechanical Engineering, Rensselaer Polytechnic Institute, Hartford, Connecticut, USA

Pruckner, F. (2001), “Corrosion and Protection of Reinforcement in Concrete Measurements and Interpretations”, Ph.D. thesis, Faculty of Natural Sciences and mathematics, University of Vienna, Vienna

Ramm, W. and Biscoping, M. (1998), “Autogenous Healing and Reinforcement Corrosion of Water-Penetrated Separation Cracks in Reinforced Concrete", Nuclear Engineering and Design, Vol. 179, No. 2, pp.191-200

Raupach, M. (1996), “Chloride-induced Macrocell Corrosion of Steel in Concrete-Theoretical background and Practical Consequences”, Construction and Building Materials, Vol. 10, No. 5, pp. 329-338

Redaelli, E., Bertolini, L., Peelen, W. and Polder, R. (2006), “FEM-Models for the Propagation Period of Chloride Induced Reinforcement Corrosion”, Materials and Corrosion, Vol. 57, No. 8, pp.628-635

Sadd, M. (2009), “Elasticity: Theory, Applications, and Numerics”, 2nd Edition, Burlington, Academic Press.

Sagüés, A.A. and Kranc, S.C. (1992), “On the determination of Polarization Diagrams of Reinforcing Steel in Concrete”, Corrosion, Vol. 48, No.8, pp. 624-633

Sagüés, A. A. (1993), “Corrosion Measurement Techniques for Steel in Concrete”, Corrosion / 93, Paper No. 353, Houston, TX, USA

Sagüés, A. A., Moreno, E., Morris, W. and Andrade, C. (1997), “Carbonation in Concrete and Effect on Steel Corrosion” Final Report to Florida Dept. of Transportation, WPI 0510685, (Accessed online: March 14, 2012) (http://www.dot.state.fl.us/research-center)

Sagüés, A. A., Peña, J., Cotrim, C., Pech-Canul, M. and Urdaneta, I. (2001), "Corrosion Resistance and Service Life of Drainage Culverts", Final Report to Florida Dept. of Transportation, Report no. WPI 0510756, Contract no. B-9898

Sagüés, A. A. and Kranc, S. (2006), "Corrosion Forecasting for 75-Year Durability Design of reinforced Concrete" Final Report to Florida Dept. of Transportation, WPI 0510805, Tallahassee, Fl, USA

Sagüés, A. A. and Fernandez, J. (2013), "Modeling Nuclear Containment Steel Liner Corrosion", Corrosion / 2013, Paper No.2668, Houston, TX, USA

Schiessl, P. and Raupach, M. (1997) "Laboratory Studies and Calculations on the Influence of Crack Width on Chloride-Induced Corrosion of Steel in Concrete", ACI Materials Journal, Vol. 94, No. 1, pp. 56-61

Singh, D. D. N. and Kumar, A. (2003), "A Fresh Look at ASTM G1-90 Solution Recommended for Cleaning of Corrosion Products Formed on Iron and Steels", Corrosion, Vol. 59, No. 11, pp. 1029-1036

Song, H. W. and Saraswathy, V. (2007), "Corrosion Monitoring of Reinforced Concrete Structures – A Review", International Journal of Electrochemical Science, Vol. 2, No. 1, pp.1-28

Subramaniam, K. V. and Bi, M. (2010), "Investigation of Steel Corrosion in Cracked Concrete: Evaluation of Macrocell and Microcell Rates using Tafel Polarization Response", Corrosion Science, Vol. 52, No. 8, pp. 2725-2735

Tang, F., Chen, G., Brow, R., Volz, J. and Koenigstein, M. (2012), "Corrosion Resistance and Mechanism of Steel Rebar Coated with Three Types of Enamel" Corrosion Science, Vol. 59, No.12, pp. 157-168

Torres-Acosta, A. (1999), "Cracking Induced by Localized Corrosion of Reinforcement in Chloride-Contaminated Concrete," Ph.D. Dissertation, Department of Civil & Environmental Engineering, University of South Florida, Tampa, FL, USA

Torres-Acosta, A. and Sagüés, A. A. (2004), "Concrete Cracking by Localized Steel Corrosion - Geometric Effects" ACI Materials Journal, Vol. 101, No. 6, pp. 501–507, American Concrete Institute, Farmington Hills, MI

Torres-Acosta, A. (2010), "Accelerated Vs. Natural Corrosion Experimental results for Remaining life Stage Forecasting", Concrete Under Severe Conditions – Environment and Loading, Castro-Borges et al., Vol. 1, Taylor and Francis Group, London, ISBN 978-0-415-59316-8

Tuutti, K. (1982), "Corrosion of Steel in Concrete", Swedish Cement and Concrete Research Institute, Stockholm, Sweden, 469 pp.

Val, D. and Stewart, M. (2009), “Reliability Assessment of Aging Reinforced Concrete Structures - Current Situation and Future Challenges”, Structural Engineering international, Vol.19, No.2, pp. 211-219

Vu, K. and Stewart, M. (2000): “Structural reliability of concrete bridges including improved chloride-induced corrosion models”, Structural Safety, Vol. 22, No. 4 pp. 313-333

Vu, K., Stewart, M. and Mullard, J. (2005), “Corrosion-Induced Cracking: Experimental Data and Predictive Models”, ACI Structural Journal, Vol. 102, No. 5 pp. 719 – 726

Williamson, G. (2007), “Service Life Modeling of Virginia Bridge Decks,” Ph.D. Dissertation, Department of Civil and Environmental Engineering, Virginia Polytechnic Institute and State University, Blacksburg, VA, USA

Wong, H. S., Zhao, Y. X., Karimi, A. R., Buenfeld, N. R. and Jin, W. L. (2010), “On the Penetration of Corrosion Products From Reinforcing Steel into Concrete Due to Chloride-Induced Corrosion”, Corrosion Science, Vol. 52, No. 7 , pp. 2469-2480

Young, G. (1967), “Humidity Control in the Laboratory Using Salt Solutions – A review”, J. of Applied Chemistry., Vol. 17, No.9, pp. 241 – 245

Zhao, Y., Karimi, A., Wong, H., Hu, B., Buenfeld, N. and Jin, W. (2011), “Comparison of Uniform and Non-uniform Corrosion Induced damage in reinforced Concrete Based on Gaussian description of the Corrosion Layer”, Corrosion Science, Vol. 53, No. 9, pp. 2803 – 2814

Zhou, K. Martin-Perez, B. and Lounis, Z. (2005), “Finite Element Analysis of Corrosion-Induced Cracking, Spalling and Delamination of RC Bridge Decks”, 1st Canadian Conference on Effective Design of Structures, McMaster University, July 10 -13th , Hamilton, Ontario, Canada

APPENDICES

Appendix A Experimental and Evaluation Procedures

A.1 Approximation Procedure to Calculate the Value of Rp for Impedance Spectra Obtained When Running EIS to a Lowest Frequency of 10 mHz.

For EIS spectra that have a lowest frequency end of 10 mHz indicated in chapter 3, an approximation procedure was applied to estimate the value of polarization resistance Rp for a given specimen. A provisional value for polarization resistance Rpp was obtained from figure A.1 and multiplied by a factor of proportionality P_F to obtain the corrected values of Rp as given by:

$$Rp = Rpp\ P_F \tag{A.1}$$

where Rpp is estimated by:

$$R_{PP} = \sqrt{(Z' - Rs)^2 + Z''^2} \tag{A.2}$$

where Z', Z'', Rs and Rpp are illustrated in figure A.1 The factor of proportionality P_F was obtained from another set of impedance spectrum for the specimen being evaluated but with the test performed to a lowest frequency end of 1 mHz. For that wider spectrum, the value of Rpp corresponding to 10 mHz may easily be found (measured). The value of Rp can be obtained using the equivalent circuit following the procedure in chapter 3. The proportionality factor P_F may then be determined using also equation (A.1). In order to ensure stability and consistency of the obtained proportionality factor P_F, the procedure was repeated for various

EIS spectra for a number of specimens. It was concluded that the value of P_F remains reasonably unchanged with time for a given specimen under a given exposure environment [Busba RC pipe report].

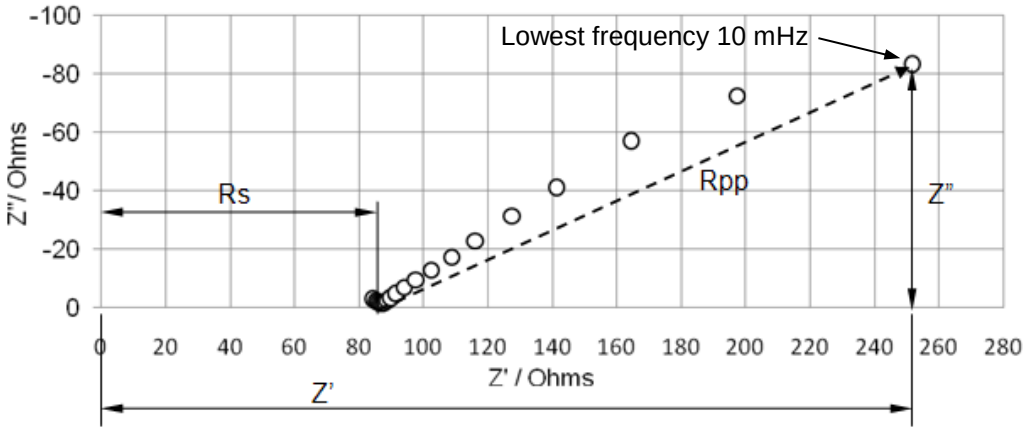

Figure A.1 Method for estimating the provisional polarization resistance value (Rpp) for EIS measurements corresponding to a lowest frequency end of 10 mHz. Circular symbols: EIS data whereas the broken line represents an estimation of the Rpp value.

A.2 Effect of Counter Electrode Configuration on Current Distribution

The case of uniformly corroding carbon steel bar was numerically simulated to examine the influence of CE geometry on current distribution pattern. The specimen dimensions were similar to those for the cases of uniformly corroding smooth bars (U1 to U7) in table 3.4. The concrete resistivity was assumed to be 100 Ohm.m and a reference potential of the steel bar was assumed to 0.2 V. The considered case was treated as an axisymmetric problem. Therefore the modeled part was only the half rectangle shown in figure A.2. For conservation

of energy, the electrical potential within the modeled sub domain has to satisfy Laplace's equation (equation 5.25). Figure A.3 (a) shows the current distribution pattern for the CE geometry selected for the experimental testing. Figure A.3 (b) shows the current distribution pattern for a CE geometry covering the entire concrete surface.

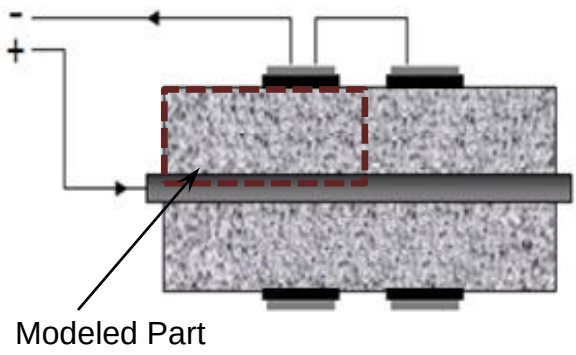

Figure A.2 A schematic diagram of the specimen being modeled and the CE geometry used for the experimental program.

The applied voltage required to achieve an average current density over the rebar surface was ~ 2.2 V and ~ 1.4 V in cases (a) and (b), respectively in figure A.3.

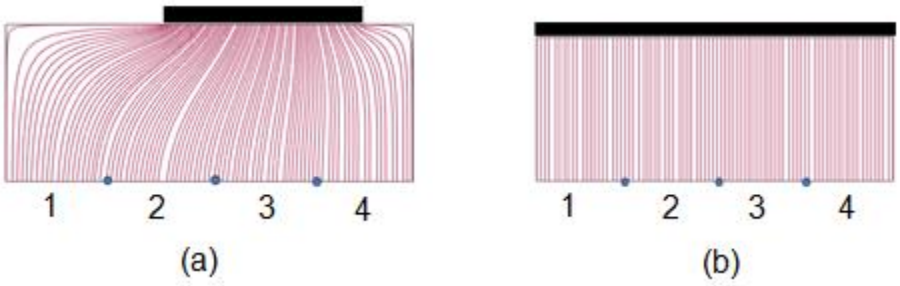

Figure A.3 Current distribution patterns for the cases with CE geometries (a) partially and (b) entirely, covering the cylinder concrete surface.

In the cases (a) and (b) of figure A.3, the rebar length was divided into short segments. The current density was calculated over each short segment to examine current distribution in each case. The individual current densities over the segments 1, 2, 3 and 4 were found to be nearly the same in both cases with values of about 100 μA/cm^2.

Appendix B Output of FE Modeling of Mechanical and Electrochemical Behaviors of Rebar Corrosion as a Function of Degree of Localization

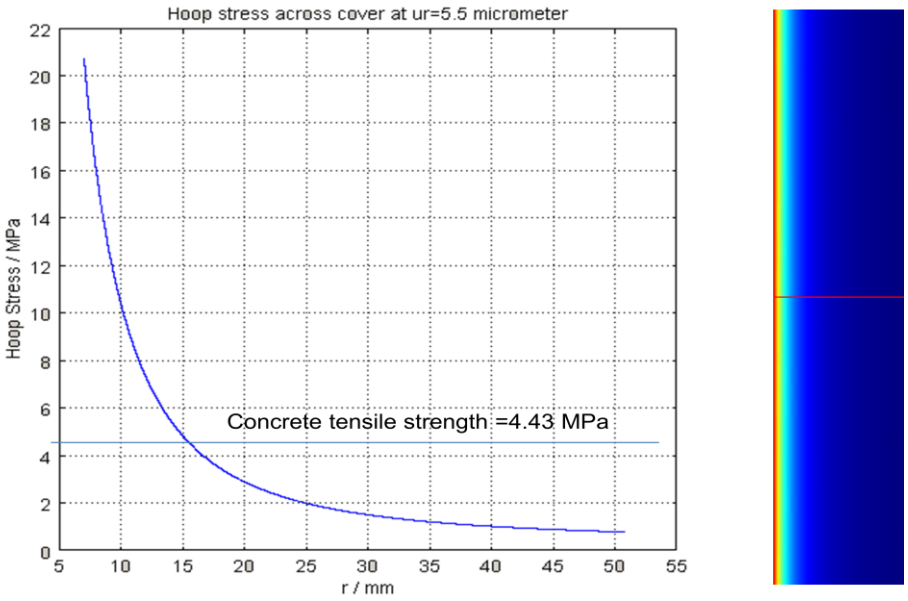

Figure B.1 Hoop stress across concrete cover for the base case of uniform corrosion in table 5.2 at radial displacement (u_r) of 5.5 μm. (Cracking evaluated according to empirical failure criterion)

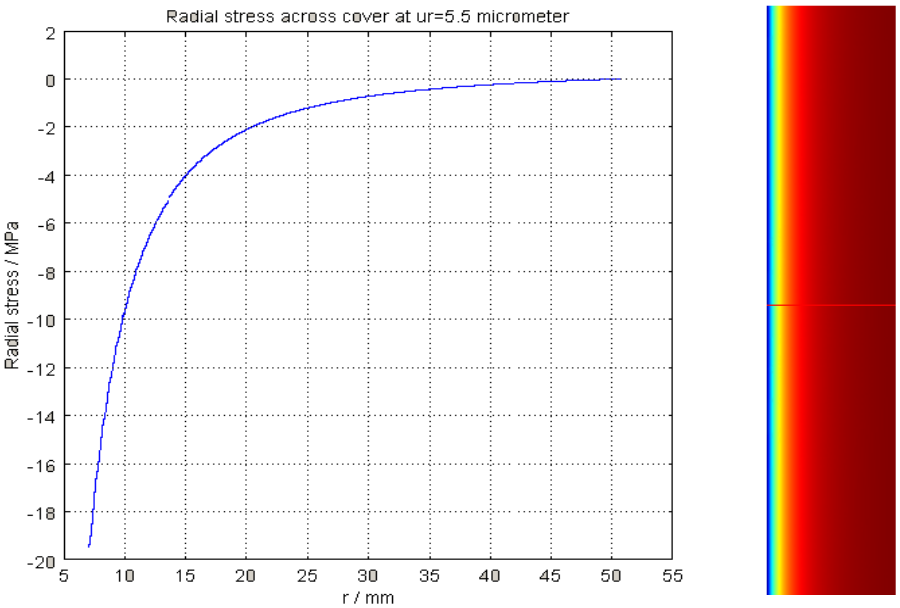

Figure B.2 Radial stress across concrete cover for the base case of uniform corrosion in table 5.2 at radial displacement (u_r) of 5.5 μm. (Cracking evaluated according to empirical failure criterion)

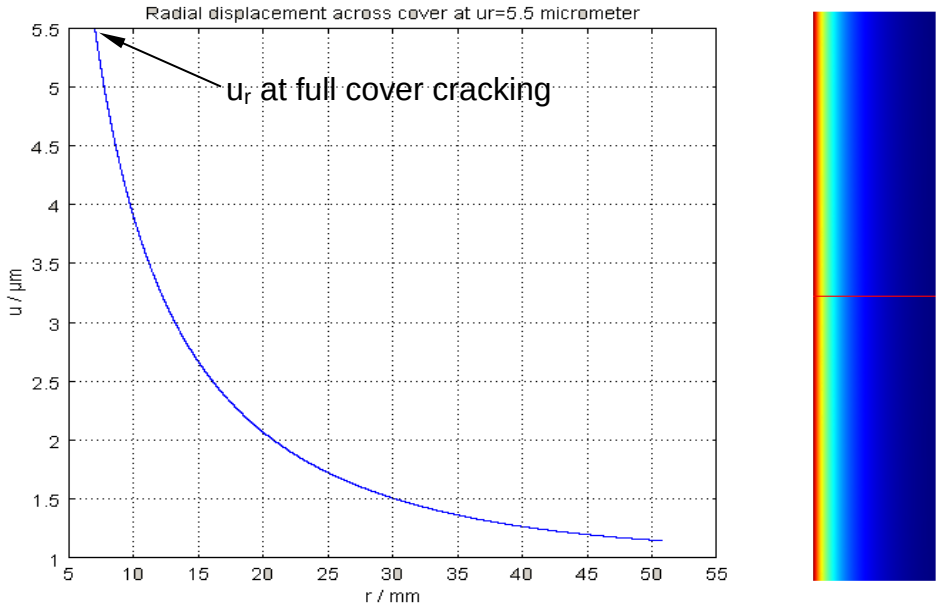

Figure B.3 Radial displacement of concrete cover for the base case of uniform corrosion in table 5.2 at onset of cracking. (Cracking evaluated according to empirical failure criterion)

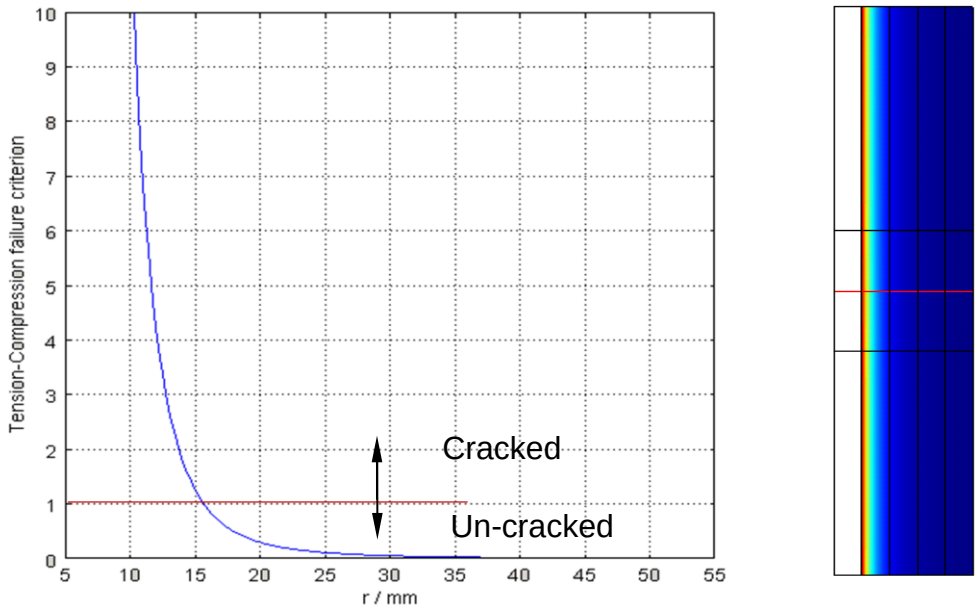

Figure B.4 Tension-Compression failure criterion across concrete cover indicating partition 1 cracking for the base case of uniform corrosion in table 5.2.

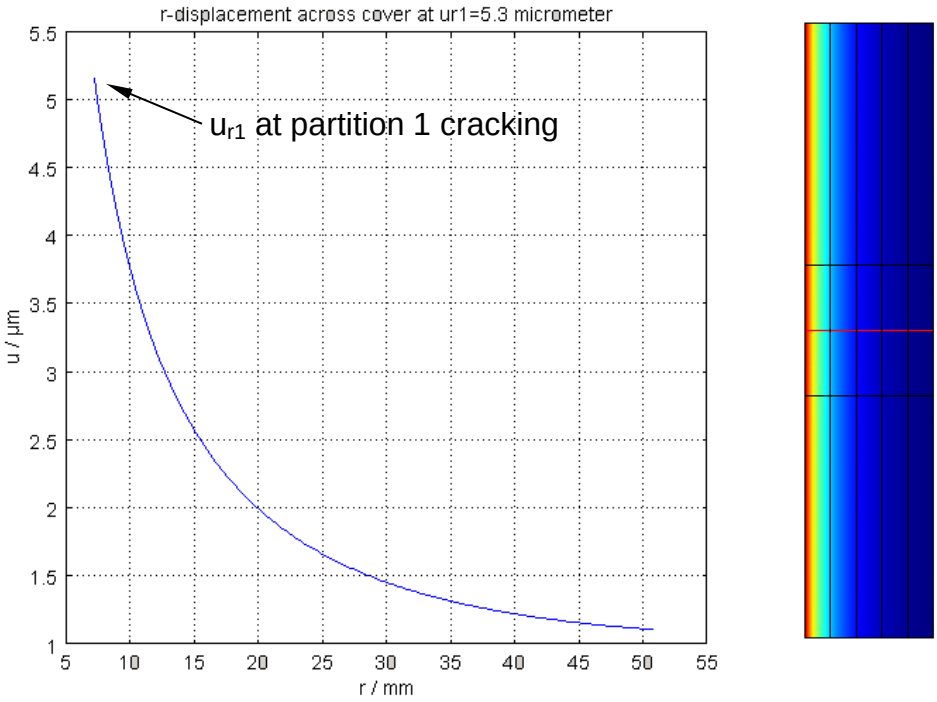

Figure B.5 Radial displacement (u_{r1}) of 5.3 µm corresponding to crack initiation (partition 1 cracking) for the base case of uniform corrosion in table 5.2. (Onset of cracking evaluated according to Tension-Compression criterion)

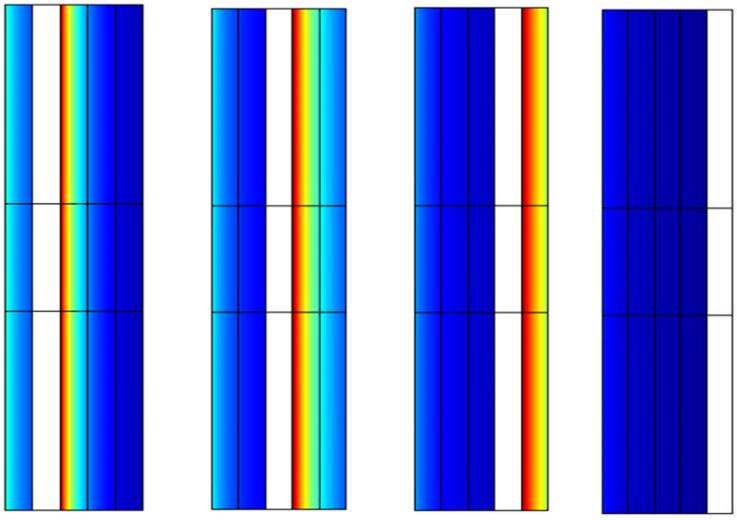

Figure B.6 Crack propagation across concrete cover manifested by the progression of Tension-Compression criterion front through the rest of partitions along the corroding length for the case in figure B.4. Criterion =1(red), <1(blue).

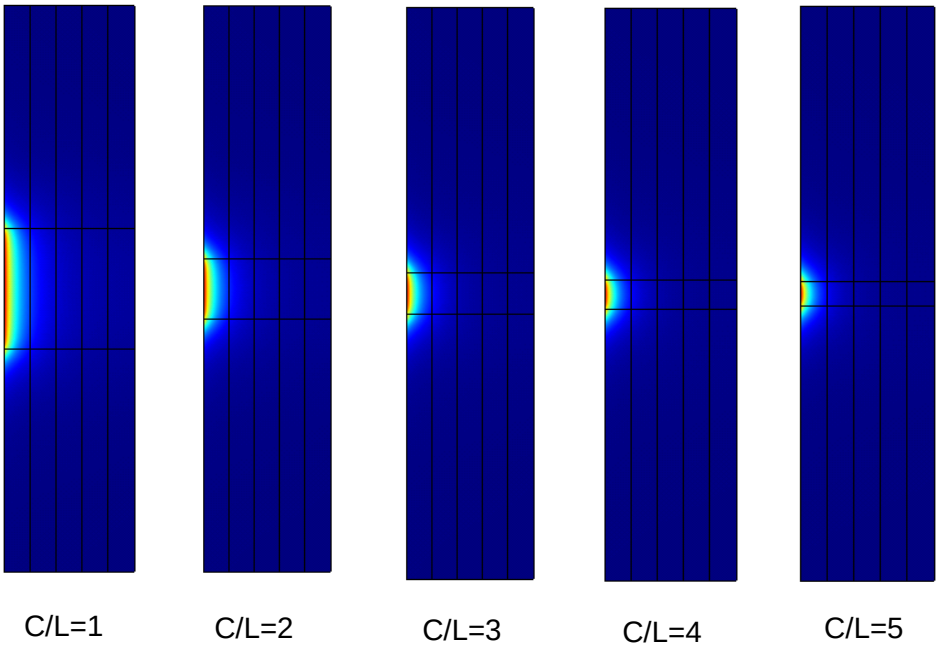

Figure B.7 Hoop stress distribution trends across concrete cover for crack initiation (cracking of partition 1) for the cases of localized corrosion in table 5.3

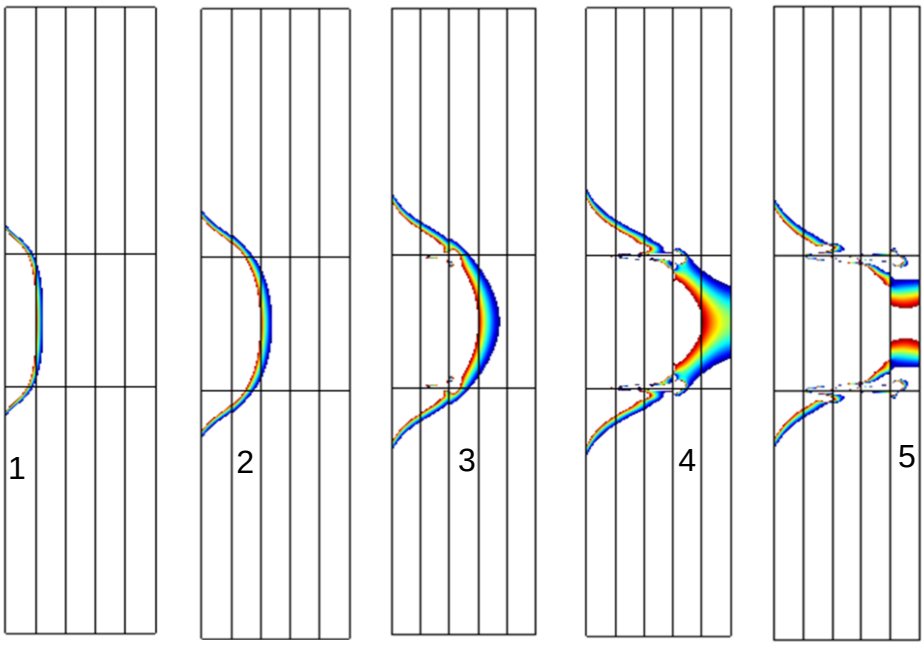

Figure B.8 Progression trend of the Tension-Compression failure criterion front across concrete cover through the five partitions (crack initiation and propagation) for the case of C/L=1 in figure B.7. Criterion =1(red), 0.5 (blue).

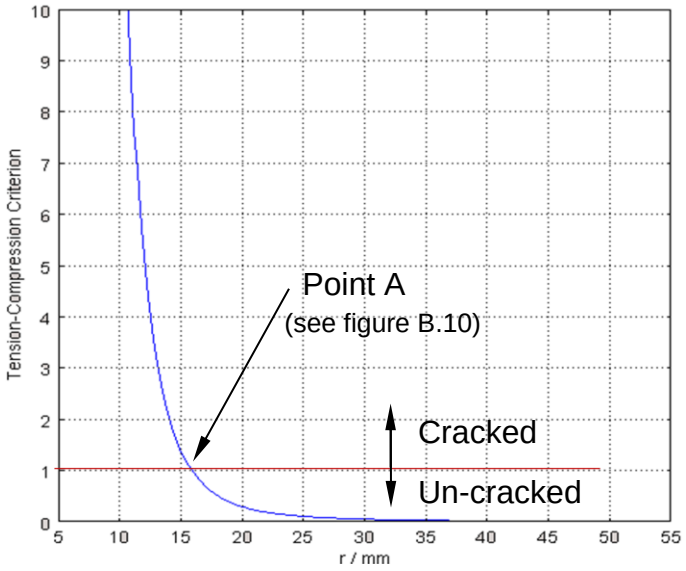

Figure B.9 Tension-Compression failure criterion across concrete cover at the midpoint along the corroding length indicating partition 1 cracking for the case of C/L=1.

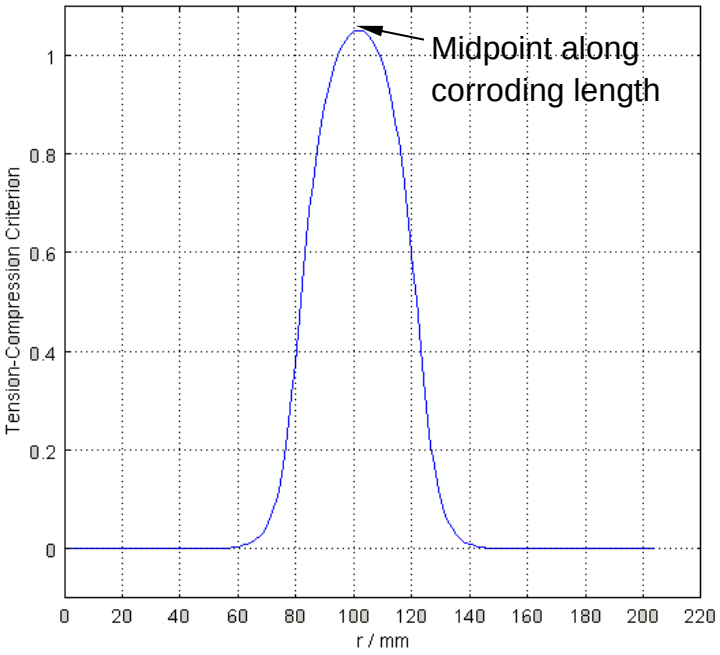

Figure B.10 Tension-Compression failure criterion along cylinder length at the outer radius of partition 1 indicating its cracking (for the case of C/L=1). For point A in figure B.9.

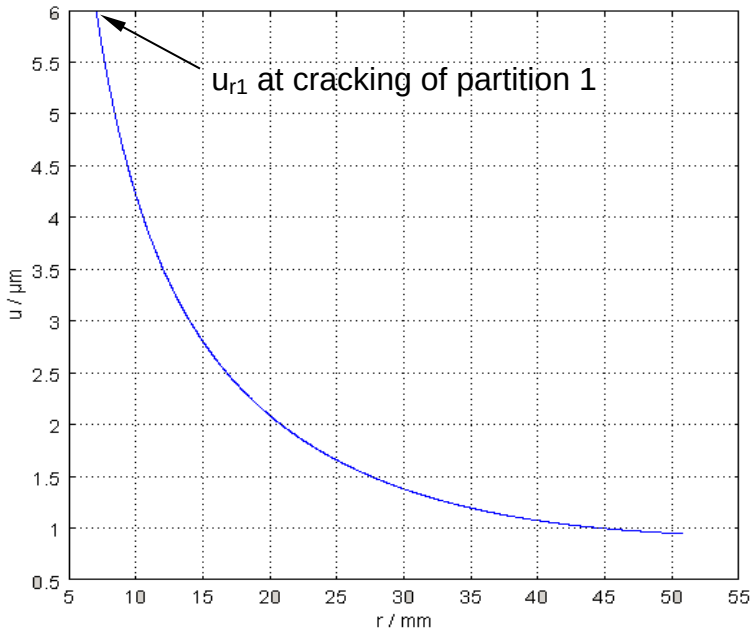

Figure B.11 Radial displacement across concrete cover at midpoint along corroding length at cracking of partition 1 for the case of C/L=1.

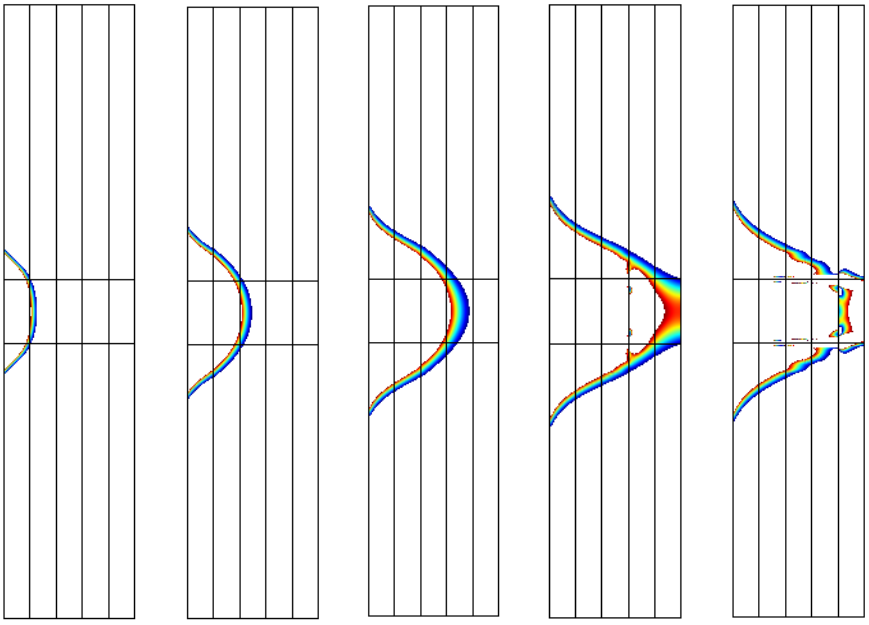

Figure B.12 Progression trend of the Tension-Compression failure criterion front across concrete cover through the five partitions (crack initiation and propagation) for the case of C/L=2 in figure B.7. Criterion =1(red), 0.5 (blue).

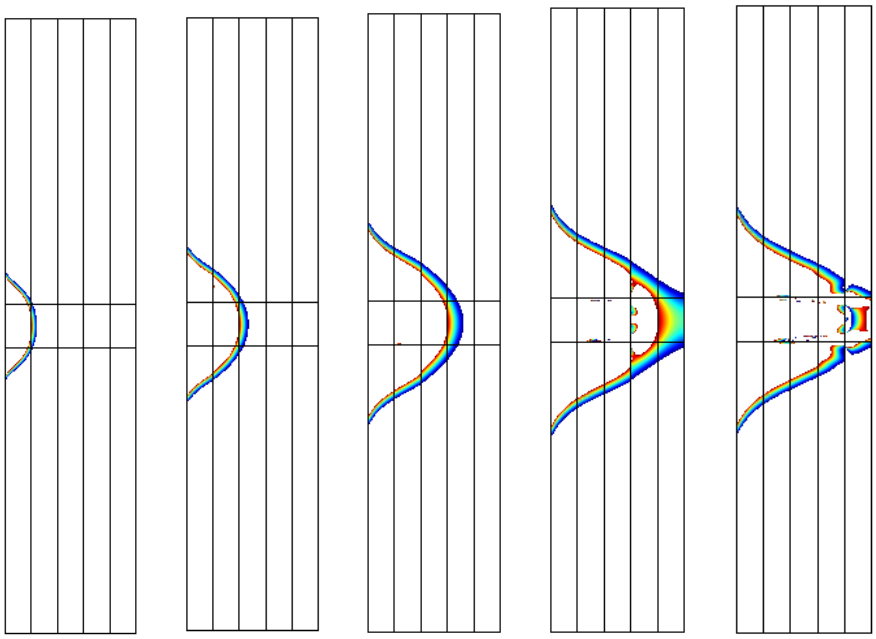

Figure B.13 Progression trend of the Tension-Compression failure criterion front across concrete cover through the five partitions (crack initiation and propagation) for the case of C/L=3 in figure B.7. Criterion =1(red), 0.5 (blue).

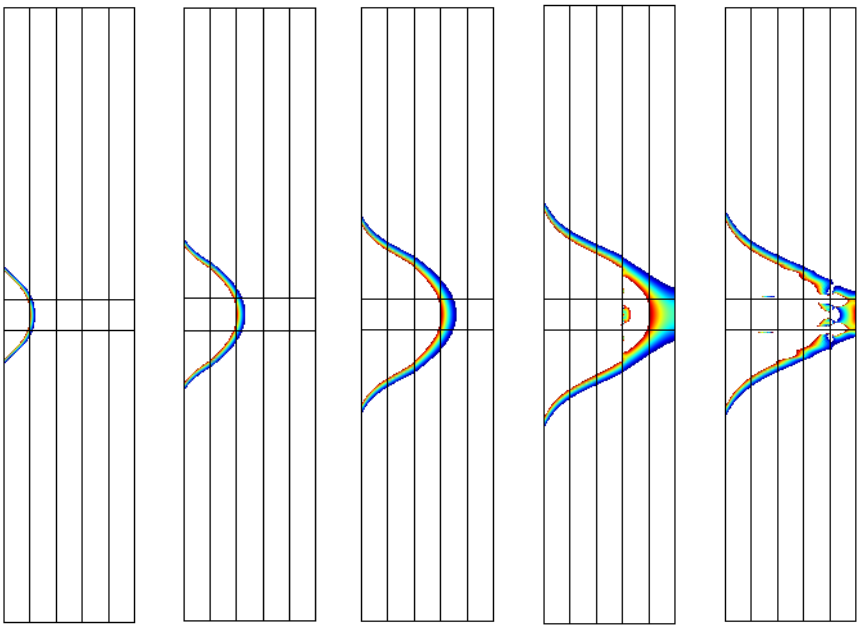

Figure B.14 Progression trend of the Tension-Compression failure criterion front across concrete cover through the five partitions (crack initiation and propagation) for the case of C/L=4 in figure B.7. Criterion =1(red), 0.5 (blue).

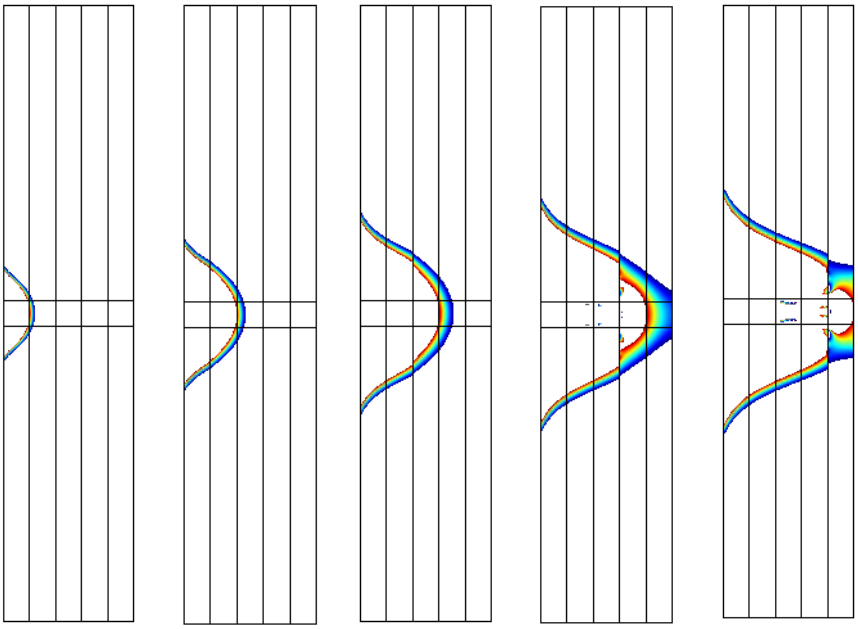

Figure B.15 Progression trend of the Tension-Compression failure criterion front across concrete cover through the five partitions (crack initiation and propagation) for the case of C/L=5 in figure B.7. Criterion =1(red), 0.5 (blue).

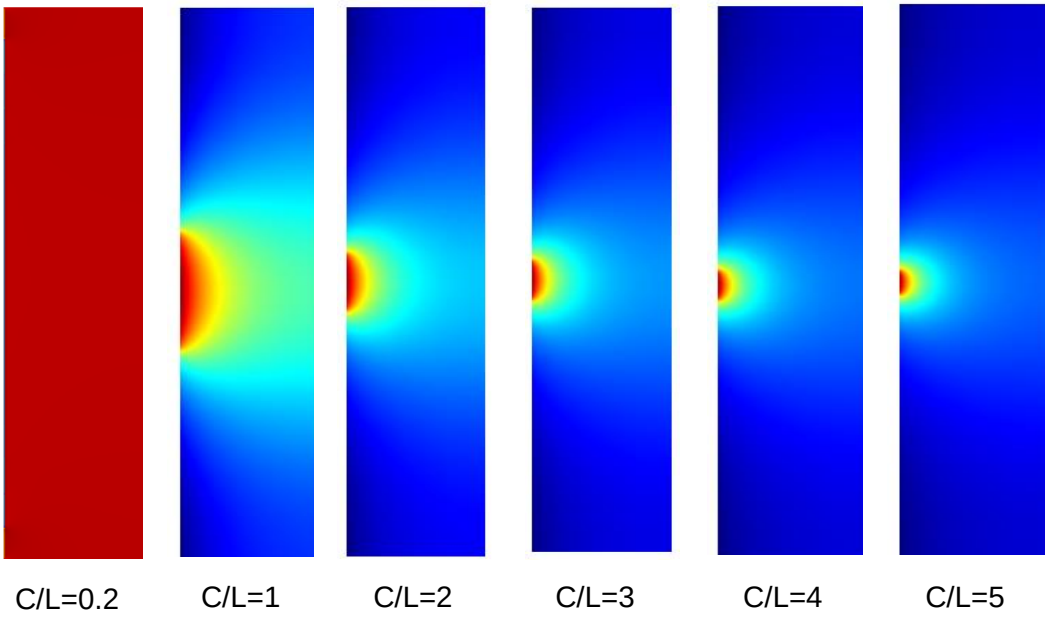

Figure B.16 Potential distribution trends across concrete cover for the localized corrosion cases considering the 100% macrocell current scenario and for the uniform corrosion case. (Potential levels were reported in chapter 5)

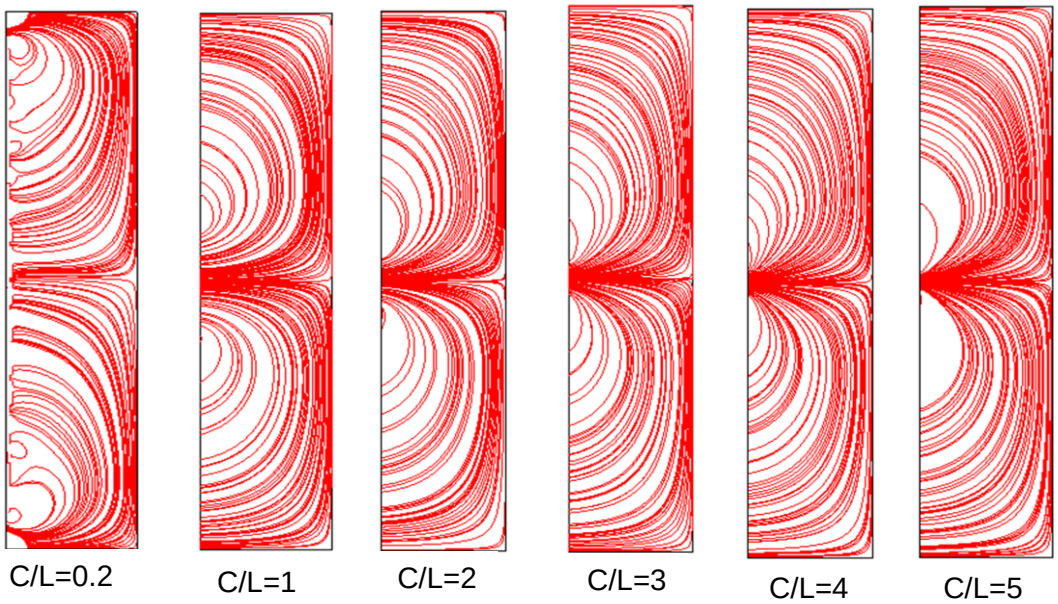

Figure B.17 Streamline trends of total current densities across concrete cover for the localized corrosion cases considering the 100% macrocell current scenario and for the uniform corrosion case.

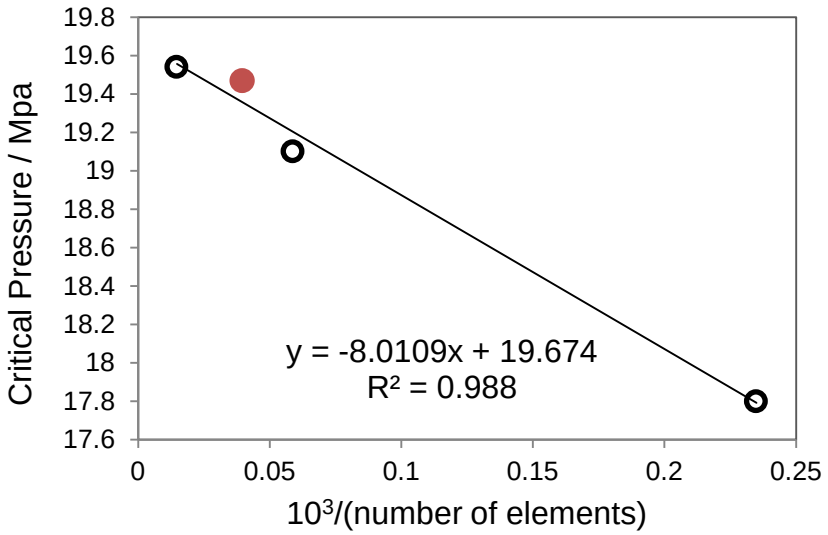

Figure B.18 Model sensitivity when considering only half of the rectangular part in figure 5.2. The model was run for a case of a uniformly corroding bar and the results evaluated using the empirical cracking criterion. The red circle represents the mesh size adopted for the model with no more than about 1% deviation from the target value of 19.674 Mpa (corresponding to infinite number of elements).

Appendix C Copyright Permissions

C.1 Permissions for Figure 4.28

RightsLink

Copyright Clearance Center

Thank You For Your Order!

Dear Mr. Ezeddin Busba,

Thank you for placing your order through Copyright Clearance Center's RightsLink service. Elsevier has partnered with RightsLink to license its content. This notice is a confirmation that your order was successful.

Your order details and publisher terms and conditions are available by clicking the link below: http://s100.copyright.com/CustomerAdmin/PLF.jsp?ref=681b5e8c-a88f-4a6e-a687-a648355ad95d

Order Details
Licensee: Ezeddin R Busba
License Date: Aug 23, 2013
License Number: 3214831154750
Publication: Corrosion Science
Title: Microscopic investigation of mill scale and its proposed effect on the variability of chloride-induced depassivation of carbon steel rebar
Type Of Use: reuse in a thesis/dissertation
Total: 0.00 USD

RightsLink

Copyright Clearance Center

Thank You For Your Order!

Dear Mr. Ezeddin Busba,

Thank you for placing your order through Copyright Clearance Center's RightsLink service. Elsevier has partnered with RightsLink to license its content. This notice is a confirmation that your order was successful.

Your order details and publisher terms and conditions are available by clicking the link below: http://s100.copyright.com/CustomerAdmin/PLF.jsp?ref=1426ab30-da16-4b50-8843-f0b48d689d51

Order Details
Licensee: Ezeddin R Busba
License Date: Aug 29, 2013
License Number: 3218271445913
Publication: Cement and Concrete Research
Title: Chloride-induced corrosion products of steel in cracked-concrete subjected to different loading conditions
Type Of Use: reuse in a thesis/dissertation
Total: 0.00 USD

Appendix C (Continued)

C.2 Permission for Referring to Information in www.saveourbridges.com

From: ebusba@mail.usf.edu [mailto:ebusba@mail.usf.edu]
Sent: Thursday, August 22, 2013 3:42 PM
To: lindsay@dehartandcompany.com; ptoulatos@lepatner.com
Subject: Save Our Bridges Contact Form

From http://saveourbridges.com
IP 68.200.159.75

Name: Ezeddin Busba
Address: [redacted]
City: [redacted]
State: [redacted]
Zipcode: [redacted]
Phone Number: [redacted]
Message: Dear Mr Le Patner I am a PhD student in the University of South Florida and currently writing my dissertation on a topic related to corrosion-induced concrete cracking. I intend to make a general reference in my introduction to your website. Therefore I would like to seek your permission to do so. Thanks and Regard, Ezeddin Busba

RE: Save Our Bridges Contact Form Inbox x

Lindsay Miller <lindsay@dehartandcompany.com> 2:04 PM (2 hours ago)
to me

Hi Ezeddin,

We work with Barry LePatner on the promotion of his books and websites and received your email below.

He asked that we respond to you. Barry said that yes, you have his permission to mention Save Our Bridges in your dissertation. He also asked if it would be possible for him to receive a copy of your dissertation once it is complete. Will you please let me know?

Thank you,
Lindsay Miller
DeHart & Company
The Piedmont Center
1375 Lenoir Rhyne Blvd. SE, Suite 109
Hickory, NC 28602
Direct Phone: 828-325-4967
Direct Fax: 828-325-4968
E-mail: Lindsay@dehartandcompany.com
www.dehartandcompany.com

Appendix C (Continued)

C.3 Permissions for Contents in Chapters 3 and 4 from Previous Publications

NACE INTERNATIONAL

Permission to Publish
NACE International
Copyrighted Paper/Article

NACE International
1440 South Creek Drive
Houston, TX 77084
Tel: 281-228-6219
Fax: 281-228-6319

Date: 08.27.2013

Name: Ezeddin Busba Title: Graduate Student

Company ("Publisher"): University of South Florida

Address: 4202 E Fowler Ave, Tampa, Florida 33620

Tel: [redacted] Fax: _____

Email: ebusba@mail.usf.edu

Publication Media: Check the applicable Box:

☐ Magazine/Journal ("Periodical"): Corrosion Issue: Vol. 69 No.4

☐ ~~Web Site URL ("Web Site")~~: Effect of localized corrosion on Chloride-induced corercracking (dissertation)

Circle the source: *Materials Performance* (CORROSION) Conference Paper Standards

Paper/Article Title: Localized Corrosion of Embedded steel in Cracked Reinforced Concrete pipes ("Work") Conference Paper No./Year: _____

Authors: Ezeddin Busba and Alberto Sagues

NACE International ("NACE") hereby grants to "Publisher" the right to publish the Work utilizing the Publication Media elected above. To the extent the Publication Media is a Periodical, the publication right is limited to publication in the specific issue identified above of the Periodical identified above and this right shall automatically terminate upon the date of issue of the particular issue of the Periodical, whether or not such Work is actually published. To the extent the Publication Media is a Web Site, the publication right is limited to publication at the specific Web Site identified above. Any right granted herein is a limited, non-transferable, non-exclusive right. No other rights in the Work are granted herein. The Publisher agrees to hold NACE harmless and indemnify NACE against any and all legal action and expenses arising out of the Publisher's use and editing of NACE material.

Notwithstanding the foregoing, Publisher may edit or otherwise modify the Work as reasonably necessary to accommodate the style and size requirements of the specific publication so long as the published Work that will appear in the Publication remains substantially similar to the original Work. Any such permitted edit or modification shall maintain the integrity of the overall original Work.

Publisher shall obtain a copy of the original Work directly from NACE International and shall not utilize copies of the Work from other sources, including the author(s). Publisher shall include on the published version of the Work the names of all authors listed on the original Work.

The Publisher shall include the following applicable Copyright notation with any publication of the Work:*

A. Conference Paper
Reproduced with permission from NACE International, Houston, TX. All rights reserved. Paper NUMBER presented at CORROSION/YEAR, City, State. © NACE International YEAR.

B. Magazine/Journal Article
Reproduced with permission from NACE International, Houston, TX. All rights reserved. Published in the MONTH, YEAR issue of JOURNAL. © NACE International YEAR.

C. Standards
STANDARDS/TECHNICAL COMMITTEE REPORT NAME. © NACE International YEAR. All rights reserved by NACE. Reprinted with permission. NACE standards are revised periodically. Users are cautioned to obtain the latest edition; information in an outdated version of the standard may not be accurate.

* Modifications to Notations: Other reference wording can be used, but must be approved by NACE in writing *in advance*.

As between NACE and Publisher, Publisher acknowledges that NACE owns all rights in the Works. Publisher shall not be entitled to any compensation for its efforts in promoting the Work.

THE WORK IS PROVIDED "AS IS." ALL EXPRESS OR IMPLIED COVENANTS, CONDITIONS, REPRESENTATIONS OR WARRANTIES, INCLUDING ANY IMPLIED WARRANTY OF MERCHANTABILITY OR FITNESS FOR A PARTICULAR

PermissiontoPublishNACECopy.doc

Appendix C (Continued)

PURPOSE OR CONDITIONS OF ACCURACY, COMPLETENESS OR QUALITY AND THOSE ARISING BY STATUTE OR OTHERWISE IN LAW, ARE HEREBY DISCLAIMED.

IN NO EVENT WILL NACE BE LIABLE FOR ANY DIRECT, INDIRECT, PUNITIVE, SPECIAL, INCIDENTAL OR CONSEQUENTIAL DAMAGES IN CONNECTION WITH OR RELATED TO THIS AGREEMENT (INCLUDING LOSS OF PROFITS, USE, DATA, OR OTHER ECONOMIC ADVANTAGE), HOWSOEVER ARISING.

This Agreement and the rights granted herein may be terminated immediately by NACE upon breach of this Agreement by Publisher. Unless earlier terminated, this Agreement and the rights granted herein will automatically terminate 6 months from the Date set forth above. If the Work has not been published within that time period, a new Agreement must be obtained.

Publisher may not, directly or indirectly, sell, assign, sublicense, lease, rent, distribute, or otherwise transfer this Agreement or any rights granted herein, without the prior written consent of NACE.

If any provision of this Agreement is found to be unenforceable, then this Agreement shall be deemed to be amended by modifying such provision to the extent necessary to make it legal and enforceable while preserving its intent. The remainder of this Agreement shall not be affected by such modification.

This Agreement does not create, and shall not be construed to create, any employer-employee, joint venture or partnership relationship between the parties. No officer, employee, agent, servant or independent contractor of either party shall at any time be deemed to be an employee, servant, agent or contractor of any other party for any purpose whatsoever.

This Agreement shall be governed by, and construed and enforced in accordance with, the laws of the State of Texas, without regard to the choice of law provisions of that State.

This Agreement shall only be effective if signed by authorized representatives of both parties. This Agreement constitutes the entire Agreement between the parties with respect to the subject matter of this Agreement. Any change, modification or waiver hereto must be in writing and signed by authorized representatives of both parties.

Other Terms & Conditions: _____

Publisher hereby requests permission to publish the paper/article described above and agrees to comply with all Terms and Conditions listed above.

Request submitted by:

Ezeddin Busbq

Printed Name

Graduate Student

[redacted]

08.21.2013

Date

Request approved by NACE:

Brenda Nitz

Printed Name

Books Coordinator

Title

Brenda Nitz

Signature

Aug 27, 2013

Date

Request agreed to by:

Ezeddin Busbq

Lead Author Printed Name

Graduate Student

Lead Author Title

[redacted]

08.21.2013

Date

PermissiontoPublishNACECopy.doc

Appendix C (Continued)

NACE INTERNATIONAL

Permission to Publish
NACE International
Copyrighted Paper/Article

NACE International
1440 South Creek Drive
Houston, TX 77084
Tel: 281-228-6219
Fax: 281-228-6319

Date: 08.27.2013

Name: Ezeddin Busba Title: Graduate Student

Company ("Publisher"): University of South Florida

Address: 4202 E. Fowler Ave., Tampa, Florida 33620

Tel: [redacted] Fax: _____

Email: ebusba@mail.usf.edu

Publication Media: Check the applicable Box:

☐ Magazine/Journal ("Periodical"): Corrosion 2013 Conference Issue: _____

☑ ~~Web Site URL ("Web Site")~~: Dissertation

Circle the source: *Materials Performance* *CORROSION* (Conference Paper) Standards

Paper/Article Title: Critical localized Corrosion penetration of Steel Reinforcement for concrete Cover Cracking ("Work") Conference Paper No./Year: 2747/2013

Authors: Ezeddin Busba and Alberto Sagues

NACE International ("NACE") hereby grants to "Publisher" the right to publish the Work utilizing the Publication Media elected above. To the extent the Publication Media is a Periodical, the publication right is limited to publication in the specific issue identified above of the Periodical identified above and this right shall automatically terminate upon the date of issue of the particular issue of the Periodical, whether or not such Work is actually published. To the extent the Publication Media is a Web Site, the publication right is limited to publication at the specific Web Site identified above. Any right granted herein is a limited, non-transferable, non-exclusive right. No other rights in the Work are granted herein. The Publisher agrees to hold NACE harmless and indemnify NACE against any and all legal action and expenses arising out of the Publisher's use and editing of NACE material.

Notwithstanding the foregoing, Publisher may edit or otherwise modify the Work as reasonably necessary to accommodate the style and size requirements of the specific publication so long as the published Work that will appear in the Publication remains substantially similar to the original Work. Any such permitted edit or modification shall maintain the integrity of the overall original Work.

Publisher shall obtain a copy of the original Work directly from NACE International and shall not utilize copies of the Work from other sources, including the author(s). Publisher shall include on the published version of the Work the names of all authors listed on the original Work.

The Publisher shall include the following applicable Copyright notation with any publication of the Work:*

A. Conference Paper
Reproduced with permission from NACE International, Houston, TX. All rights reserved. Paper NUMBER presented at CORROSION/YEAR, City, State. © NACE International YEAR.

B. Magazine/Journal Article
Reproduced with permission from NACE International, Houston, TX. All rights reserved. Published in the MONTH, YEAR issue of JOURNAL. © NACE International YEAR.

C. Standards
STANDARDS/TECHNICAL COMMITTEE REPORT NAME. © NACE International YEAR. All rights reserved by NACE. Reprinted with permission. NACE standards are revised periodically. Users are cautioned to obtain the latest edition; information in an outdated version of the standard may not be accurate.

* Modifications to Notations: Other reference wording can be used, but must be approved by NACE in writing *in advance.*

As between NACE and Publisher, Publisher acknowledges that NACE owns all rights in the Works. Publisher shall not be entitled to any compensation for its efforts in promoting the Work.

THE WORK IS PROVIDED "AS IS." ALL EXPRESS OR IMPLIED COVENANTS, CONDITIONS, REPRESENTATIONS OR WARRANTIES, INCLUDING ANY IMPLIED WARRANTY OF MERCHANTABILITY OR FITNESS FOR A PARTICULAR

PermissiontoPublishNACECopy.doc

Appendix C (Continued)

PURPOSE OR CONDITIONS OF ACCURACY, COMPLETENESS OR QUALITY AND THOSE ARISING BY STATUTE OR OTHERWISE IN LAW, ARE HEREBY DISCLAIMED.

IN NO EVENT WILL NACE BE LIABLE FOR ANY DIRECT, INDIRECT, PUNITIVE, SPECIAL, INCIDENTAL OR CONSEQUENTIAL DAMAGES IN CONNECTION WITH OR RELATED TO THIS AGREEMENT (INCLUDING LOSS OF PROFITS, USE, DATA, OR OTHER ECONOMIC ADVANTAGE), HOWSOEVER ARISING.

This Agreement and the rights granted herein may be terminated immediately by NACE upon breach of this Agreement by Publisher. Unless earlier terminated, this Agreement and the rights granted herein will automatically terminate 6 months from the Date set forth above. If the Work has not been published within that time period, a new Agreement must be obtained.

Publisher may not, directly or indirectly, sell, assign, sublicense, lease, rent, distribute, or otherwise transfer this Agreement or any rights granted herein, without the prior written consent of NACE.

If any provision of this Agreement is found to be unenforceable, then this Agreement shall be deemed to be amended by modifying such provision to the extent necessary to make it legal and enforceable while preserving its intent. The remainder of this Agreement shall not be affected by such modification.

This Agreement does not create, and shall not be construed to create, any employer-employee, joint venture or partnership relationship between the parties. No officer, employee, agent, servant or independent contractor of either party shall at any time be deemed to be an employee, servant, agent or contractor of any other party for any purpose whatsoever.

This Agreement shall be governed by, and construed and enforced in accordance with, the laws of the State of Texas, without regard to the choice of law provisions of that State.

This Agreement shall only be effective if signed by authorized representatives of both parties. This Agreement constitutes the entire Agreement between the parties with respect to the subject matter of this Agreement. Any change, modification or waiver hereto must be in writing and signed by authorized representatives of both parties.

Other Terms & Conditions: _____

Publisher hereby requests permission to publish the paper/article described above and agrees to comply with all Terms and Conditions listed above.

Request submitted by:

Ezeddin Busba
Printed Name

Graduate Student
Title

[redacted]
Signature

08.27.2013
Date

Request approved by NACE:

Brenda Nitz
Printed Name

Books Coordinator
Title

Brenda Nitz
Signature

Aug. 27, 2013
Date

Request agreed to by:

Ezeddin Busba
Lead Author Printed Name

Graduate Student
Lead Author Title

[redacted]
Lead Author Signature

08.27.2013
Date

PermissiontoPublishNACECopy.doc